MECHANICAL PROPERTIES OF ZIRCONIUM AND ZIRCONIA SYSTEMS BY MOLECULAR DYNAMICS SIMULATION

By

ZIZHE LU

A DISSERTATION PRESENTED TO THE GRADUATE SCHOOL
OF THE UNIVERSITY OF FLORIDA IN PARTIAL FULFILLMENT
OF THE REQUIREMENTS FOR THE DEGREE OF
DOCTOR OF PHILOSOPHY

UNIVERSITY OF FLORIDA

2015

To my parents and all the loved ones

ACKNOWLEDGMENTS

I would like to express my sincerest appreciation to my advisor Dr. Simon Phillpot for his generous support of my PHD research, for his patience, kindness and immense knowledge. His guidance helped me to get through a lot of difficulties throughout my Ph.D study. Besides my advisor, I would like to thank Dr. Sinnott for her meaningful mentoring and collaborations. I'd also like to thank the rest of the committee members Drs. Michele Manuel, Yong Yang and Youping Chen for their insightful comments and encouragement.

My sincere thanks also goes to all the past and present group members, who shared their knowledge and led insightful discussions. Drs. Dong-Hyun Kim, Tao Liang, Tzu-Ray Shan, and Alex Chernatynskiy did an excellent mentoring work. The FLAMES group members are always there for each other. I am grateful to be in this group.

I would like to thank my girlfriend for her unconditional support and her love.

Last but not the least, I am forever thankful to my parents for their endless love and support. Their unconditional support allows me to pursue my life goal freely. This dissertation is dedicated to them for all their sacrifices.

TABLE OF CONTENTS

page

CHAPTER

LIST OF TABLES

LIST OF FIGURES

LIST OF ABBREVIATIONS

CNA	Common Neighbor Analysis
COMB	Charge-optimized Many-Body
DFT	Density Functional Theory
DXA	Dislocation Extraction Algorithm
EAM	Embeded Atom Method
EBSD	Electron Backscatter Diffraction
GGA	Generalized Gradient Approximation
GPF	General Planar Fault
LAMMPS	Large-scale Atomic/Molecular Massive Parallel Simulator
MA	Mendelev-Ackland
MD	Molecular Dynamics
MEAM	Modified Embedded Atom Method
SFE	Stacking Fault Energy
TEM	Transmission Electron Microscopy
USF	Unstable Stacking Fault

Abstract of Dissertation Presented to the Graduate School
of the University of Florida in Partial Fulfillment of the
Requirements for the Degree of Doctor of Philosophy

MECHANICAL PROPERTIES OF ZIRCONIUM AND ZIRCONIA SYSTEMS BY MOLECULAR DYNAMICS SIMULATION

By

Zizhe Lu

December 2015

Chair: Simon R. Phillpot
Major: Materials Science and Engineering

Zirconium alloys have been widely used as cladding material in nuclear reactors. Due to the extreme conditions inside the nuclear reactor, zirconium oxide and hydride can form at the cladding surface. Better understanding of the basic deformation behaviors of Zr and ZrO_2 systems will help to improve the design and ultimately performance of clad. Molecular dynamics (MD) simulation has been widely used in the study of defects and microstructures. The empirical potential that describes the atomic interactions plays an essential role in the MD simulations. An Embedded Atom Method (EAM) potential is used to describe the zirconium metallic system, while a third-generation Charged-Optimized Many-Body (COMB) potential is used to describe zirconium metallic system, zirconia ionic system and zirconia on top of zirconium heterogeneous system.

Molecular dynamics simulation is used to characterize the deformation behavior of polycrystalline Zr under tension. The deformation processes in $[11\bar{2}0]$ and $[0001]$ textured 2D structures and a fully 3D structure are studied. The predictions of the two different potentials are compared. The experimentally observed prismatic dislocations, pyramidal dislocations and twinning behaviors are reproduced in the simulations of

$[11\bar{2}0]$ and $[0001]$ 2D textured structures and in the fully 3D structure simulations. The relationship between the generalized stacking fault energy and the mechanical properties is discussed. In particular we find that the different shapes of the generalized stacking-fault energy curves for the two different interatomic descriptions of Zr have a significant effect on the deformation mechanisms.

Nanoindentation is now an important and widely-used method used to probe the mechanical properties of materials at the nanoscale. Molecular dynamics simulations of nanoindentation are used to study the deformation behaviors of single crystal Zr for four different surface orientations. The load-displacement curve, hardness and deformation behaviors of the various surface orientations Zr are compared and the elastic and plastic deformation behaviors are analyzed. As ZrO_2 often coats the clad, nanoindentation MD simulations are also performed on the ZrO_2 and ZrO_2/Zr systems and the load-displacement curve, hardness and deformation processes are analyzed. The deformation behaviors of Zr, ZrO_2 and ZrO_2/Zr systems are compared to understand how the oxide layer influences the mechanical properties of the cladding.

CHAPTER 1
INTRODUCTION

Background and Motivation

Zircaloy-2 and Zircaloy-4 are extensively used as cladding materials because Zr has a relatively low thermal neutron absorption cross section, a high melting point (2125 K), good mechanical strength at elevated temperatures, and good corrosion resistance [1, 2]. The weight percent of the other major components of Zircaloy-2 is Sn(1.2-1.7), Fe(0.07-0.20), Cr(0.05-0.15), and Ni(0.03-0.08). Zircaloy-4 was developed from Zircaloy-2 with the principal aim of reducing the tendency to pick up hydrogen [3, 4]. In Zircaloy-4, the weight percentage of nickel is limited to a maximum of 0.007% and the range of weight percentage of iron is reduced to 0.12 - 0.18% [5]. The behavior of Zircaloy-2 and Zircaloy-4 are very similar except that during high-temperature water corrosion Zircaloy-4 absorbs less hydrogen than Zircaloy-2 does [2]. Under nuclear reactor operating condition, the cladding can react with steam to form hydrogen and ZrO_2 [6]. This hydrogen can diffuse into Zr cladding to form zirconium hydrides. During the above corrosion process, cracks form [7]. The unique characteristic of the nuclear reactor environment is the presence of intense radiation [8]. Fast neutrons play an important role in irradiation damage because of their high penetration energy. This intense radiation environment will cause radiation defect structures in the cladding material [9-11]. Electronic ionization and atomic displacement are two common radiation effects. Electronic ionization is a temporary effect while atomic displacement can cause permanent damage. Specifically the absorption of neutrons in cladding will result in atomic displacements, including a thermal spike and a displacement spike and will result in producing atoms or alloying elements to alter the material properties [2, 10]. The interstitials and vacancies caused by the radiation can form clusters and dislocation loops [12-14]. Dislocation loops with interstitial character on the basal plane as well as dislocation loops with vacancy character on prismatic plane are observed in irradiated Mg [12]. In experiments by Northwood et al. of neutron irradiation damage in zirconium alloys, both interstitial and vacancy loops were found [15]. The defect structures caused by radiation can interact with other defect structures including grain boundaries and dislocations. Grain boundaries can act as sinks and sources for interstitials and vacancies. Defect clusters and dislocation loops can act as obstacles to dislocation motion. A recent in situ TEM observation of zirconium shows that dislocation loops can be eliminated by the gliding process of prismatic <a> slip [13]. Due to the behaviors described above, the easier slip plane can change from the prismatic plane to the basal plane. The change of the primary slip system is described as the dislocation channeling mechanism [13, 14]. In a nuclear reactor, the cladding also experience stress. In the corrosive, aqueous environment, stress-corrosion cracking can lead to the failure of the cladding material [16-19].

Molecular dynamics (MD) simulation has been widely used in the study of defects and microstructures in metals. MD simulations have provided significant insights into the mechanical behavior of fcc metals [20-24]. MD simulations of fcc copper showed material softening at very small grain sizes, i.e., a reverse Hall-Petch effect [20]. The simulation on nanocrystalline Al predicted twin deformation before it was identified in experiments [25, 26]. In the MD study of Al, Cu and Ni, the influences of the stacking fault energy, the unstable stacking fault energy and the unstable twin fault energy on the deformation behavior were analyzed. It was found that the stacking fault energy and, more importantly, the unstable stacking fault energy determine the dislocation behavior [24]. Although MD simulations have also been performed on hcp metals [27, 28], they have not been as extensive as in fcc metals. MD simulation of nanocrystalline Mg using an EAM potential [29] manifested the experimentally observed basal <a> dislocation and tensile twinning behaviors [28]. MD simulation of nanocrystalline 2D $[0001]$-textured Zr using the Pasianot and Monti EAM potential [30] manifested the predominant prismatic <a> dislocation and showed the Hall-Petch effect [31]. COMB is one of the two potentials that can describe systems the ionic and metallic bonding in the ZrO_2/Zr heterogeneous system;no MD simulations of the mechanical properties of the ZrO_2 and ZrO_2/Zr heterogeneous system have been performed.

In summary, understanding the deformation behaviors of the Zr and ZrO_2/Zr system is necessary in order to improve the cladding performance. Atomistic simulations can help us to better understand the deformation behaviors from the atomic point of view. Insufficient MD mechanical simulation studies have been carried out on Zr, especially ZrO_2 and ZrO_2/Zr heterogeneous system. Therefore, the mechanical properties of the Zr, ZrO_2 and ZrO_2/Zr systems are studied using molecular dynamics in this dissertation.

Project Overview

This dissertation studies the mechanical properties of Zr and ZrO_2 systems using molecular dynamics (MD) simulation method. It contains two major projects. The first project covers the mechanical response of polycrystalline Zr under tension. A 2D-textured polycrystalline model and a 3D polycrystalline model are used in the first project. The second project covers the mechanical response of Zr, ZrO_2 and ZrO_2/Zr systems under nanoindentation. The models studied in the second project are single crystals with various surface orientations. The Embedded Atom Method (EAM) potential and Charged-Optimized Many-Body (COMB) potential are used to describe the Zr system. The COMB potential is used to describe the ZrO_2 and ZrO_2/Zr systems. For Zr system, the comparison of two potentials can provide great insight on how unstable and stable stacking fault energy influence the mechanical response.

In the next chapter, the backgrounds on Zr and ZrO_2 systems, the basic dislocation theory regarding stacking fault and dislocations, and the simulation methodologies are introduced.

Objectives

This dissertation has five specific objectives:

First, to validate the potentials' ability to describe the mechanical behaviors of Zr, ZrO_2 and ZrO_2/Zr systems through mechanical simulations.

Second, to illustrate the deformation process under tension of polycrystalline Zr and under nanoindentation of Zr, ZrO_2 and ZrO_2/Zr systems.

Third, to characterize the influence of stable and unstable stacking fault energies on mechanical properties by comparing the deformation behaviors of Zr using two potentials.

Fourth, to understand the load-displacement curves and hardnesses of the Zr, ZrO_2 and ZrO_2/Zr systems.

Fifth, to determine how the presence of zirconium oxide on top of zirconium metal influences the mechanical properties, by comparing the mechanical responses of the Zr, ZrO_2 and ZrO_2/Zr systems.

CHAPTER 2
BACKGROUNDS AND SIMULATION METHODOLOGY

Zirconium and Zirconia Systems

Zirconium Metal

The ground phase of Zr belongs to hcp system and space group $P6_3/mmc$. The crystallography and low-index planes of hcp system are shown in Figure 2-1. The stacking sequence of hcp lattice is ABABAB, while for fcc lattice, the stacking sequence is ABCABC. The interatomic distance in the stacking direction is noted as a and the unit length in the stacking sequence is noted as c. The c/a ratio represents the anisotropy of the system. The ideal axial c/a ratio for hcp metals is 1.633 [32]. The deformation modes in the hcp metals are well related to the c/a ratio. For c/a>1.633 the basal plane (0001) is the most densely packed and basal slip is expected. For c/a<1.633 the prism plane is more densely packed than the basal plane, and prismatic slip is expected [33]. The predominant slip plane is also related to the d-electron configuration [34]. For instance, Ti, Zr and Hf all have 2 d-electrons and the prismatic slip is the predominant slip mode [35]. The c/a ratio of Zr is 1.593, less than the ideal ratio; accordingly, prismatic slip and pyramidal slip are frequently observed in experiments [36, 37], with prismatic <a> slip being most easily activated. The ductility of hcp metals such as Zr is severely limited because they manifest slip on only one or a few planes, typically with the slip direction along the hcp <a>-direction; as a result, according to Von Mises criterion they cannot support isotropic deformation. Homogeneous deformation could take place if usually inactive <c> or <c+a> slip processes could be activated, or if twinning with a <c> component were to play an important role in the deformation process. The most commonly observed twinning structures are $\{1\bar{1}02\}$ and $\{11\bar{2}1\}$ tensile twins and $\{11\bar{2}2\}$

compressive twins [33, 36, 37]. The slip and twinning systems in Zr as seen in experiments are presented in Table 2-1.

Texture in Zirconium Alloys

During the fabrication process of cladding tube, the Zircaloy experiences rolling and annealing [38]. The Electron Back Scattered Diffraction (EBSD) image for 25%, 50% and 75% room temperature rolled Zircaloy-2 is shown in Figure 2-2 [39]. Large volume fractions of {0002} basal plane up to 30° outward to the normal direction of rolling shown as the red region are seen in Figure 2-2. The blue region shown in Figure 2-2 represents the grains with $\{10\bar{1}0\}$ planes parallel to rolling direction. $\{01\bar{1}2\}$ planes get towards to the transverse direction shown in green in Figure 2-2. The same texture of Zircaloy is also seen in references [40-42]. The texture of rolled Zircaloy is shown schematically in Figure 2-3 [39]. Figure 2-4 shows the TEM image of room temperature rolled Zircaloy-2 after 25%, 50%, 75%, and 85% reduction respectively [39]. During the rolling process, dislocation tangles shown as arrows in Figure 2-4 and dislocation cells shown as triangles in Figure 2-4 are observed.

Zirconium Oxide

Zirconia (ZrO_2) manifests three polymorphs. The monoclinic phase (space group $P2_1/c$) is stable at room temperature, transforming to the tetragonal phase (space group $P4_2/nmc$) at 1205°C. The tetragonal phase transforms to the cubic phase (space group $Fm\bar{3}m$) at about 2370°C [43, 44]. The martensitic tetragonal to monoclinic phase transformation is the source of transformation toughening around crack tips in zirconia [45-49]. Under high pressure, the phases of zirconia transform to orthorhombic [50-52]. The generalized pressure-temperature phase diagram for ZrO_2 is shown in Figure 2-5 [50].

The cubic phase of zirconia can be stabilized at room temperature by doping, most prominently by Y_2O_3 at concentrations of 8-10 mol% [53, 54]. The phase diagram of ZrO_2-Y_2O_3 is shown in Figure 2-6. The crystal structure of cubic zirconia has the fluorite structure as shown in Figure 2-7. Its dominant slip system is ½<110>{100}; however at high temperatures or if the cubic slip is suppressed, the secondary slip systems ½<110>{110} and ½<110>{111} can be activated [54, 55]. The atomic structure of the edge dislocation ½<110>{100} is shown in Figure 2-8. It contains two extra half planes; as a result the dislocation core is charge neutral.

Oxidation of Zirconium

The oxidation of Zr and Zr alloys has been widely studied in reference [56-60]. A corrosion curve for Zircaloy-4 is shown in Figure 2-9 [61]. The oxidation process can be described as follows [58, 61]. In the initial stage of the oxidation process, the corrosion rate is fast and the formed oxide is porous [62]. Then the corrosion rate slows down and the formed oxide is dense. Then it reaches the transition point where the accelerated corrosion kinetic starts to take place. The structure of the oxide layer has been studied extensively using Raman spectroscopy [58, 60, 63-65], in which the tetragonal and monoclinic phases of zirconia are found. The tetragonal phase is located close to the interface, while the outer part of the oxide layer consists of the monoclinic phase [60, 65]. The compressive stress existing at the interface helps to stabilize the tetragonal phase [58, 64, 66]. The compressive stress decreases with the distance from the interface [67]. Moreover, cubic zirconia has been observed in oxidized Zr by electron diffraction [68-71]. In the above electron diffraction study, [110] orientation of ZrO_2 is observed. Figure 2-10 shows TEM image of oxide formation on Zr1%Fe [7]. Cracks form in the oxide layer during the oxidation process.

Dislocation Theory

Stacking Fault

In closed-pack fcc and hcp systems, the atoms can be regarded as hard spheres held together by interatomic forces. We denote one closed-pack layer as layer A. The closed-pack structure can be formed by stacking the next closed-packed layer on top of layer A at B site or C site. The FCC has ABCABC stacking order while the hcp has ABABAB stacking order. Stacking faults form when the closed-pack stacking order is disrupted. Stacking faults are classified as intrinsic or extrinsic [72]. For intrinsic stacking fault, a layer of atoms is removed from the normal stacking sequence. For extrinsic stacking faults, an additional layer of atoms is inserted to the normal stacking sequence. For the above stacking faults, the close packing is unchanged, so there is no distortion of the nearest-neighbor bonds. Due to the undistorted nearest-neighbor bond in the above stacking faults, the stacking fault energy is lower than that of grain boundaries and surfaces. In fcc, the stacking faults can be constructed by shearing the closed-pack (111) plane along certain directions. Given a perfect fcc crystal with a stacking sequence of ABCABCABCABC, if we displace B plane and all the planes above it by the vector $\frac{1}{6}[\bar{2}11]$ as shown in Equation 2-1, an intrinsic fault is formed.

$$\begin{array}{ll} \text{ABCABCABCABC} & \longrightarrow \quad \text{ABCA}\mid\text{CABCABC} \\ \phantom{\text{ABCA}}\downarrow\downarrow\downarrow\downarrow\downarrow\downarrow\downarrow\downarrow & \\ \phantom{\text{ABCA}}\text{CABCABCA} & \end{array} \qquad (2\text{-}1)$$

Furthermore, if moving all the planes below plane A by $\frac{1}{6}[\bar{2}11]$ as shown in Equation 2-2, an extrinsic stacking faults form.

$$\begin{array}{l} \mathrm{CABCA}\,\vdots\,\mathrm{CABCABC} \longrightarrow \mathrm{BCABA}\,|\,\mathrm{CABCAB} \\ \downarrow\downarrow\downarrow\downarrow \\ \mathrm{BCAB} \end{array} \qquad (2\text{-}2)$$

In addition, if we continue to displace the plane above A plane by plane by $\frac{1}{6}[\bar{2}11]$ as shown in Equation 2-3, a coherent twin is formed.

$$\begin{array}{r} \mathrm{ABCABCABCABC} \\ \downarrow\downarrow\downarrow\downarrow\downarrow \\ \mathrm{CABCA} \\ \downarrow\downarrow\downarrow\downarrow \\ \mathrm{BCAB} \\ \downarrow\downarrow\downarrow \\ \mathrm{ABC} \\ \downarrow\downarrow \\ \mathrm{CA} \\ \downarrow \\ \mathrm{B} \end{array} \;\; \begin{array}{l} \\ \\ \\ \\ \longrightarrow \mathrm{ABCABCA}\,|\,\mathrm{CBACB} \\ \\ \\ \\ \\ \\ \\ \end{array} \qquad (2\text{-}3)$$

For the hcp system with an ABABABAB stacking sequence, there are four basal planar stacking faults [73]. The I_1 stacking fault has an ABABCBCBC stacking sequence, which is achieved by removal of a basal plane and then shearing the half of the crystal along $\frac{1}{3}[10\bar{1}0]$ direction. The I_2 stacking fault has an ABABCACACA stacking sequence. It is formed by shearing half of the crystal along $\frac{1}{3}[10\bar{1}0]$ direction. If we insert an extra plane, the external fault E is formed. The stacking sequence of external fault E is ABABCABAB. For the twin-like fault T_2, the stacking sequence ABABCBABA has a twin image.

The local environment of the stacking faults structure has changed compared to the perfect crystal. The stacking fault energy (SFE) arises from this structural change [74]. The SFE γ is defined as the energy difference per unit area between the stacking fault structure and the perfect crystal structure. It can be expressed as Equation 2-4 [75].

$$\Upsilon = \frac{E_{SF} - E_0}{A} \tag{2-4}$$

E_{SF} is the energy of the structure with a stacking fault, E_0 is the energy of the perfect structure and A is the surface area.

The generalized planar fault (GPF) curve can be obtained by rigidly shearing a perfect crystal along the fault plane [24, 76, 77]. An example of the GPF is shown in Figure 2-11. The unstable stacking fault (USF) energy γ_{usf} acts as the energy barrier for dislocation motion; the stacking fault energy γ_{sf} is at the local minimum position and can be considered as a metastable state. When rigidly shearing a perfect crystal containing a pre-existing stacking fault structure, the twin fault is created [24, 78].

Partial Dislocations

For full dislocations, the atoms move from one equilibrium state to the next during the slip process. So after the dislocation glides, it leaves an unchanged perfect crystal structure. The Burgers vector of the full dislocation is usually the shortest atom-to-atom lattice translation vector. For a partial dislocation, the surrounding environment is not entirely the original lattice structure and the Burgers vector of the partial dislocation is not a regular lattice translation vector [79]. The reason for the formation of a partial dislocation is that atoms move through a smaller misfit energy indirect path instead of the high misfit energy direct path, which obeys the Frank's Energy Criterion. According to Frank's Energy Criterion, the dislocation will dissociate into partial dislocations when the total energy of the partials is less than the energy of the original dislocation. In an fcc stacking structure as shown in Figure 2-12, the perfect dislocation $\frac{1}{2}[\bar{1}01]$ requires atom to be displaced from B_1 to B_2. However, the displacement along $\frac{1}{2}[\bar{1}01]$ direct path creates larger misfit energy. In order to minimize the required energy, atom prefers to move from B_1 to C to B_2, a lower energy path. The $\frac{1}{6}\langle 112\rangle$ dislocations are called Shockley partials. Because the glide plane of the Shockley partials is in the plane of fault, they are glissile dislocations. The dissociation of the perfect dislocation $\frac{1}{2}\langle 1\bar{1}0\rangle$ can be described as $\frac{1}{2}\langle 1\bar{1}0\rangle \rightarrow \frac{1}{6}\langle 2\bar{1}\bar{1}\rangle + \frac{1}{6}\langle 1\bar{2}1\rangle$. A dislocation consisting of two Shockley partials and an enclosed stacking fault is called an extended dislocation. The structure of the extended dislocation is shown in Figure 2-13.

Simulation Methodology

Introduction to Computational Method

Computational methods can be categorized based on their length and time scales, see Figure 2-14. Density functional theory (DFT) [80, 81] and molecular dynamics (MD) [82] simulation are classified as atomic-level modeling methods. DFT, based on quantum mechanics, is capable of calculating the physical and electronic structure of materials. The system size of DFT calculations usually ranges from a few atoms to a few hundreds of atoms. MD predicts the trajectories of atoms by numerically solving Newton's equations of motion. MD simulation can deal with systems with up to millions (or even billions) of atoms. The length and time scales of MD simulations are on the order of nm and ps. If longer length and time scales are needed, mesoscale and continuum methods can be applied. Computational models with different length and time scales can be linked together to achieve multi-scale modeling.

In this dissertation, MD simulation is used to study the mechanical properties of Zr, ZrO_2 and ZrO_2/Zr systems. The following provides the background of MD simulations and interatomic potentials.

Molecular Dynamics

Molecular dynamics simulation is a computational method that predicts the trajectories of atoms and molecules by solving Newton's Equation of motion [83]:

$$\boldsymbol{F}_i = m_i \frac{d^2 \boldsymbol{r}_i}{dt^2} = -\frac{\partial E}{\partial r_i} \tag{2-5}$$

where $\boldsymbol{F}_i$ is the force on atom i, m_i is its mass and $\boldsymbol{r}_i$ is its position; t is the time and E is the total energy. The force is determined from the potential energy. Thus a high-quality interatomic potential is essential to get reasonable simulation results.

Time integration

The time integration algorithm is the engine of the MD simulation [84]. The time step δt is defined as the finite time increment between consecutive particle positions. Truncation errors and round-off errors are two common errors associated with the integration scheme. Truncation errors are associated with the algorithm. The round-off errors are due to the computer's finite precision. The Verlet algorithm [85], leap-frog algorithm, velocity Verlet and predictor-corrector algorithms are commonly used integration methods for MD [83, 86].

In the integration algorithm, the positions, velocities and accelerations are predicted by Taylor series expansion:

$$\vec{r}(t+\delta t) = \vec{r}(t) + \vec{v}(t)\delta t + \frac{1}{2}\vec{a}(t)\delta t^2 + \cdots \tag{2-6}$$

$$\vec{v}(t+\delta t) = \vec{v}(t) + \vec{a}(t)\delta t + \frac{1}{2}\vec{b}(t)\delta t^2 + \cdots \tag{2-7}$$

$$\vec{a}(t+\delta t) = \vec{a}(t) + \vec{b}(t)\delta t + \cdots \tag{2-8}$$

where $\vec{r}$ is the position, $\vec{v}$ is the velocity, $\vec{a}$ is the acceleration, and $\vec{b}$ is the third derivatives of the position with respect to time t. δt is the time step. The time step should be at least an order of magnitude smaller than the fastest motion in the system. In a molecular system, the vibrational frequencies correspond to a time period of ~10fs and the optical phonon frequencies correspond to a time period of ~100fs. So the typical time step in MD simulation is on the order of a fs.

For the Verlet algorithm, the new atomic position at time t+δt is calculated using positions and accelerations at time t and the positions from time t- δt. We can write the Verlet algorithm as

$$\vec{r}(t+\delta t) = \vec{r}(t) + \vec{v}(t)\delta t + \frac{1}{2}\vec{a}(t)(\delta t)^2 + \frac{1}{6}\vec{b}(t)(\delta t)^3 + \mathcal{O}((\delta t)^4) \tag{2-9}$$

$$\vec{r}(t-\delta t) = \vec{r}(t) - \vec{v}(t)\delta t + \frac{1}{2}\vec{a}(t)(\delta t)^2 - \frac{1}{6}\vec{b}(t)(\delta t)^3 + \mathcal{O}((\delta t)^4) \tag{2-10}$$

Summing Equation 2-9 and Equation 2-10, Equation 2-11 is obtained

$$\vec{r}(t+\delta t) = 2\vec{r}(t) - \vec{r}(t-\delta t) + \vec{a}(t)(\delta t)^2 + \mathcal{O}((\delta t)^4) \tag{2-11}$$

From Equation 2-11, the error is of order $(\delta t)^4$.

For the Leap-frog algorithm, the velocity at half of the time step is calculated. Then this average velocity is used to calculate the position $\vec{r}$ at t+δt. The Leap-frog algorithm is described as

$$\vec{r}(t+\delta t) = \vec{r}(t) + \vec{v}\left(t+\frac{1}{2}\delta t\right)\delta t \tag{2-12}$$

$$\vec{v}\left(t+\frac{1}{2}\delta t\right) = \vec{v}\left(t-\frac{1}{2}\delta t\right) + \vec{a}\delta t \tag{2-13}$$

Although the velocities in Leap-frog algorithms are explicitly calculated, the time integration is not reversible.

Thermostat

Molecular dynamics simulation usually involves temperature control by regulating the velocity of each atom. There are many methods available for temperature control, including velocity-rescaling [83], the Berendsen algorithm [87], the Nosé-Hoover algorithm [88] and the Langevin algorithm [89-91].

Velocity rescaling method is the easiest and most straightforward way to control temperature. The distribution of velocities can be described by Maxwell-Boltzmann distribution as

$$P\left(v_{i,\alpha}\right) = \left(\frac{m}{2\pi k_B T}\right)^{\frac{1}{2}} e^{-\frac{m v_{i,\alpha}^2}{2k_B T}} \tag{2-14}$$

where $v_{i,\alpha}$ is the velocity of atom i in α(x,y,z) direction.

From Equation 2-14, the relationship between kinetic energy $E_{kinetic}$ and the temperature T can be obtained.

$$k_B T(t) = \frac{1}{N_f} \sum_{i,\alpha} m v_{i,\alpha}^2 \tag{2-15}$$

where N_f is the number of degrees of freedom. $T(t)$ fluctuates due to the randomly generated velocities. In order to keep $T(t) = T$, the velocities can be rescaled as

$$v'_{i,\alpha} = \sqrt{\frac{T}{T(t)}} v_{i,\alpha} \tag{2-16}$$

The velocity-rescaling method is very simple to implement. However it has a few disadvantages [92]: it does not correspond to a well-defined thermodynamic ensemble and it is not time reversible because the energy and momentum are not conserved [93].

In this dissertation, the Berendsen and Langevin thermostats are used. The following is the brief description of Berendsen thermostat.

The Berendsen thermostat scales the velocities at each time step, such that the temperature change rate is proportional to the temperature difference:

$$\frac{dT(t)}{dt} = \frac{1}{\tau}(T_0 - T(t)) \tag{2-17}$$

where T_0 is the external heat bath. τ is the coupling parameter that determines how tightly the bath and the system are coupled together.

The temperature change between successive time steps is

$$dT = \frac{dT}{\tau}(T_0 - T) \tag{2-18}$$

Thus the velocity can be rescaled as

$$v'(t) = \lambda v(t) \tag{2-19}$$

$$\lambda = \left(1 + \frac{dt}{\tau_T}\left(\frac{T_0}{T} - 1\right)\right)^{\frac{1}{2}} \tag{2-20}$$

where τ_T is the coupling time constant that determines how fast the system can reach the desired temperature. λ is the rescaling factor.

In the Langevin thermostat, a random force is applied to the particles at each time step and the velocities are controlled by a viscous drag force [94]. The equation of motion can be describe as

$$m\frac{d\vec{v}_i}{dt} = -\frac{\delta U}{\delta \vec{r}_i} - m\Gamma\vec{v}_i + \sigma W_i \tag{2-21}$$

where Γ is a friction coefficient that determines the viscous drag force and σW_i is the random force. The fluctuation-dissipation relation can be described as

$$\sigma^2 = 2\Gamma \mathrm{m} k_B T \tag{2-22}$$

Barostats

In MD simulations, the simulation cell is usually held under constant pressure conditions. In addition, for mechanical tests using MD, stresses or strains are applied to the simulation cell. Under the influence of stress or strain, the size or shape of the simulation cell needs to change accordingly. Barostats are applied in order to allow the size or shape of the simulation cell to change. The Andersen barostat [95] and the Parrinello-Rahman barostat [96] are two widely used barostats scheme used in MD simulation. The Andersen barostat allows isotropic expansion or contraction. Parrinello and Rahman extended the Anderson barostats to allow anisotropic expansion or contraction, and shear of the simulation cell.

The Anderson barostat mimics the action of pistons with a mass M compressing on the simulation cell in three principle directions. The kinetic and potential energy of the piston is described as

$$E_{V,kin} = \frac{1}{2} M \left(\frac{dV}{dt}\right)^2 \tag{2-23}$$

$$E_{V,pot} = P_1 V \tag{2-24}$$

where V is the volume and P_1 is the external pressure acting on the piston.

Then the coordinates r_i is replaced by the scaled coordinates ρ_i

$$\rho_i = \frac{r_i}{V^{\frac{1}{3}}} \tag{2-25}$$

where V is the volume. Then the kinetic and potential energy of the simulated unscaled system can be obtained as

$$E_{kin,i} = \frac{1}{2} V^{\frac{2}{3}} m_i \left(\frac{d\vec{\rho}_i}{dt}\right)^2 \tag{2-26}$$

$$U_i = U(V^{\frac{1}{3}} \vec{\rho}_i) \tag{2-27}$$

The new Lagrangian can be written as

$$L = E_{V,kin} + E_{V,pot} + E_{kin,i} + U_i \tag{2-28}$$

$$L\left(\rho^N, \dot{\rho}^N, V, \dot{V}\right) = \frac{1}{2} V^{\frac{2}{3}} \sum_{i=1}^{N} m_i \left(\frac{d\vec{\rho}_i}{dt}\right)^2 - \sum_{i<j=1}^{N} U(V^{\frac{1}{3}} \vec{\rho}_{ij}) + \frac{1}{2} M \left(\frac{dV}{dt}\right)^2 - P_1 V \tag{2-29}$$

The equation of motions under the Andersen scheme is then obtained as

$$\frac{d\mathbf{r}_i}{dt} = \frac{\mathbf{P}_i}{m_i} + \frac{1}{3}\mathbf{r}_i \frac{d\ln V}{dt} \tag{2-30}$$

$$\frac{d\mathbf{P}_i}{dt} = -\sum r_{i,j}\, U'(\mathbf{r}_{ij}) - \frac{1}{3}\mathbf{P}_i \frac{d\ln V}{dt} \tag{2-31}$$

$$\frac{Md^2V}{dt^2} = P_1 + \left(\frac{2}{3}\sum \frac{\mathbf{P}_i^2}{2m_i} - \frac{1}{3}\sum\sum r_{i,j}\, U'(\mathbf{r}_{ij})\right)/V \tag{2-32}$$

Parinello and Rahman extended the Andersen barostat to allow the change of shape of the simulation cell by expressing the volume using a 3×3 matrix H. The volume the position can be expressed as

$$r_i = \mathrm{H}\mathrm{s}_i = a_1\mathrm{a} + a_2\mathrm{b} + a_3\mathrm{c} \tag{2-33}$$

where a_1, a_2, a_3 are the components of a column vector s_i.

The Lagrangian can be written as

$$L = \frac{1}{2}\sum m_i\, \dot{\mathrm{s}}_i^T (\mathrm{H}^T H)\mathrm{s}_i - \sum\sum U(r_{ij}) + \frac{1}{2}MTr(\dot{\mathrm{H}}^T\dot{\mathrm{H}}) - pV \tag{2-34}$$

The Andersen and Parrinello-Rahman barostats are both used in this project.

Ensembles

In MD simulation, the temperature and the pressures of the simulated system need to be controlled in order to create appropriate experimental condition. Number of atoms (N), energy (E), volume (V), temperature (T) and pressure (P) are state variables. Some of the state variables can be controlled to generate certain thermodynamic ensembles. The microcanonical ensemble (NVE), canonical ensemble (NVT) and isothermal-isobaric ensemble (NPT) are among most important thermodynamic ensembles in MD simulation [83]. In the NVE ensemble, the energy is conserved. The system is isolated, thus there is no pressure and temperature control. The NVT ensemble is not recommended for equilibration because it does not allow the dimensions of the simulation cell to evolve freely. The temperature of the system is kept constant during the simulation. For the NPT ensemble, the temperature and pressure of system are defined. The NPT ensemble is capable of achieving desired temperature and pressure. The NVT, NPT and NVE ensembles are all used in this study.

Interatomic Potential

The interatomic potential describes the potential energy of system arising from the atomic configurations [97]. The mathematical function of the potential usually depends on the bonding type within the system. One major frontier of potential development is to establish a unified framework to describe metallic, ionic and covalent bonding types [98, 99]. In this dissertation, an Embedded Atom Method (EAM) potential and a Charge-Optimized Many Body (COMB) potential are used. The EAM potential is usually used to describe metallic system, while the COMB potential is capable of describing systems of different bonding types, including metallic and ionic bonding, within a unified framework.

EAM Potential

The Embedded Atom Method (EAM) potential was first proposed by Daw and Baskes [100, 101]. The total energy of the system can be expressed as

$$E_{total} = \frac{1}{2}\sum_{i,j}\phi(r_{i,j}) + \sum_i F(\bar{\rho}_i) \qquad (2\text{-}35)$$

$$\bar{\rho}_i = \sum_j \rho(r_{ij}) \qquad (2\text{-}36)$$

where $\phi(r_{i,j})$ is the pairwise interaction between atom i and j, $r_{i,j}$ is the scalar distance between atom i and j. $\rho(r_{ij})$ is the electronic density as a function of distance from the nucleus of atom i. Then $\bar{\rho}_i$ is the electronic density of the host system with atom i removed. $F(\bar{\rho}_i)$ is the quantum mechanical energy when atom i is embedded into $\bar{\rho}_i$ [102]. It acts as the ‘embedding function’ of atom i.

Mendelev and Ackland (MA) develop a Zr potential using EAM formalism [103]. The MA EAM potential is used to study the mechanical properties of Zr.

COMB Potential

The COMB potential is a variable-charge reactive potential formalism. Reactive potentials can describe the dissociation and creation of chemical bonds [104, 105]. The bond-order concept [106-112] is one of the foundations of COMB potential [105]. Unlike traditional potentials, the COMB potential allows dynamic charge adjustment according to the local environment, and is based on self-consistent charge equilibration approach [105, 113, 114]. Thus the COMB potential can simulate complex structures and changing bond environments such as heterogeneous interfaces [115]. The COMB potential used in this dissertation is the third generation [104]. The first generation was developed by Yu et al. by modifying Yasukawa [116] potential [117]. Devine et al. modify the formalism of the first generation COMB to become the second generation COMB [118].

For the third generation COMB (COMB3), the total energy is described as

$$U_{tot} = U_{es} + U_{short} + U_{vdw} + U_{corr} \tag{2-37}$$

$$U_{es} = U_{self} + U_{coul} + U_{polar} \tag{2-38}$$

where E_{es} is the electrostatic energy term. As shown in Equation 2-38, it consists of a self-energy term (U_{self}), a Coulomb term (U_{coul}) and a term to describe self-dipole, dipole-dipole and charge-dipole interactions (U_{polar}). The concept of the electrostatic energy comes from ES+ potential proposed by Streitz and Mintmire [114]. E_{short} is the short range interaction term. E_{vdw} is the van der Waals energy term, which is non-bonding interaction. U_{corr} is the correction term. It is used to correct the energies associated with bond angles.

In the electrostatic energy term, U_{self} is the energy required when a charge is formed on an isolated atom, which can be described as

$$U_{self}[\{q\},\{r\}] = \sum_i \left[V_i^{ioniz}(q_i) + V_i^{field}(q_i, r_{ij})\right]$$ (2-39)

$$V_i^{ioniz}(q_i) = E_i^0(0) + \chi_i q_i + J_i q_i^2 + \mathrm{K}_i q_i^3 + L_i q_i^4 + L^{barr}\left(q_i - q_i^{lim}\right)q_i^4$$ (2-40)

$$V_i^{field} = \frac{1}{2\pi\varepsilon_0} \sum_{j>1}^{NN} \left(\frac{P_{ij}^{\chi}}{r_{ij}^3} + \frac{P_{ij}^{J} q_j^2}{r_{ij}^5}\right)$$ (2-41)

where q_i is the charge on the i^{th} atom and r_{ij} is the distance between atoms i and j. $V_i^{ioniz}(q_i)$ is the energy required to form a charge on an isolated atom. V_i^{field} reflects the change of the electronegativity and atomic hardness of the atom when it is in a molecule or ionic lattice. In the $V_i^{ioniz}(q_i)$ term, χ represents the electronegativity and J is associated with the chemical hardness. $L^{barr}\left(q_i - q_i^{lim}\right)q_i^4$ is used to keep the charge of the atom within physically sensible charge limits. In Equation 2-41, P^{χ} and P^{J} are associated with the specific bond type.

In the electrostatic energy term, U_{coul} term contains the charge-charge interactions ($U^{qq}[\{q\},\{r\}]$) and charge-nuclear interactions ($U^{qZ}[\{q\},\{r\}]$), which can be expressed as

$$U^{qq}[\{q\},\{r\}] = \sum_i \sum_{j>1} q_i J_{ij}^{qq} q_j$$ (2-42)

$$J_{ij}^{qq} = \left[\rho_i | \rho_j\right] = \int d^3 r_1 \int d^3 \frac{\rho_i(r_1)\rho_j(r_2)}{r_{12}}$$ (2-43)

$$U^{qZ}[\{q\},\{r\}] = \sum_i \sum_{j>i} \left(q_i J_{ij}^{qZ} Z_j + q_j J_{ji}^{qZ} Z_i\right)$$ (2-44)

$$J_{ij}^{qZ} = [j|\rho_i] - \left[\rho_j | \rho_i\right]$$ (2-45)

$$[j|\rho_i] = \int d^3 r \frac{\rho_i(r)}{|\mathbf{r} - \mathbf{r}_i|}$$ (2-46)

where Z is the core charge. ρ is the charge density, which is based on S-type Slater orbitals [119]. **r** represents the center of charge density and r_{12} is the distance between charge density distribution. J_{ij}^{qq} is the Coulomb integral operator and J_{ij}^{qZ} is the charge-nuclear coupling operator.

In the electrostatic energy term, U_{polar} represents self-dipole, dipole-dipole and charge-dipole interactions, which correspond to the three terms on the right hand of Equation 2-47, respectively. It can be expressed as

$$U^{polar}[\{q\},\{\mathrm{r}\}] = \sum_i \frac{\vec{\mu}_i^2}{2P_i} + \sum_i \vec{\mu}_i \vec{E}_i^q + \sum_i \sum_{j>i} \vec{\mu}_i T_{ij} \vec{\mu}_j \tag{2-47}$$

where $\vec{\mu}$ is the dipole moment caused by the electric field $\vec{E}$. P_i is the polarizability tensor. T_{ij} is the damped dipole field tensor that diminishes as atoms overlap.

In the COMB formalism, the short range interaction term contributes the most to capture the complex physics and chemistry. The short range interaction term consists of a pair-wise repulsive term, $V^R(r_{ij}, q_i, q_j)$ and a pairwise attractive term, $V^A(r_{ij}, q_i, q_j)$. The short range interaction term is the bond-order term, which can be described as

$$U^{short}[\{q\},\{r\}] = \sum_i \sum_{j>i} \{F_c(r_{ij})[V^R(r_{ij}, q_i, q_j) - b_{ij} V^A(r_{ij}, q_i, q_j)]\} \tag{2-48}$$

where (r_{ij}, q_i, q_j) is the cutoff function. b_{ij} is the bond-order term that modifies the attractive energy contributed by coordination, bond angle, torsion and conjugate effect.

The pairwise repulsive and attractive term can be expressed as

$$V^R(q_i, q_j, r_{ij}) = A_{ij} \times \exp\left\{-\lambda_{ij} r_{ij} + \frac{1}{2}[\lambda_{ii} D_i(q_i) + \lambda_{jj} D_j(q_j)]\right\} \tag{2-49}$$

$$V^A\left(q_i, q_j, r_{ij}\right) = B_{ij} B_{ij}{}^*\left(q_i q_j\right) \times \exp\left\{-a_{ij} r_{ij} + \frac{1}{2}\left[a_{ii} D_i(q_i) + a_{jj} D_j\left(q_j\right)\right]\right\} \tag{2-50}$$

where A_{ij}, B_{ij}, λ_{ij}, and a_{ij} have default values based on the bond type. r_{ij} is the distance between atoms. $D_i(q_i)$ is the charge dependent correction function. $B_{ij}{}^*\left(q_i q_j\right)$ is the charge dependent function.

$D_i(q_i)$ is the element related,

$$D_i(q_i) = D_{\mathrm{U}_i} + |b_{D_i}\left(Q_{\mathrm{U}_i} - q_i\right)|^{n_{D_i}} \tag{2-51}$$

$$b_{D_i} = \frac{\left(D_{\mathrm{L}_i} - D_{\mathrm{U}_i}\right)^{1/n_{D_i}}}{\left(Q_{\mathrm{U}_i} - Q_{\mathrm{L}_i}\right)} \tag{2-52}$$

$$n_{D_i} = \frac{\ln D_{\mathrm{U}_i} - \ln\left(D_{\mathrm{U}_i} - D_{\mathrm{L}_i}\right)}{\ln\left(Q_{\mathrm{U}_i} - Q_{\mathrm{L}_i}\right)} \tag{2-53}$$

where D_{U} and D_{L} are parameters that reflect the change in atomic radius with charge; Q_{U} and Q_{L} are the atomic charges that correspond to the limits of the valence shell.

The charge dependent function ($B_{ij}{}^*\left(q_i q_j\right)$) is used to control the change in bond order with charge,

$$B_{ij}{}^*\left(q_i q_j\right) = \left(B_i{}^* B_j{}^*\right)^{\frac{1}{2}} \tag{2-54}$$

$$B_i{}^* = \left[a_{B_i} - \left|b_{B_i}\left(q_i - Q_{O_i}\right)\right|^{n_{B_i}}\right] \tag{2-55}$$

$$b_{B_i} = \frac{\left|a_{B_i}\right|^{\frac{1}{n_{B_i}}}}{\Delta Q_i} \tag{2-56}$$

$$a_{B_i} = \left(1 - \left|\frac{Q_{O_i}}{\Delta Q_i}\right|^{n_{B_i}}\right)^{-1} \tag{2-57}$$

$$\Delta Q_i = \frac{1}{2}\left(Q_{\mathrm{U}_i} - Q_{\mathrm{L}_i}\right) \tag{2-58}$$

$$Q_{O_i} = \frac{1}{2}\left(Q_{\mathrm{U}_i} - Q_{\mathrm{L}_i}\right) \tag{2-59}$$

where n_{B_i} is equal to 10 for all elements.

The bond order term, b_{ij}, in Equation 2-48 modifies the short-range attraction based on the coordination, bond angle, torsion and conjugation

$$b_{ij} = \left\{1 + \left[\sum\nolimits_{k \neq i,j}^{N} \left[F_c(r_{ik})\left(r_{ij}, R_{ij}^{min}, R_{ij}^{max}\right)\zeta\left(r_{ij}, r_{jk}\right) g_{ij}\left(\cos\theta_{ijk}\right)\right] + P_{ij}(N_i^1, N_i^2, \cdots)\right]^{\eta_i}\right\}^{\frac{-1}{2\eta_i}} \tag{2-60}$$

Function $\zeta\left(r_{ij}, r_{jk}\right)$ is the screening function:

$$\zeta\left(r_{ij}, r_{jk}\right) = \exp\left[\beta_{ij}^{mi}\left(r_{ij} - r_{ik}\right)^{mi}\right] \tag{2-61}$$

The screening function weakens the longer bonds.

Function $g_{ij}\left(\cos\theta_{ijk}\right)$ is the angular function:

$$g_{ij}\left(\cos\theta_{ijk}\right) = \sum\nolimits_{n=0}^{6} b_{ij}^{n} \cos\theta_{ijk}^{n} \tag{2-62}$$

The angular function is a sixth-order polynomial.

The coordination function $\left(P_{ij}\right)$ is given by

$$P_{ij} = c_1\Omega_i + c_2\exp(c_3\Omega_i) + c_4 \tag{2-63}$$

where Ω_i is the total number of neighbors of the center atom i.

Function $F_c(r_{ik})$ is the cut-off function:

$$F_c\left(r_{ij}, R_{ij}^{min}, R_{ij}^{max}\right) = \begin{cases} 1 & r_{ij} \leq R_{ij}^{min} \\ \frac{1}{2}\left[1 + \cos\left(\pi\frac{r_{ij} - R_{ij}^{min}}{R_{ij}^{max} - R_{ij}^{min}}\right)\right] & R_{ij}^{min} < r_{ij} \leq R_{ij}^{max} \\ 0 & r_{ij} > R_{ij}^{max} \end{cases} \tag{2-64}$$

The last component of the total energy is the van der Waals interaction. The van der Waals interaction can be described by traditional Lennard-Jones formula [120]:

$$U^{vdw}[\{r\}] = \sum_i \sum_{j>i}^{NN} 4\varepsilon_{ij}^{vdw} \left[\left(\frac{\sigma_{ij}^{vdw}}{r_{ij}} \right)^{12} - \left(\frac{\sigma_{ij}^{vdw}}{r_{ij}} \right)^{6} \right] \tag{2-65}$$

The COMB potential is used to study the deformation behaviors of Zr and ZrO_2 system in this dissertation. The COMB potential is especially suitable for studying metal and metal oxide interface such as Zr and ZrO_2 interface in this study.

Simulation Analysis Tools

Visualization software OVITO [121] and AtomEye [122] are used to visualize the simulation results. The Crystal Analysis Tool [123-125] is used for analyzing the defect structures. The Crystal Analysis Tool developed by Stukowski is capable of identifying lattice and defect structures, identifying dislocation directions and their corresponding Burgers vectors achieved the by Dislocation Extraction Algorithm (DXA), and computing the atomic-level elastic and plastic deformation gradient fields [123-125].

In order to analyze the deformation process, Common Neighbor Analysis (CNA) [126, 127] is used to distinguish atoms in hcp, fcc and other environments. With the help of CNA, the dislocation lines and stacking fault structures can be easily visualized.

Table 2-1. Slip and twinning systems of Zr [33, 37].

Properties	Zr
Slip system	Predominant prismatic <a>
	Secondary basal <a>, pyramidal <c+a>
Twin system	Tensile twin $\{1\bar{1}02\}$ $\{11\bar{2}1\}$
	Compressive twin $\{11\bar{2}2\}$

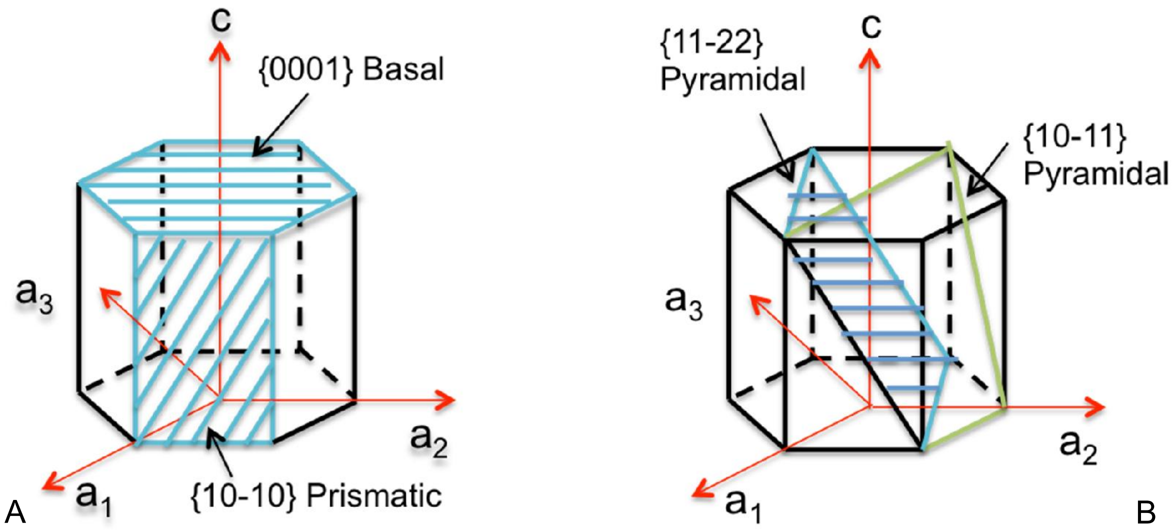

Figure 2-1. Planes in hcp system. A) Basal and prismatic planes in hcp. B) First and second order pyramidal planes.

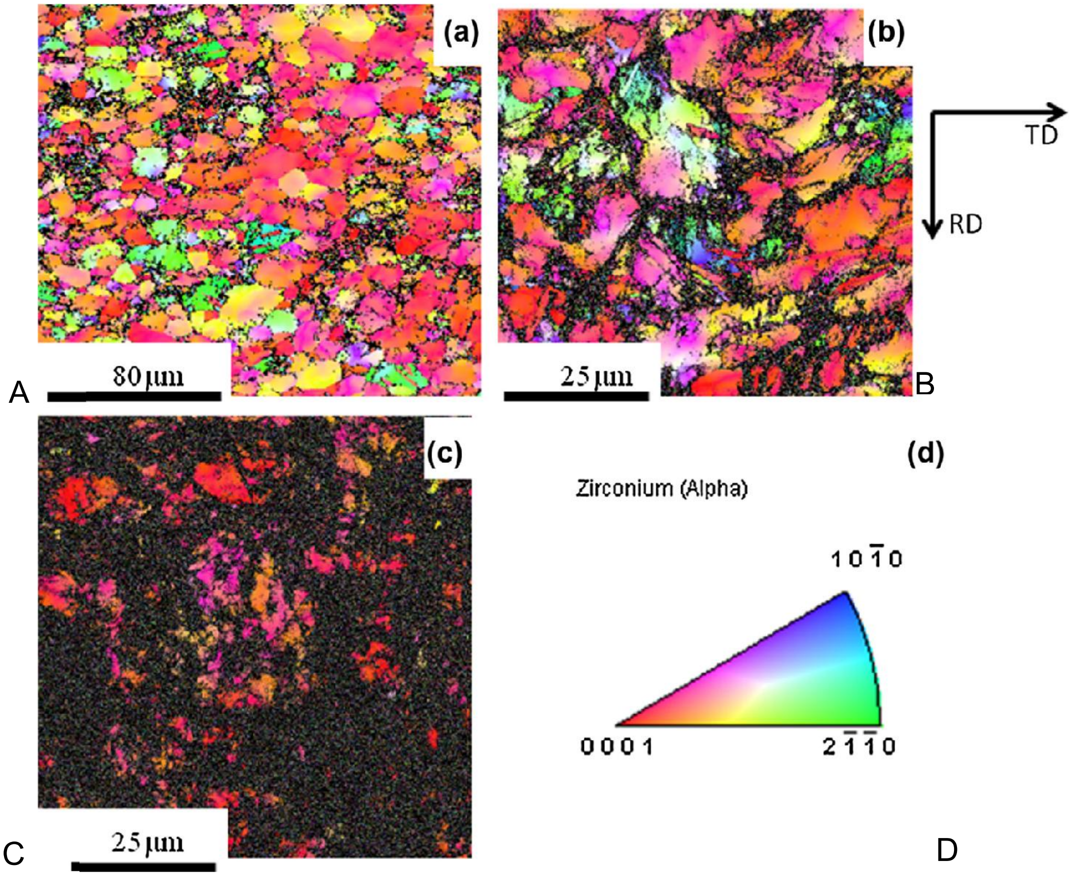

Figure 2-2. EBSD image for room temperature rolled Zircaloy-2. A) 25%reduction. B) 50% reduction. C) 75% reduction. The dark regions are completely deformed. (from reference [39])

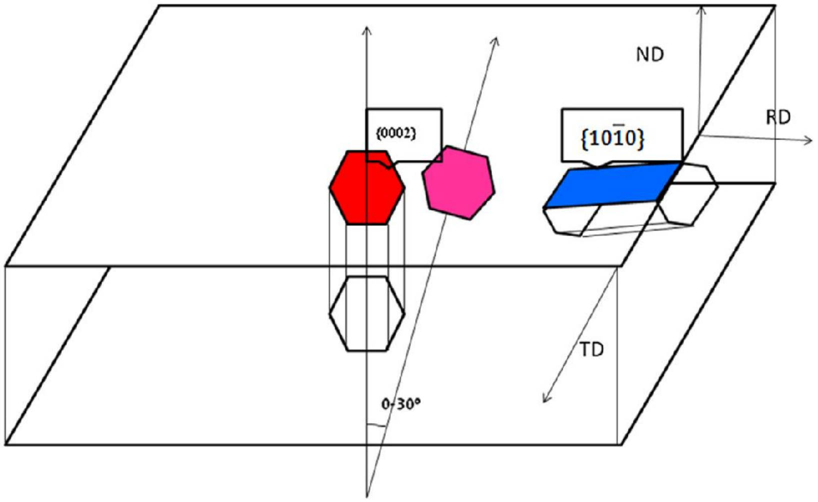

Figure 2-3. Schematic of orientation of planes after rolling for Zircaloy-2. (from reference [39])

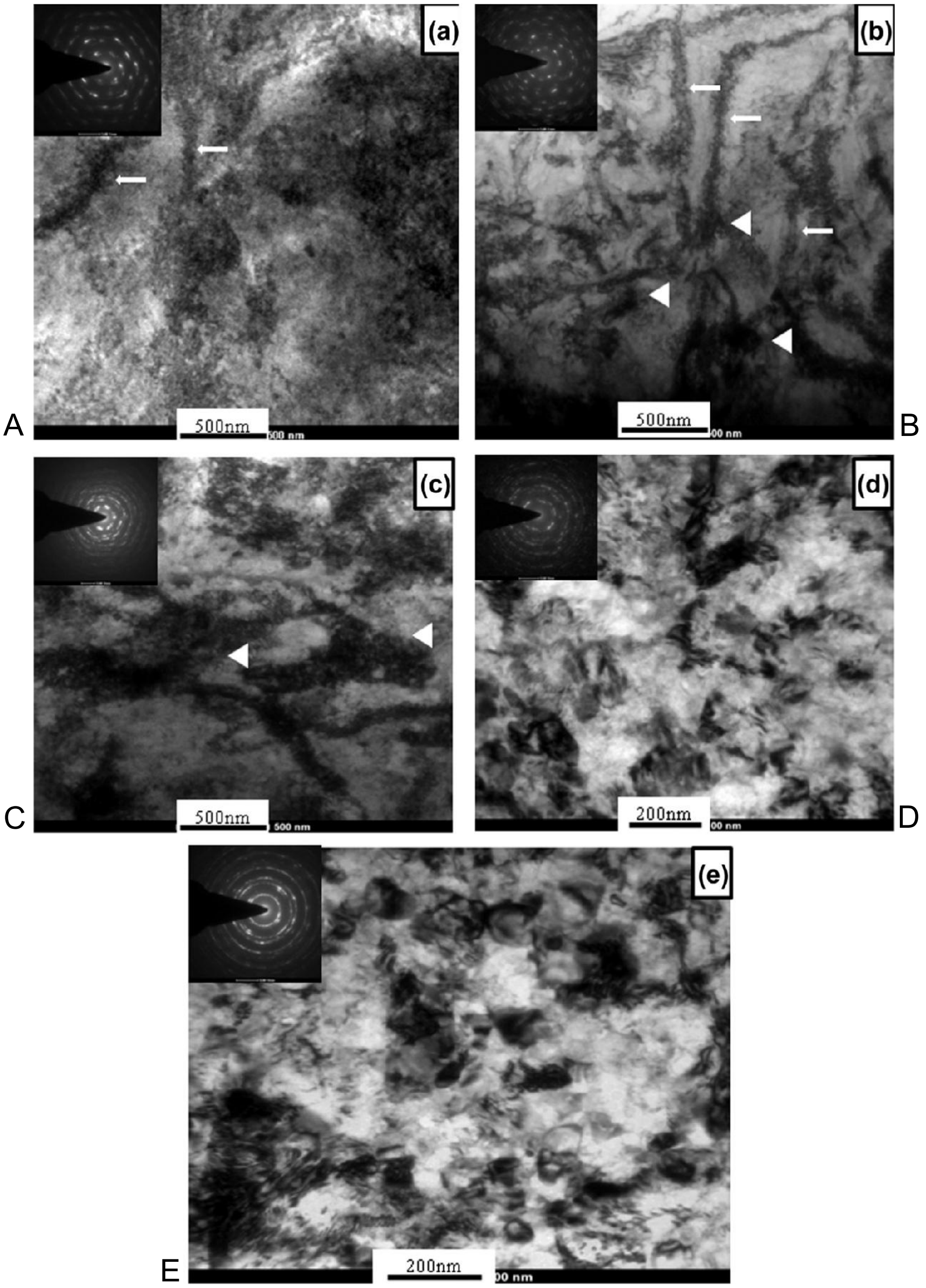

Figure 2-4. TEM image of room temperature rolled Zircaloy-2. A) 25% reduction. B) 50% reduction. C) 75% reduction. D) 85% reduction. E) Annealing at 400 °C for 30 minutes after 85% reduction. (from reference [39])

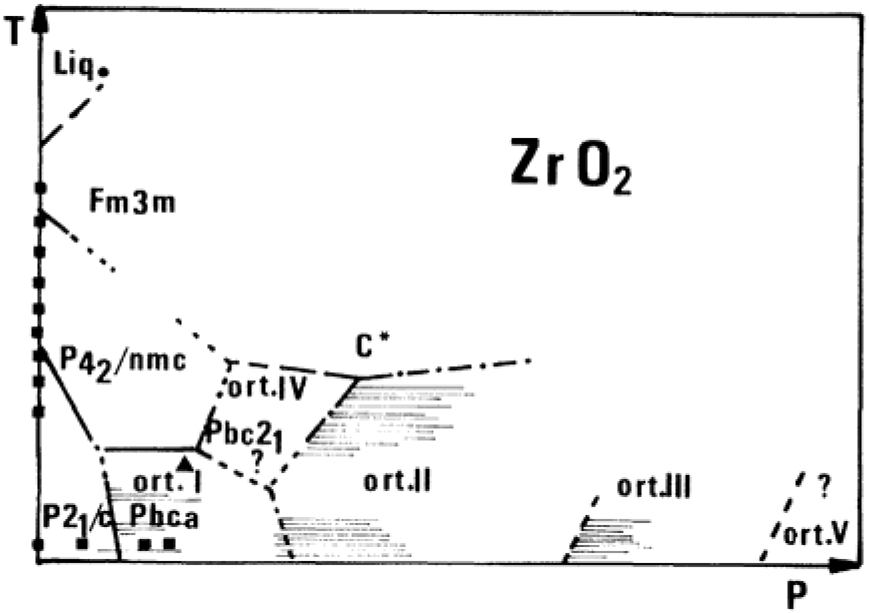

Figure 2-5. Generalized pressure-temperature phase diagram from ZrO_2. (from reference [50]

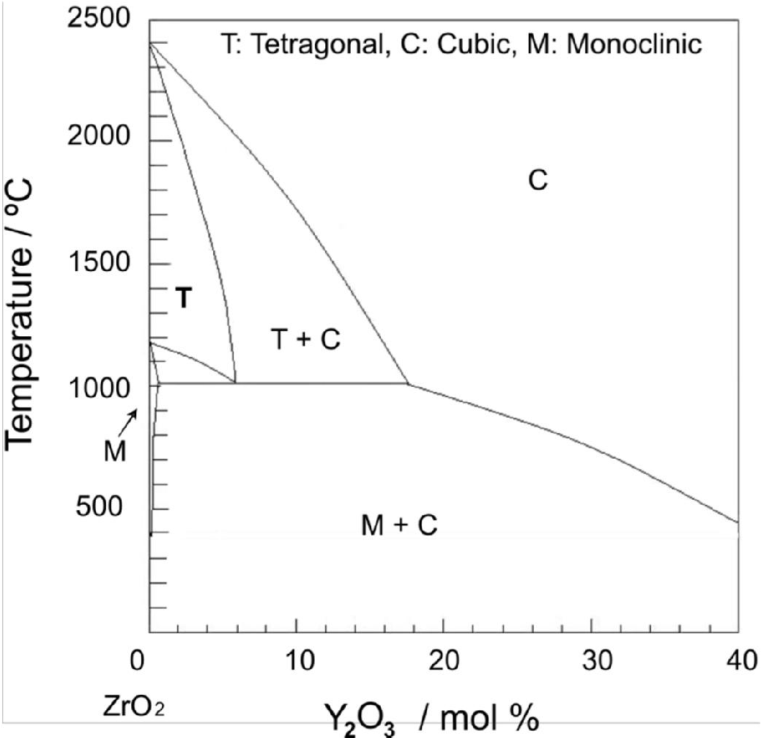

Figure 2-6. Phase diagram of the ZrO_2-Y_2O_3 system [128, 129].

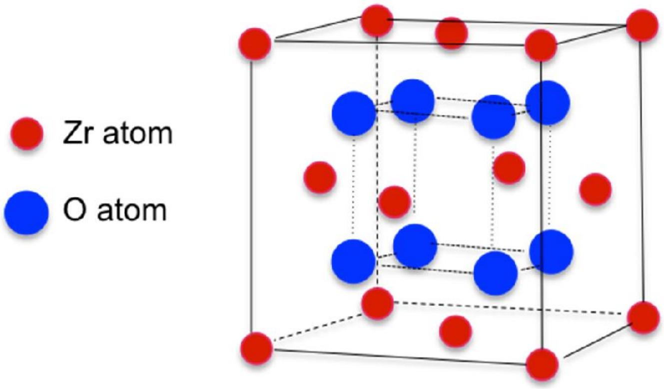

Figure 2-7. Unit cell of ZrO_2 fluorite structure.

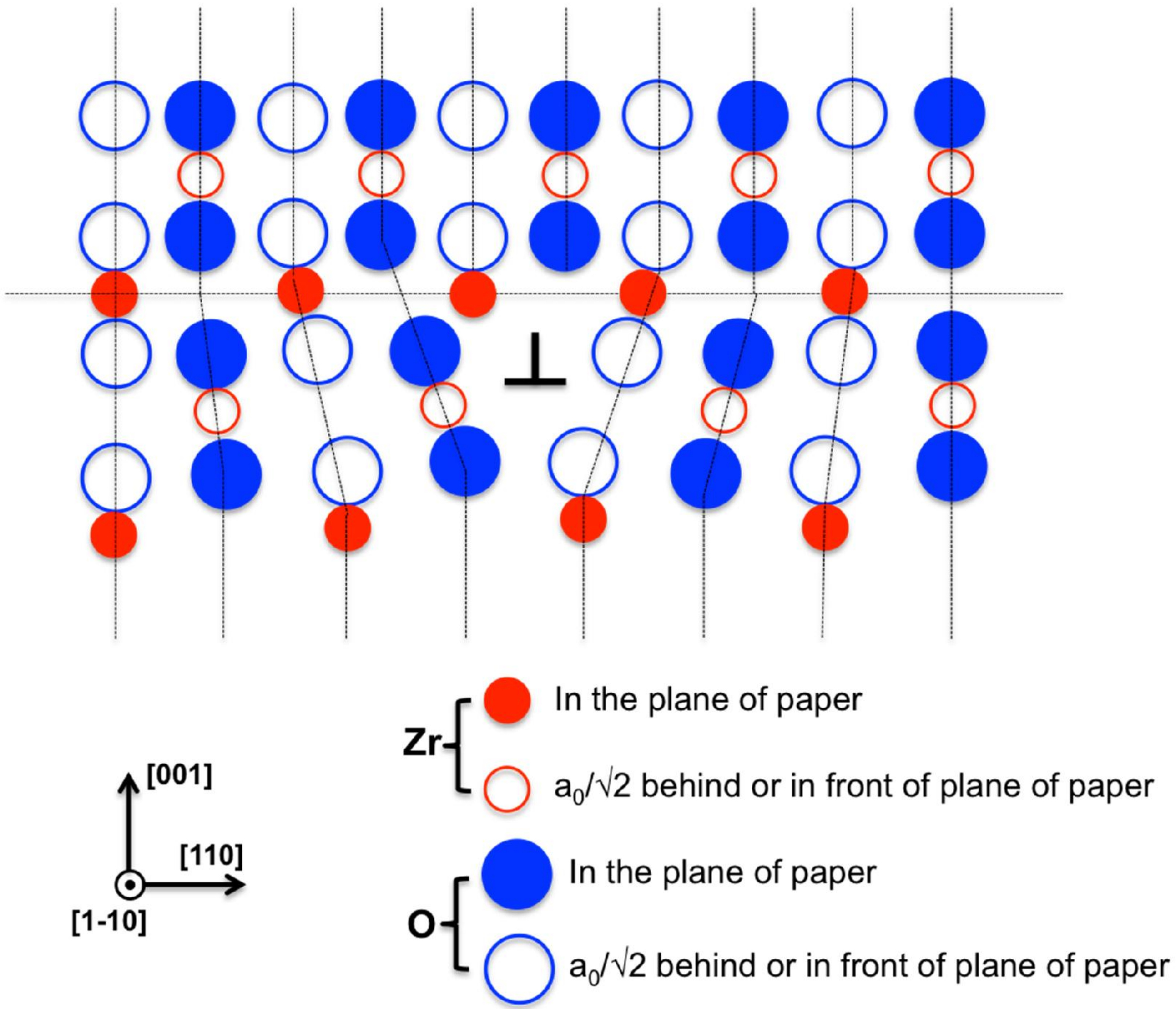

Figure 2-8. Schematic of edge dislocation in the fluorite structure. The glide plane is (001) and the Burgers vector is (1/2) [110] [130].

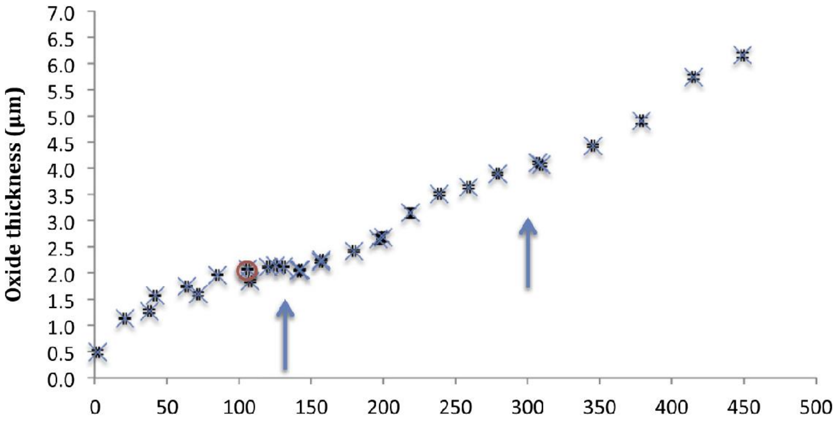

Figure 2-9. Corrosion curve for Zircloy-4 exposed to simulated PWR conditions at 350 °C. The transitions in corrosion kinetics are denoted by the arrows.

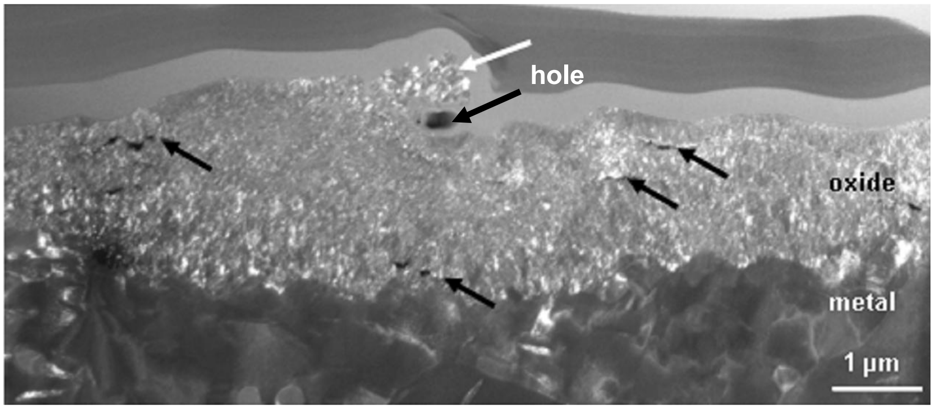

Figure 2-10. Dark field contrast of oxidized Zr1%Fe with iron oxide particles on the surface (white arrow). The black arrows represent large cracks in the oxide. (from reference [7]).

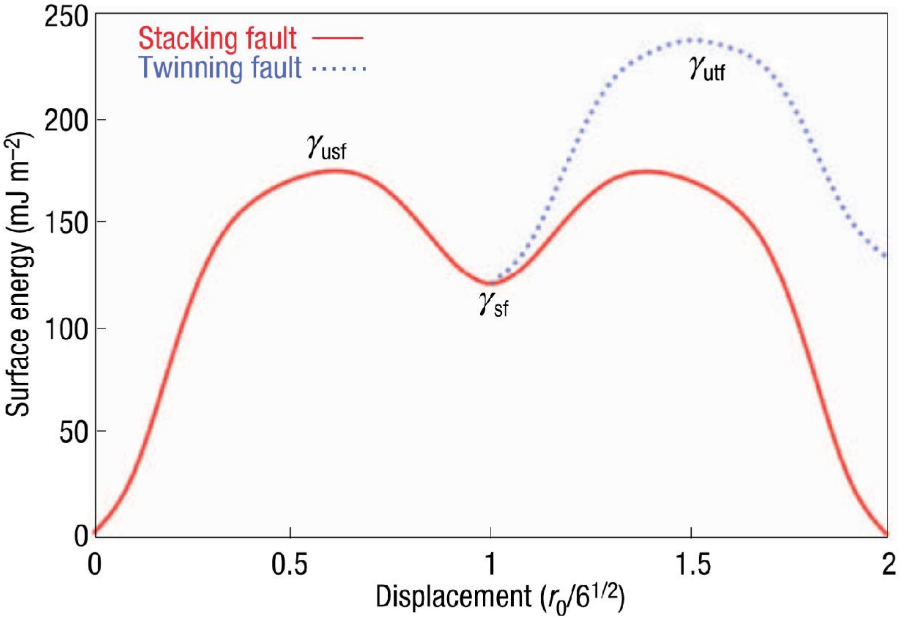

Figure 2-11. Generic generalized planar fault energy curves for the stacking and twin fault planar defect [24].

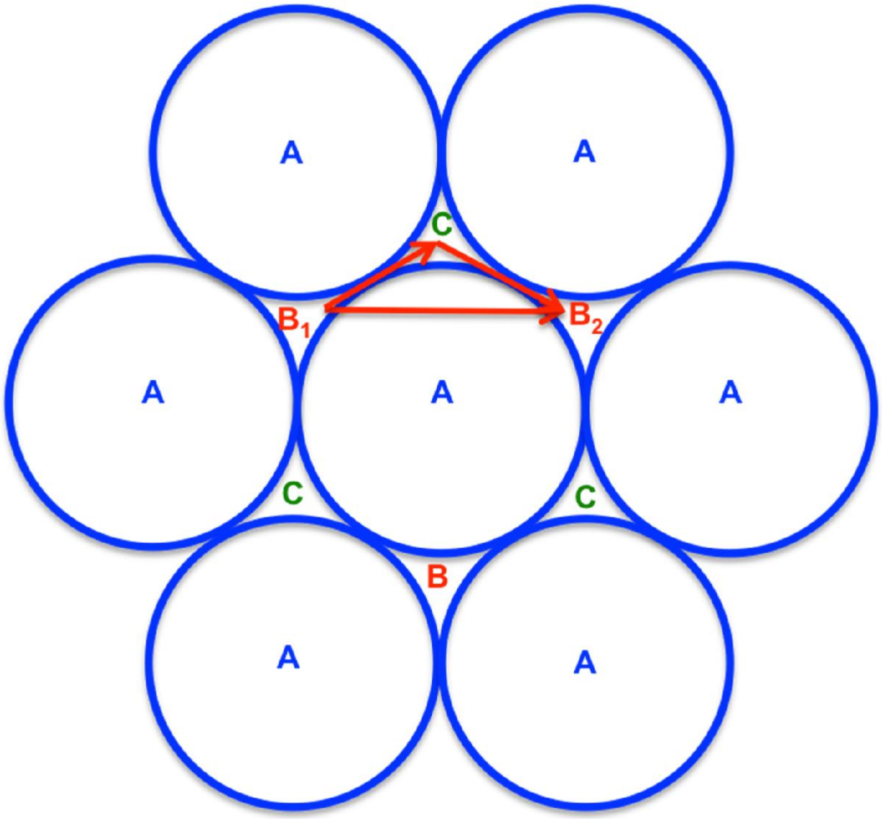

Figure 2-12. Possible directions of slip on close-packed (111) plane of FCC structure.

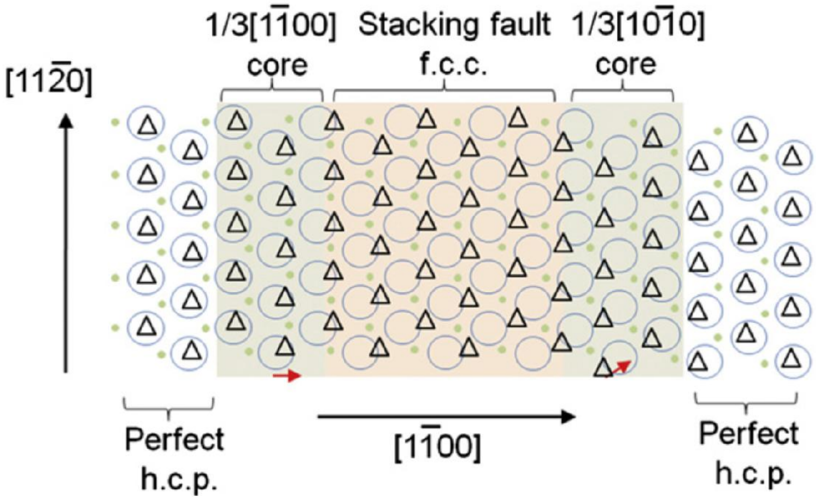

Figure 2-13. Schematic of an atomic structure of a <a> extended dislocation observed in Mg simulation [28]. Three atomic layers: A circle, B dot and C triangle. The red arrow indicates the slip vector of each partial dislocation.

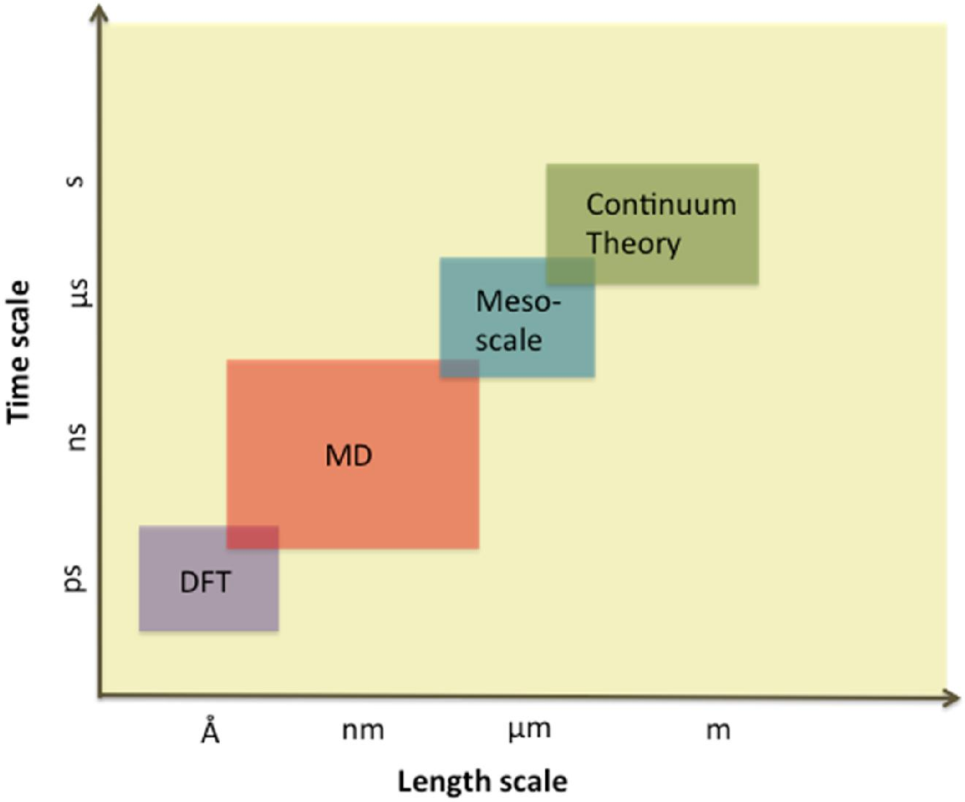

Figure 2-14. Simulation methods at different length and time scales.

CHAPTER 3
DEFORMATION PROCESSES IN POLYCRYSTALLINE ZR BY MOLECULAR DYNAMICS SIMULATIONS

Overview of MD Studies on Metal Systems

Molecular dynamics (MD) simulation has been widely used in the study of defects and microstructures in metals. MD simulations have provided significant insights into the mechanical behavior of fcc metals [20-24]. MD simulations of fcc copper showed material softening at very small grain sizes, i.e., a reverse Hall-Petch effect [20]. The simulation on nanocrystalline Al predicted twin deformation before it was identified in experiments [25, 26]. In the MD study of Al, Cu and Ni, the influences of the stacking fault energy, the unstable stacking fault energy and the unstable twin fault energy on the deformation behavior were analyzed. It was found that the stacking fault energy and, more importantly, the unstable stacking fault energy determine the dislocation behavior [24]. There has also been some work on hcp metals [27, 28]. The c/a ratio of Mg is 1.623 close to the ideal value; thus the primary slip system of Mg is on the basal plane. MD simulation of nanocrystalline Mg using an EAM potential [29] manifested the experimentally observed basal <a> dislocation and tensile twinning behaviors [28]. Nanocrystalline materials are of particular interest because they have a large area of grain boundaries, which tend to be dislocation nucleation sites. Moreover, nanocrystalline materials display some superior properties compared to coarse-grained materials, including improved strength and hardness, higher coefficient of thermal expansion and enhanced diffusivity [131]. MD simulation of nanocrystalline 2D $[0001]$-textured Zr using the Pasianot and Monti EAM potential [30] manifested the predominant

---

The work in this Chapter is based on Z. Z. Lu, M. J. Noordhoek, A. Chernatynskiy, S. B. Sinnott and S. R. Phillpot, *Journal of Nuclear Materials*, 2015, **462**, 147.

prismatic <a> dislocation and showed the Hall-Petch effect [31]. Bacon and Vitek found a strong relationship between the generalized stacking fault energy surface and dislocation behavior [35]. Because of the different slip systems of Mg and Zr (basal vs. prismatic), the deformation behavior of Zr is expected to be different from the deformation behavior of Mg. Thus, the focus here is the characterization of slip and twinning processes in nanocrystalline Zr by MD simulation, how stable and unstable stacking fault energies influence the deformation behaviors, and a comparison with polycrystalline Mg.

The embedded atom method (EAM) and modified embedded atom method (MEAM) potentials can effectively describe the mechanical properties of many metallic systems [132]. In this chapter, we perform deformation simulations of Zr with 2D $[11\bar{2}0]$- and $[0001]$-textured microstructures and the fully 3D microstructure with grains of random orientation. The reason for using two different 2D textured structures is to observe both prismatic slip ($[0001]$-texture) and basal slip ($[11\bar{2}0]$-texture). The prismatic slip and basal slip cannot both be observed in one single textured structure at the same time. Also $[0001]$ is the main texture observed in rolled Zircaloy discussed in the texture of zirconium alloy section of Chapter 2. The 3D nanocrystalline model can explore the competition among different deformation modes; there have been no previous simulations of fully 3D microstructures in Zr. The interatomic interactions are described by two different potentials: a Zr EAM potential, fitted by Mendelev and Ackland (MA) [103], and the Zr potential within the third generation Charge Optimized Many Body (COMB) framework [132]. The details of the formalisms of the two potentials are introduced in the interatomic potential section of Chapter 2. The fidelity of the two potentials in describing the mechanical response of Zr is compared.

Interatomic Potentials

Table 3-1 summarizes salient properties, and compares experimental values with those predicted by Density Functional Theory (DFT) using the Generalized Gradient Approximation (GGA), the MA potential and the COMB potential; although not used in this study, the EAM potential of Ackland et al. [133] (the Ackland potential) and Pasianot and Monti [30] are included in Table 3-1 for completeness.

In order to be able to correctly model the mechanical behavior using MD, the structure, elastic properties and stacking fault energy should all be correctly described by the potentials. The Ackland potential [133] is capable of describing the lattice constants and elastic constants. However, it underestimates the basal stacking fault energy by a large amount (almost a factor of four). The lattice constants and elastic constants of both the MA [103] and COMB [132] potentials closely match the experimental [134, 135] and DFT [136] values. DFT predicts the basal stacking fault energy to be 30 mJ/m^2 higher than the prismatic stacking fault energy. The MA and COMB potentials both predict the correct order, but straddle the DFT predictions and both predict somewhat larger energy differences than DFT. These predictions of the correct order of the basal stacking fault energy and prismatic stacking fault energy are important as stacking fault energies have a strong influence on the mechanical properties.

Based on this assessment of the basic properties, the MA and COMB potentials should describe the mechanical properties with similar levels of materials fidelity. The EAM formalism of the MA and Ackland potentials is simpler than the COMB formalism and computationally much faster. However, the COMB formalism can also include Zr–

ZrO_2–ZrH_2 system, which is presented in reference [71]; ZrO_2 and ZrO_2/Zr systems will be studied in Chapter 5 and Chapter 6.

Stacking Fault Energetics

As discussed in the previous section, in order to use an empirical potential to study the dislocation processes in Zr, it is important that the potential reproduce not only the correct stacking fault energy, but also the generalized stacking fault energy, which is critically involved in slip. As discussed in detail in [132], the generalized stacking fault energy is calculated using the method described by Poty et al. [137]. As summarized in Figure 3-1, DFT and the MA and COMB potentials all predict the same minimum energy path for basal slip. Because the indirect path has a lower energy than the direct path between the minima, the basal <a> dislocation dissociates into two Shockley partials: $\frac{1}{3}\langle 11\bar{2}0\rangle = \frac{1}{3}\langle 10\bar{1}0\rangle + \frac{1}{3}\langle 01\bar{1}0\rangle$.

By contrast, on the prismatic plane the COMB potential predicts the same path as DFT as indicated in Figure 3-2B and Figure 3-2C, with the energy minimum lying along the $\langle 11\bar{2}0\rangle$ direction. There is a local minimum along the <a> direction predicted by DFT and the COMB potential (the ‘direct’ <a> path), as shown in Figure 3-2D. In contrast, as illustrated in Figure 3-2A, the minimum point for the MA potential does not correspond to a $\langle 11\bar{2}0\rangle$ trajectory, but is shifted along the <c> direction (the ‘indirect’ <a> path). The prismatic $\langle 11\bar{2}0\rangle$ dislocation can dissociate into $\frac{1}{4}\langle 22\bar{4}1\rangle + \frac{1}{4}\langle 22\bar{4}\bar{1}\rangle$. Figure 3-2A further shows that in the case of the MA potential, there is only a single energy barrier of 277mJ/m^2 along the direct <a> path. However, due to the local energy minimum position shifting along the <c> direction, there is a local minimum along the indirect $\frac{1}{4}\langle 22\bar{4}1\rangle + \frac{1}{4}\langle 22\bar{4}\bar{1}\rangle$ path. Moreover, the energy barrier, 271 mJ/m^2, on the indirect path is slightly lower than that on the direct path. This may lead to the formation of a partial <a> dislocation: $\langle 11\bar{2}0\rangle = \frac{1}{4}\langle 22\bar{4}1\rangle + \frac{1}{4}\langle 22\bar{4}\bar{1}\rangle$ instead of a full <a> dislocation on the prismatic plane for the MA potential. The influence of the above difference between MA and COMB potentials will become clear in the simulations of the mechanical response described below.

In order to correctly describe the dominant prismatic slip in Zr, an empirical potential should yield a higher barrier on the basal plane than on the prismatic plane. The energy barriers along the indirect <a> path (unstable stacking fault energy) on the basal plane obtained by DFT [137], MA and COMB are 250 mJ/m^2 [137], 314 mJ/m^2 and 346 mJ/m^2. Similarly, the energy barriers along the <a> direction on the prismatic plane obtained by DFT [137], MA and COMB are 199 mJ/m^2 [137], 277 mJ/m^2 and 246 mJ/m^2. That is, in all three cases the energy barrier for prismatic <a> is smaller than the energy barrier for basal <a>. Thus both empirical potentials predict the prismatic <a> dislocation to be the predominant dislocation mode, which is in consistent with the experiment results [36].

Overall, the MA potential tends to underestimate the stacking fault energy comparing to the DFT results, while the COMB potential tends to overestimate the stacking fault energy. This energy difference can be expected to results in a high yield strength for the COMB potential. It can also be expected that there will be some differences in prismatic slip as described by the MA and COMB potentials.

Simulation of Deformation of Textured Zr

Deformation simulations using a textured polycrystalline structure have previously been performed on Al [138] and Mg [28]. Deformation simulations using fully 3D polycrystalline structures have been carried out on Cu, Ni and Al using various empirical potentials that have different stable and unstable stacking fault energies [24]. The effect of unstable and stable stacking fault energies on dislocation behaviors has been discussed [24]. A textured polycrystalline structure has the advantage that, compared to fully 3D random microstructures, the simulation of 2D textured microstructures is less computational intensive; moreover, it is easier to visualize the deformation process. However, the textured microstructure does limit the deformation processes that can be manifested. Also due to the small thickness of the textured structure, the activated dislocations from GBs can only be straight lines [23]. The results of simulations with the MA and COMB potential will be compared with each other and with experiment. The effect of the different unstable and stable stacking fault energies of MA and COMB potential on dislocation behaviors will be discussed. The simulation results will also be compared with simulations on the same microstructure in Mg carried out by Kim et al. [28]. The slip and twinning systems in Zr as seen in experiments are presented in Table 3-2.

The tensile test simulation of textured polycrystalline structure Mg manifests the experimentally observed deformation behaviors [28]. The 2D structure [28] shown in Figure 3-3 has four grains; this is crystallographically identical to the Mg structure simulated by Kim et al. [28]. Due to the highly textured structure, when the loading direction is applied along the x- or y-directions, only certain types of deformation behaviors can be activated. Hence, in order to see all the important deformation behaviors, different textured structures need to be used. The $[11\bar{2}0]$ textured structure is favorable for basal slip, pyramidal slip and twinning. For the Mg case, the primary slip system is basal <a> slip. Thus the $[11\bar{2}0]$ texture can support both the basal slip and twinning behavior of

Mg. The $[11\bar{2}0]$ textured is a good choice to simulate the pyramidal and twinning behavior of Zr system. However the primary slip for Zr is prismatic <a> slip, which requires the $[0001]$ texture. Thus, we simulate deformation in a $[0001]$ textured system for the Zr case as well. For the 2D textured structure, periodic boundary conditions are applied in all three spatial directions.

Deformation in $[\mathbf{11\bar{2}0}]$ Textured Polycrystal

We first simulate the $[11\bar{2}0]$ texture to examine twinning and pyramidal slip. The 2D structure, shown in Figure 3-3, contains four grains with orientations of 11.25°, 33.75°, 56.25°, and 78.75° with respect to the simulation cell edges. The structure is successively annealed at high (900K), low (200K) and room temperatures (300K) [28], after which the total stress value of the system was below 0.01 GPa. Common neighbor analysis (CNA) is used to distinguish fcc like atoms from hcp atoms [126, 127]. The structure is visualized with AtomEye [122].

Creep Simulations in Zr

Creep simulations are performed with a uniaxial load along the x-direction in Figure 3-3, with the load ranging from 1 GPa to 4 GPa. The creep curves are shown in Figure 3-4, from which we can see that the two potentials have similar responses to the uniaxial loading. For 1 GPa and 2 GPa loads, there is no dislocation activity in either the COMB or MA simulations; in both cases, the stress is not large enough for dislocations to initiate and the response of these systems is purely elastic. In both cases, the polycrystals display plasticity at 3 GPa; thus for both potentials, the yield stress is between 2 and 3 GPa. There are more extended dislocations under 4 GPa load than under 3 GPa load. The MA potential deforms at a higher strain rate than the COMB potential at 3 GPa, just above the yield stress; this is consistent of the lower stacking fault energy level of MA potential, as discussed in the previous section. At 4 GPa, well above the yield stress, the strain rates are similar.

Figure 3-5 shows snapshots of systems with 30 nm grain size strained by 6.3% under a stress of 4 GPa. For both potentials we can see pyramidal <c+a> partial dislocations, partial <a> dislocations and extended dislocations; the structures are similar for the two potentials.

The large areas of GBs in the textured polycrystalline structure readily act as nucleation sites for dislocations and twinning. As shown in Figure 3-5 and Figure 3-7A, pyramidal slip nucleates from the grain boundaries with Burgers vector of 1/6$[2\bar{2}03]$. The pyramidal <a+c> dislocation is observed in Ti-6Al-4V and it can dissociate into 1/6$[2\bar{2}03]$ [139]. The dissociation of pyramidal <a+c> dislocation into 1/6$[2\bar{2}03]$ partials is also observed in Mg by electron microscopy [140]. The same dissociation is also observed in the Mg MD simulation [28]. For the COMB potential, the approximate number of pyramidal dislocations generated in grains 1 - 4 is 0, 8, 0 and 19 as compared to 1, 11, 6 and 22 for the MA potential. The strong differences among the various grains can be understood in terms of the resolved shear stress in each grain. For grain 1 there is no pyramidal slip for either potential due to the very small Schmid factor (0.03) for pyramidal slip. With relatively large Schmid factors for grain 2 (0.50) and grain 4 (0.37), both potentials yield pyramidal slip. However, for grain 3 with Schmid factor of 0.33, there are 10 pyramidal slips for MA, while there is no pyramidal slip for COMB. The explanation for this difference may lie in the grain boundary structures. From Figure 6(a) and Figure 6(b), it can be seen that the structure of the grain boundary is only subtly different for the two potentials before the load is applied. Nevertheless the resulting evolutions during deformation, Figure 6(c) and Figure 6(d), during deformation are quite different. Evidence that details of the GB structure can be significant was found in a simulation of deformation of fcc Ni, in which an inverse relationship between the static GB energy and the energy barrier to slip nucleation at the GB was identified [25]. We thus speculate that the atomic-level rearrangement of the grain boundary between grain 2 and grain 3 in the COMB simulation during deformation may decrease the grain boundary energy and thus increase the GB dislocation nucleation energy barrier, suppressing the emission of pyramidal dislocations.

Extended dislocations, as illustrated in Figure 3-7, are observed in both MA and COMB. The partial dislocation core nucleates from the grain boundary and moves into the grain with a Burgers vector of 2/3$[1\bar{1}00]$, leaving behind an I2-type stacking fault. The stacking fault connects the partial core and the grain boundary. When the stress is high enough, the second partial core nucleates from the grain boundary and starts to move into the grain, thereby forming a structure of two partial cores connected by a stacking fault; this is an extended dislocation [26]. The observed extended dislocation atomic structure is shown in Figure 3-8. The extended dislocation contains two 1/3$[1\bar{1}00]$ partial cores connecting by an I2 type stacking fault. The formation of extended dislocations has been widely observed during deformation simulations of fcc [24, 138] and hcp [28] metals. Moreover, the presence of extended dislocations here is consistent with the basal stacking fault energies of 199mJ/m^2 of MA and 267mJ/m^2 of COMB. However, such extended dislocations are mostly observed in grain 4, which has the highest dislocation density and displays twinning behavior. This observation is consistent with the Al case, in which it was observed that extended dislocations can exist under high internal or external stress [138]. Based on the Schmid factor, extended dislocations are more likely in grain 1 and grain 4. Our simulation results show that the splitting distance of the extended dislocation is very long in grain 1 and the density of the extended dislocations in grain 4 is the highest. According to dislocation theory [141], the distance between partials, that is the length of the stacking fault, is determined by the applied stress and the stacking fault energy. Thus, under the same stress condition, a higher stacking fault energy leads to a shorter splitting distance. There are a large number of extended dislocations and the splitting distance is much longer for the MA potential than for the COMB potential. This difference can be explained from Figure 3-1 and Table 3-1: the energy barrier for basal partial <a> dislocation is lower for the MA potential than for the COMB potential.

At 6.3% strain for MA potential, the basal <a> slip nucleates from the grain boundary in grain 2 as shown in Figure 3-9. The structure of this basal slip is different from the one shown in Figure 3-7B in that there are no atoms in fcc environments. By contrast, there is no basal <a> slip for the COMB potential simulations. The appearance of the basal <a> slip for MA potential is physically reasonable because it has a lower energy barrier along the basal <a> path than the COMB potential.

Twinning processes are also observed in grain 4 for both potentials, as shown in Figure 3-5. The tensile twin is nucleated at a GB, which is a favorable site for twin nucleation [142, 143]. However, in both cases, the twinned regions remain small. The detailed structures of the $\{10\bar{1}2\}\langle10\bar{1}1\rangle$ tensile twin are shown in Figure 3-10. The twinning region has a high density of I2-type stacking faults. As discussed above, extended dislocations are only observed under high constant stress load. The twin region can act as a high stress concentration area to promote the formation of stacking faults. From Figure 3-10, the structure of the twin boundaries is very similar for the MA and COMB simulations, consisting of two dislocations on the pyramidal and basal planes; the results of dislocation dissociation are represented by the black lines in Figure 3-10. This twinning nucleation mechanism is consistent with the dislocation dissociation mechanism described in reference [144]. Another twinning boundary seen in the MA simulation consists of two dislocations on pyramidal planes as shown in Figure 3-9A. This type of twin boundary structure may make it difficult for the twin boundary to move.

Overall, for the $[11\bar{2}0]$ texture simulation, the MA and COMB potentials yield very similar deformation behaviors. In particular, they predict the same dislocation and twinning behaviors. Moreover, the atomic structures of all the defects are very similar. Given that the functional forms of the interatomic interactions in these two potentials are very different from each other, this similarity gives us high confidence that they are both capturing deformation behavior that is representative of what would be seen experimentally.

Comparison to Mg for $[\mathbf{11\bar{2}0}]$ Texture

It is instructive to compare the above results for Zr with earlier simulations on polycrystalline Mg with the same microstructure. As an illustration, in Figure 3-11 we present the $[11\bar{2}0]$ textured structure of Mg [28] where a tensile twin, basal <a> dislocations, extended dislocations and pyramidal <c+a> partial dislocations can be observed. The same features are found in the $[11\bar{2}0]$ textured Zr explored in this work as shown in Figure 3-5. Thus, from the point of view of the types of deformation modes, the Mg case and Zr case are very similar. However, in terms of the amount of activity associated with each deformation mode, the Mg case and Zr case have some differences. For the Zr case, the twinning region does not occupy as large a portion of the grain as in the Mg case [28]. Unlike the twin boundary in the Zr case that only consists of two dislocations on two planes, the twin boundary in the Mg case has more curvature. Also the density of the stacking faults inside the twinning region is much high for Mg as compared with Zr.

The stacking fault forms after the emission of the first partial dislocation core; this dislocation core is also part of the twin boundary. It thus appears that the movement of partial dislocation cores followed by the stacking fault may help the growth of the twinning region. The stacking faults energies of the Mg EAM [29] potential, 27 mJ/m^2 (I1 stacking fault) and 54 mJ/m^2 (I2 stacking fault) are very low in comparison to Zr. Thus, purely from point of view of energy, it is much easier for Mg to form a structure that consists of a leading partial dislocation core and a stacking fault. Hence the growth of the twinned region is very likely related to the stacking fault energy.

The commonly observed pyramidal slip, extended dislocations and twinning in hcp systems have been manifested in both the Mg and Zr simulations. Moreover, the same detailed atomic structures are seen for pyramidal and extended dislocations of Mg and Zr. In addition to the basic potential properties, the stacking fault energy has a big influence on the mechanical properties. Thus tuning the stacking fault energy is a key factor during the potential fitting process in order to correctly describe the mechanical properties.

Deformation in $[0001]$ Textured Polycrystals

Due to the highly textured structure, only pyramidal slips and extended dislocations on the basal plane can be activated in the $[11\bar{2}0]$ texture. Because of this limitation of the $[11\bar{2}0]$ texture, the simulations described above do not probe the prismatic <a> dislocation, which is the dominant slip mode in Zr. In order to characterize deformation via this dislocation, we also simulate structures with the $[0001]$ textured structure, which promotes prismatic slip. The symmetry of basal plane is six-fold; we thus select the orientations of the four grains in our textured polycrystal as 0°, 15°, 30° and 45° with respect to the x-axis of the simulation cell. Thus, there are a number of 15° GBs in the structure; these are relatively low misorientation angles and these GBs can be expected to be less stable than the higher angle GBs in the $[11\bar{2}0]$ textured structure. The equilibration process is the same as for the $[11\bar{2}0]$ texture. The tensile test is carried out 300 K with a constant stress value of 3 GPa; this smaller constant stress value comparing to $[11\bar{2}0]$ is used because of the presence of the low angle GBs.

For the $[0001]$ texture, the two potentials again yield rather similar results; the 7.3% strained structures are shown below in Figure 3-12. The microstructure evolution of COMB is shown in Figure 3-13. The predominant prismatic <a> slip is the only slip mode observed in the simulation, as we expect; twinning is not expected because the applied stress favors of the predominant prismatic <a> slip rather than the twinning behavior. The first partial dislocation nucleates from the grain boundary; when given enough energy, the second partial dislocation can nucleate from grain boundary and a full prismatic <a> slip is formed in the grain. From the microstructure evolution shown in

Figure 3-12, we can see that some of the prismatic dislocations are full dislocations. This is consistent with prior MD simulation results using $[0001]$ texture structure under constant strain rate [35]. This is in contrast to the $[11\bar{2}0]$ texture, in which it is difficult for the second partial pyramidal slip to nucleate. From the stable and unstable stacking fault energy point of view discussed above, it requires less energy for the second partial prismatic dislocation to nucleate for the $[0001]$ texture, again illustrating the close relationship between stacking fault energy and dislocation behavior. Within each grain, most of the prismatic slips glide in <a> direction on the same plane, because only one of three prismatic planes is favorable for prismatic <a> dislocation due to the Schimid factor.

Simulation of 3D Nanocrystalline Microstructures

While the $[11\bar{2}0]$ texture promotes pyramidal slip, basal slip and twinning, the $[0001]$ texture promotes prismatic slip. To explore the competition among these modes, we now simulate a 3D randomly oriented polycrystalline structure in which all slip and twinning processes are potentially active.

The 3D polycrystalline structure consists of 16 randomly oriented grains with an average grain size of 18 nm. The equilibration process of the 3D structure is the same as that for the 2D structure discussed above. The tensile test is conducted at 300K with a constant stress value of 3 GPa. Comparing to the 2D texture structure, a smaller stress has been applied to the 3D structure because the 16 randomly oriented grains in the structure can provide more dislocation nucleation sites and can cooperate to promote the predominant slip. The initial structure is shown in Figure 3-14. In this figure, the structure is cut in order to show the hexagonal shape of the grains. Periodic boundary conditions are applied in x, y and z directions. The stress is applied along y direction. Figure 3-15 and Figure 3-16 show the CNA map of 3D nanocrystalline Zr for both MA and COMB potentials after loading.

Because of the large grain boundary area for potential nucleation sites and the 16 different orientations of the grains, the predominant prismatic <a> slip is most prevalent in both the MA and COMB potential simulations, as shown in Figure 3-15 and Figure 3-16. This prismatic <a> slip is the experimentally realized deformation mode in Zr and is consistent with the order of prismatic and basal stacking fault energies of the potentials themselves. The dislocation density for the MA potential is higher than that for COMB, which is consistent with the results of the textured structure simulation. The details of the prismatic dislocation are shown in Figure 3-17. The prismatic <a> dislocation displays both full dislocation and partial dislocation structures. The COMB potential yields more full prismatic dislocations than does the MA potential; from the prismatic stacking fault energy map, Figure 3-2B, we recall that the minimum path of prismatic <a> for the COMB potential is along the <a> direction. By contrast, for the MA potential, the minimum point on the <a> path is shifted along the <c> direction, see Figure 3-2A. This shift causes the prismatic <a> slip of the MA potential to break into partial dislocations. However, the above difference was not present for the $[0001]$ texture simulations due to the short gliding distance of prismatic <a> dislocations and the thinness of the textured structure that forces the dislocations to be straight lines. There are a few basal extended dislocations for the MA potential but virtually none for the COMB potential. This is also consistent with the stacking fault energy map on the basal plane. As shown in Figure 3-1(d), the energy barrier for the basal <a> partial dislocation of MA potential is lower than that of COMB potential. Twinning behavior is almost absent for both MA and COMB in the 3D simulation. The small 3D 16 randomly oriented grains structure has a large fraction of atoms at or close to GBs; these GBs provide the ideal nucleation sites for dislocations. Thus, compared to the textured structure, the sixteen randomly oriented grains structure have a much higher proportion of dislocation activation as compared to twinning activity.

Conclusions on MD Simulations of Polycrystalline Zr

The objective of this work was to describe deformation in fine-grained polycrystalline Zr, to compare results from two rather different interatomic descriptions of the atomic interactions, and to compare with the results of previous simulations on Mg. The ability of the MA and COMB potentials to describe the deformation process of Zr has been shown. From work on fcc metals, we know that not only the stacking fault energy but more importantly the unstable stacking fault energy plays an important role in the mechanical response of a metal [24]. Thus, for a potential to predict the dominant dislocation mode, it needs to correctly predict the lowest unstable stacking fault compared to other slip modes. For the MA and COMB potentials, the energy barrier for prismatic dislocation is lower than the barrier for basal dislocation. Thus, we observe the prismatic <a> dislocation to be the dominant dislocation mode in our simulations. The ability of the potential to predict full dislocations or partial dislocations is determined by two factors. The first factor is the lowest energy path on the slip plane. On the basal plane, the lowest energy path is $\frac{1}{3}\langle 10\bar{1}0\rangle + \frac{1}{3}\langle 01\bar{1}0\rangle$ for both MA and COMB potential. Consistent with this, a basal partial dislocation was observed in the simulation instead of full basal <a> dislocation. The second factor is the ratio between the energy of the stacking fault and unstable stacking along dislocation path. If the ratio is close to unity, the potential tends to predict full dislocations, while if the ratio is much less than unity, the potential tends to predict partial dislocations [24]. On the basal plane, this ratio is 0.63 for MA and 0.77 for COMB. Thus, both potentials tend to predict partial dislocations. We observe basal partial dislocations in our simulation with a higher density for in the MA simulation, consistent with its smaller ratio compared to COMB. On the prismatic plane along the direct <a> path, the ratio of the stacking fault and unstable stacking fault energies [24, 137] is 1.0 for the MA potential and 0.9 for the COMB potential. Thus, the two potentials should predict full dislocations on the prismatic plane. However, the MA potential has a slightly lower energy indirect path on prismatic plane. In the 3D simulation, we observe more full dislocations on prismatic plane for COMB than for the MA potential.

The deformation behavior is also determined by the Schmid factor, grain boundary structures, misorientation angles between grains and competition between different slip modes and twinning. The extended dislocation and twinning behaviors have been observed in the high dislocation density grain with high stress level. The nucleation of the second partial and twinning requires higher energy. In order to get the reasonable results from the mechanical simulation, the potential needs to yield the correct general stacking fault on major slip planes of the simulating system.

Table 3-1. Properties of Zr given by the COMB potentials compared with experiment, DFT calculations, and EAM potentials.

Properties	Experiment 134, 135	DFT 136	Ackland 133, 137	Pasianot and Monti 30	MA 103, 137	COMB 132
a (Å)	3.23	3.23	3.267	3.232	3.234	3.226
c (Å)	5.15	5.17	5.211	5.149	5.168	5.159
c/a	1.594	1.600	1.595	1.593	1.598	1.599
E_c (eV/atom)	-6.32	N/A	-6.245	-6.25	-6.635	-6.32
C_{11} (GPa)	155	156	157	143	147	154
C_{12} (GPa)	67	61	75	73	69	71
C_{13} (GPa)	65	62	69	65	74	62
C_{33} (GPa)	172	166	174	165	168	164
C_{44} (GPa)	36	26		32	44	32
Basal I_2 stacking fault (mJ/m^2)		227	55	70	199	267
Prism I_1 stacking fault (mJ/m^2)		197		162	145	215
Basal surface (mJ/m^2)		1600			1770	1770
Prism surface (mJ/m^2)		1660			1930	1740

Table 3-2. Slip and twinning systems of Mg and Zr [33, 35].

Properties	Mg	Zr
Slip system	Predominant basal <a> Secondary prismatic <a>, pyramidal <c+a>	Predominant prismatic <a> Secondary basal <a>, pyramidal <c+a>
Twin system	Tensile twin $\{1\bar{1}02\}$ Compressive twin $\{10\bar{1}1\}$	Tensile twin $\{1\bar{1}02\}$ $\{11\bar{2}1\}$ Compressive twin $\{11\bar{2}2\}$

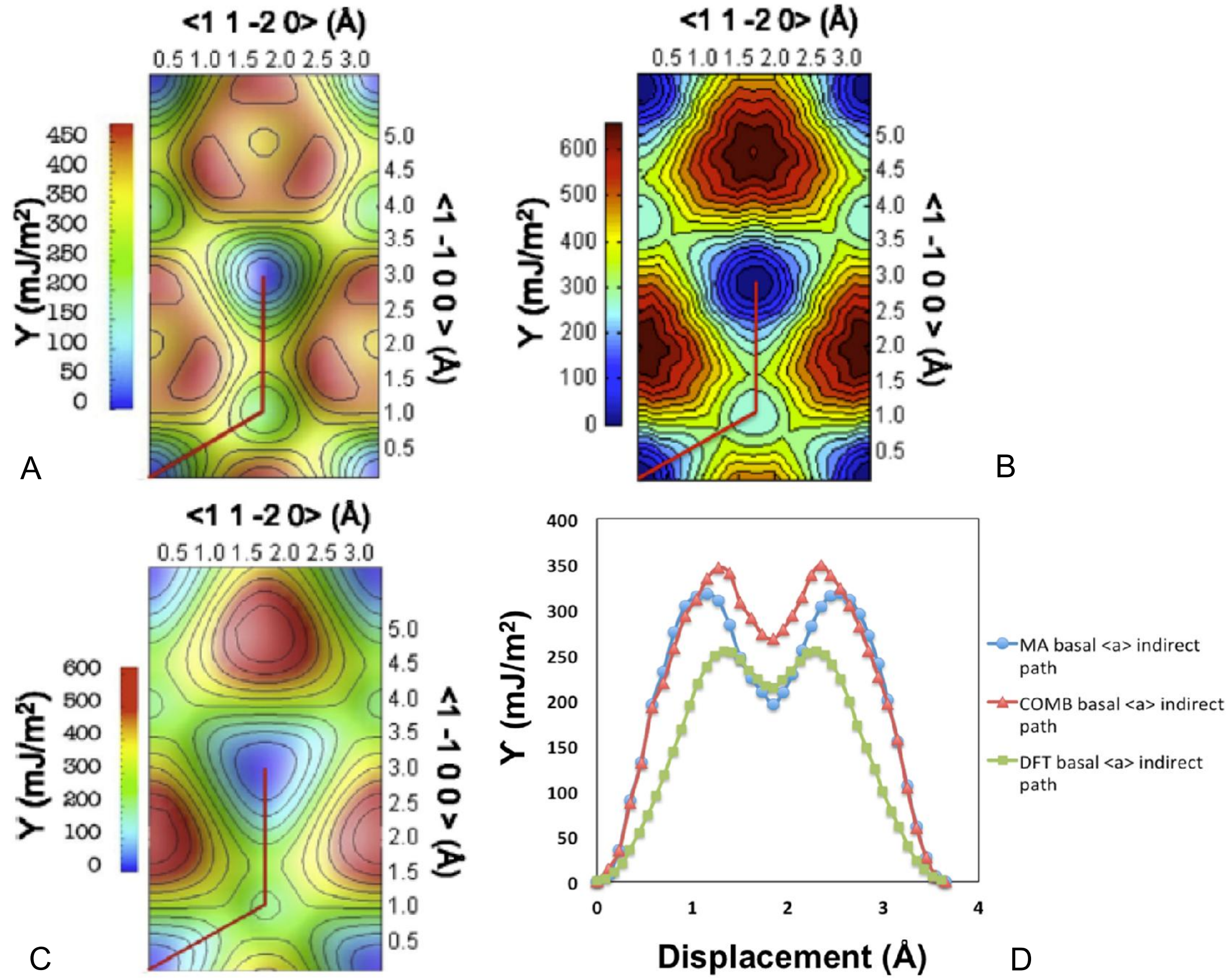

Figure 3-1. Stacking fault energy map of $[0001]$ basal plane. A) MA [137]. B) COMB. C) DFT [137], reproduced from Ref [137] with permission. D) Stacking fault energy along the minimum energy indirect path for MA, COMB and DFT.

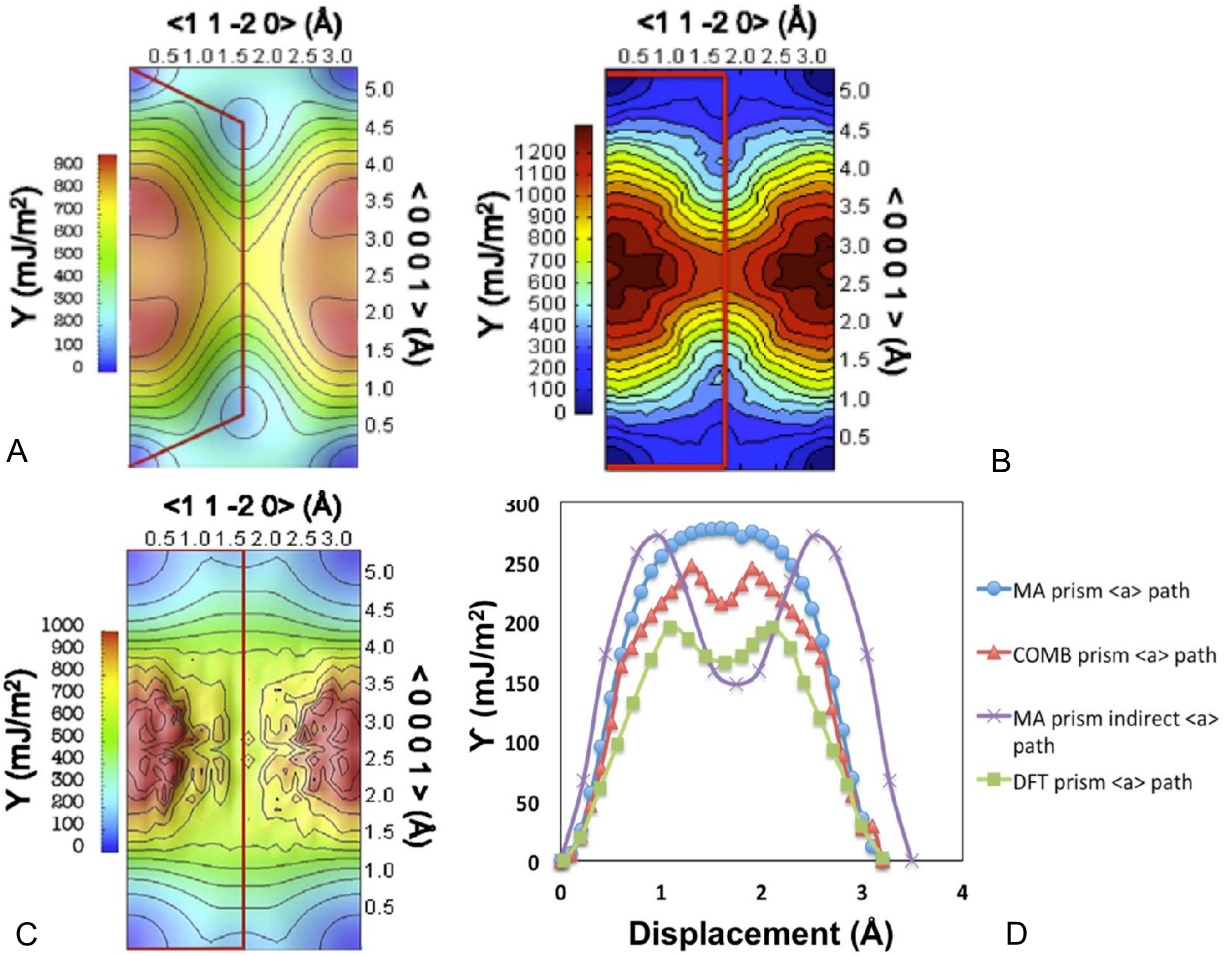

Figure 3-2. Stacking fault energy map of $[10\bar{1}0]$ prismatic plane. A) MA [137]. B) COMB. C) DFT, reproduced from Ref [137] with permission. D) Stacking fault energy along direct <a> path for MA, COMB and DFT; the energy for the indirect <a> path for the MA potential, illustrated in A is also shown.

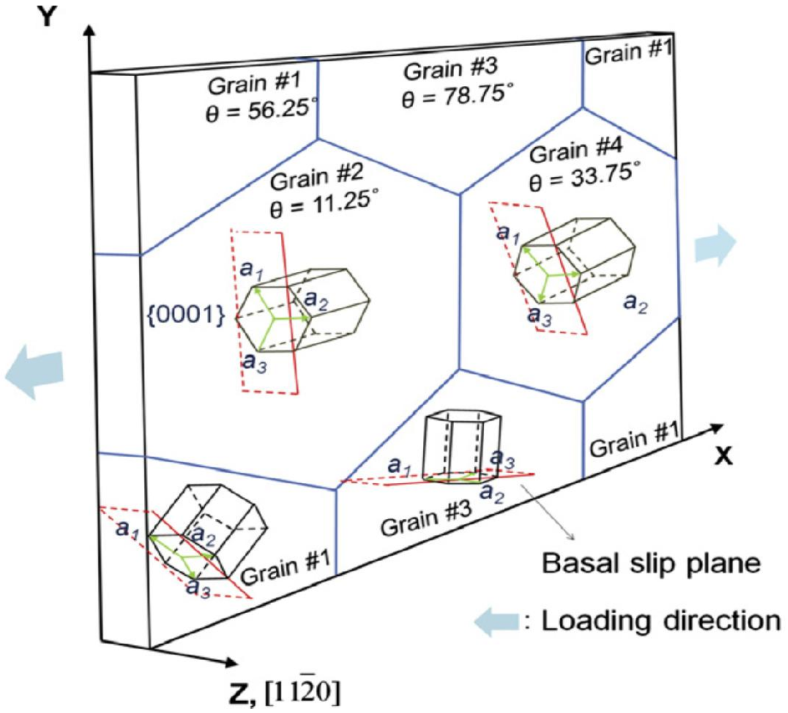

Figure 3-3. The 2D $[11\bar{2}0]$-textured simulation structure is the same as that used for prior simulations of Mg. Reproduced from Ref [28] with permission.

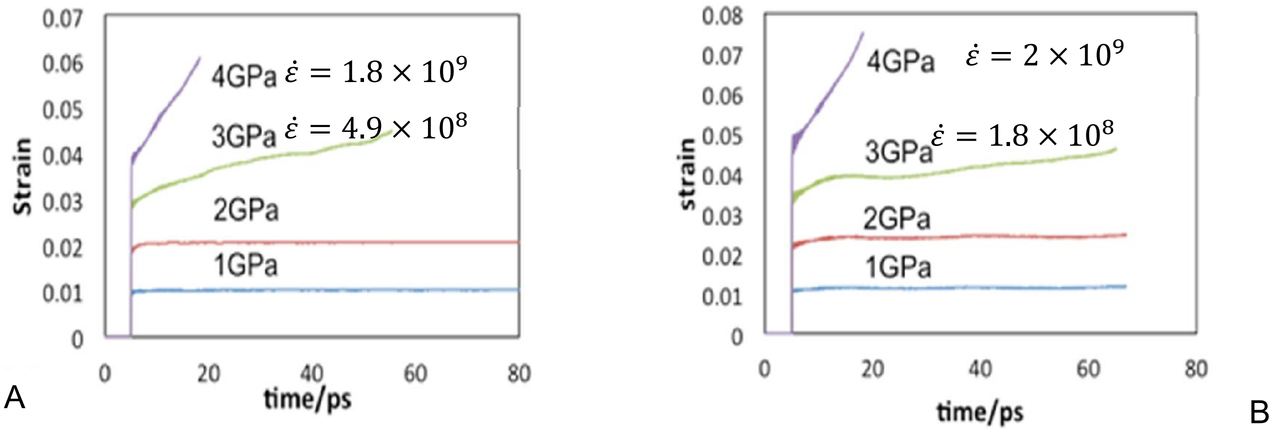

Figure 3-4. Creep plots for the $[11\bar{2}0]$ textured structure in Figure 3-5. A) MA potential. B) COMB potential.

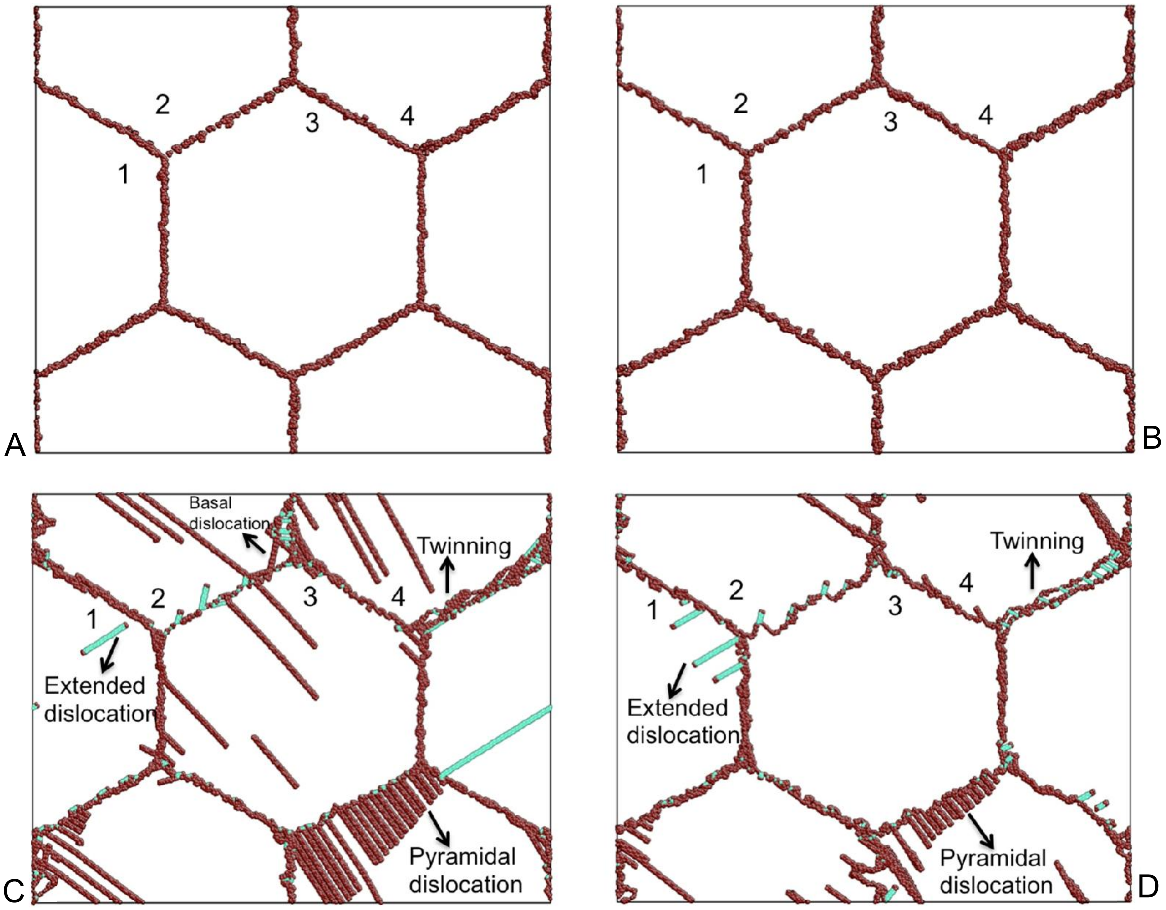

Figure 3-5. $[11\bar{2}0]$-textured structure with a grain size of 30 nm before tensile loading and under 6.3% tensile strain at 4 GPa. A) MA. B) COMB. C) MA 6.3% strain. D) COMB 6.2% strain. In this and subsequent similar figures, atoms are distinguished by CNA with the red atoms representing atoms with coordination different from 12, the disordered atoms. The light green atoms represent fcc environment atoms. Atoms in hcp environments are not shown.

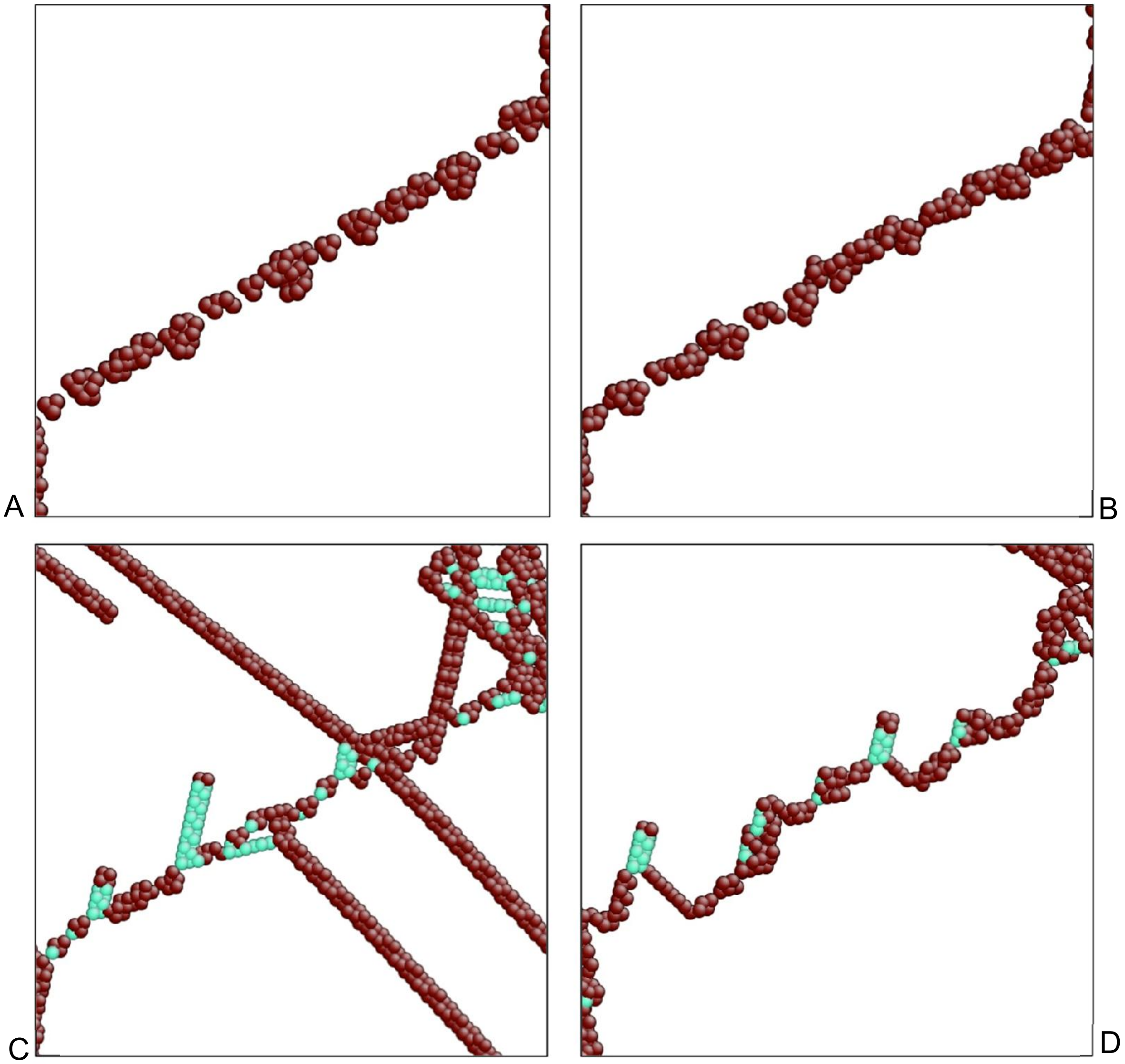

Figure 3-6. Grain boundary between grain 2 and grain 3 before and after loading. A) MA before loading. B) COMB before loading. C) MA 6.3% strain. D) COMB 6.3% strain.

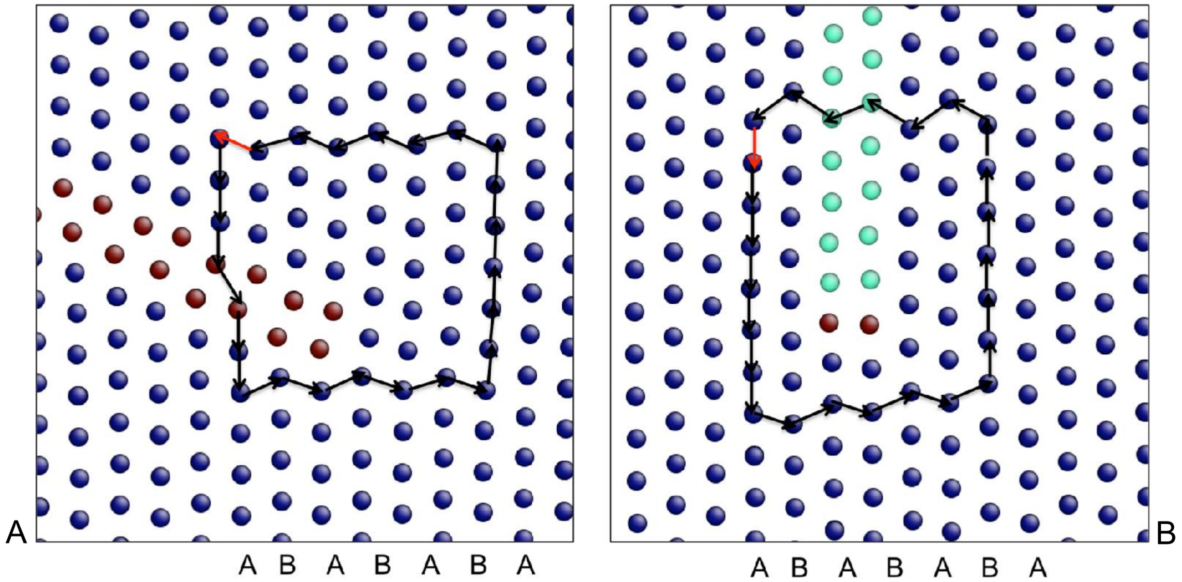

Figure 3-7. Atomic structures of pyramidal and basal partial dislocations. A) Pyramidal 1/6[$2\bar{2}03$]<c+a> partial dislocation. B) I2-type stacking fault with a partial dislocation of 2/3[$1\bar{1}00$]. The results are from COMB simulation. MA simulations yield the same atomic structure, not shown. Blue atoms denote those in hcp environments.

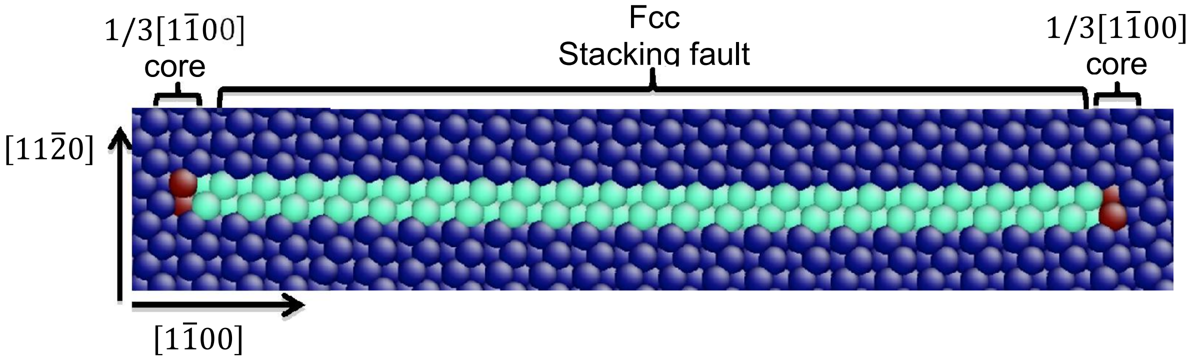

Figure 3-8. Atomic structure of the extended <a> dislocation from a simulation with COMB potential; the structure of the dislocation with the MA potential is the same.

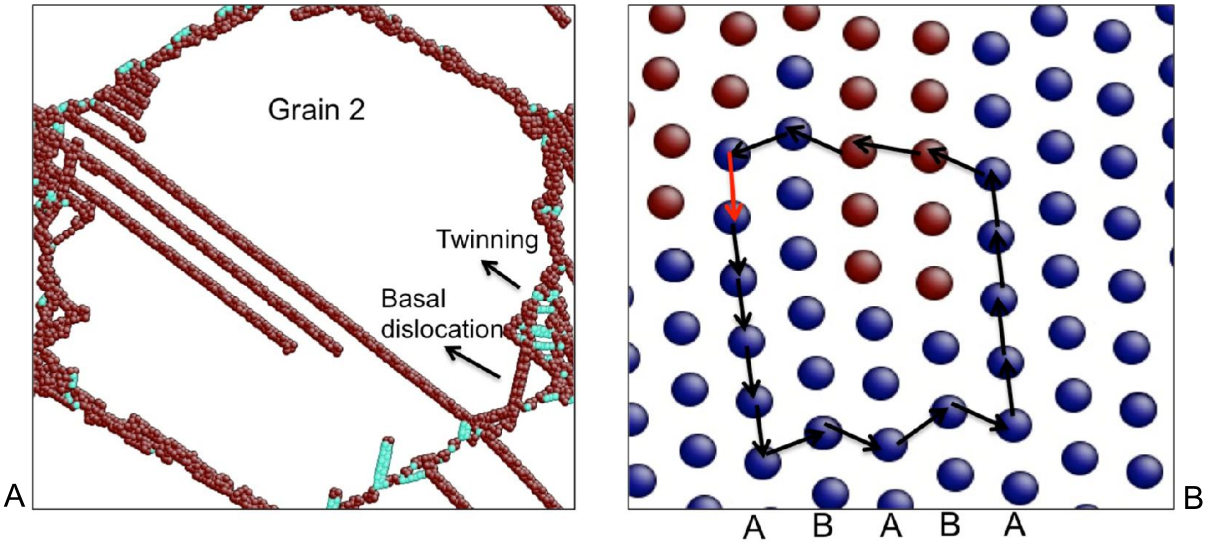

Figure 3-9. Basal dislocation in MA potential. A) In a 6.3% strained grain, basal slip take place for the MA potential; atoms in hcp environments not show. B) Details of 2/3$[1\bar{1}00]$ basal <a> dislocation; the red arrow indicates the Burgers vector.

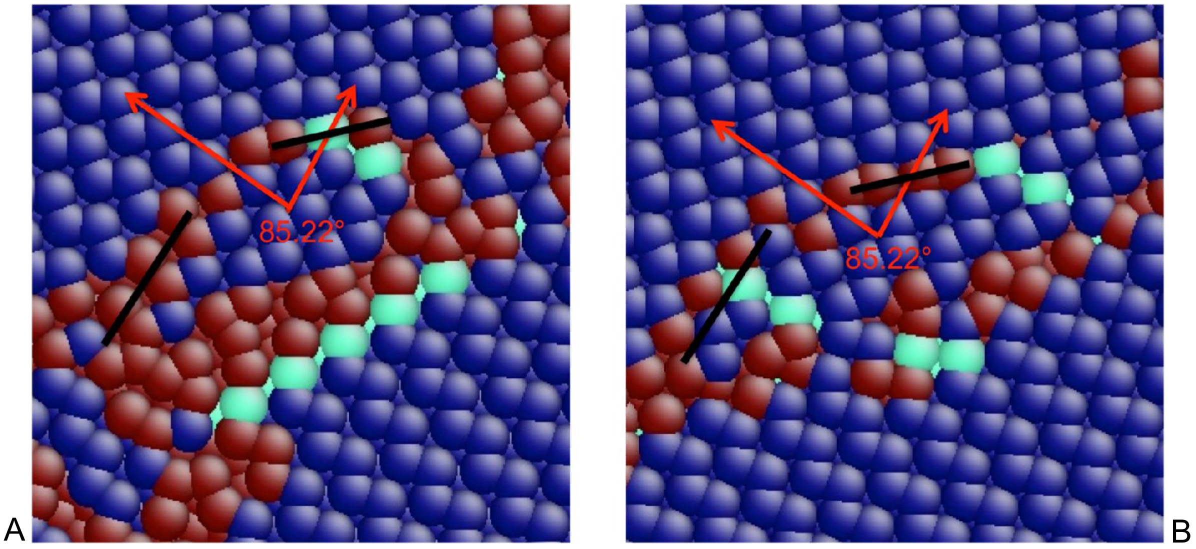

Figure 3-10. $\{10\bar{1}2\}\langle 10\bar{1}1\rangle$ twin found during tensile test of the 2D textured system. A) MA. B) COMB.

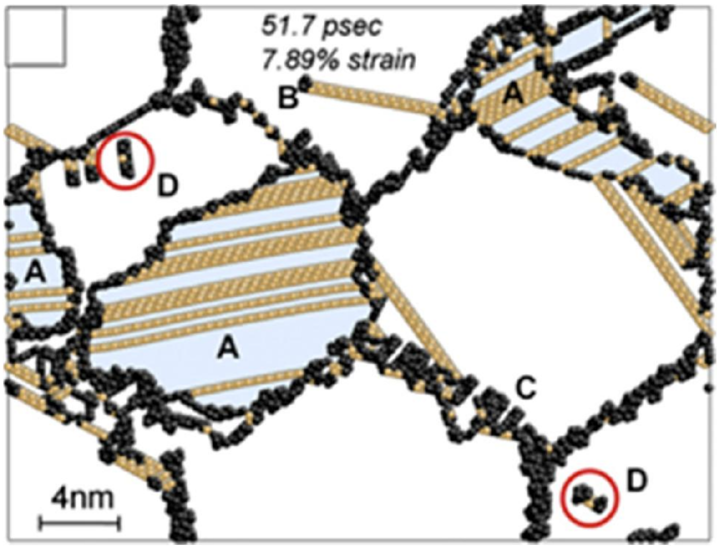

Figure 3-11. Snapshot of 7.89% strained $[11\bar{2}0]$ textured Mg. A) $\{10\bar{1}2\}\,\langle 10\bar{1}1\rangle$ Tensile twin. B) Partial dislocations of 1/3 $[\bar{1}100]$ or 2/3 $[\bar{1}100]$. C) Pyramidal <c+a> partial dislocations D) Extended dislocation with basal slip. Cyan represents twinning region, brown represents stacking fault fcc like atoms, and black represents disorder atoms (non-hcp or fcc). Reproduced from Ref [28] with permission.

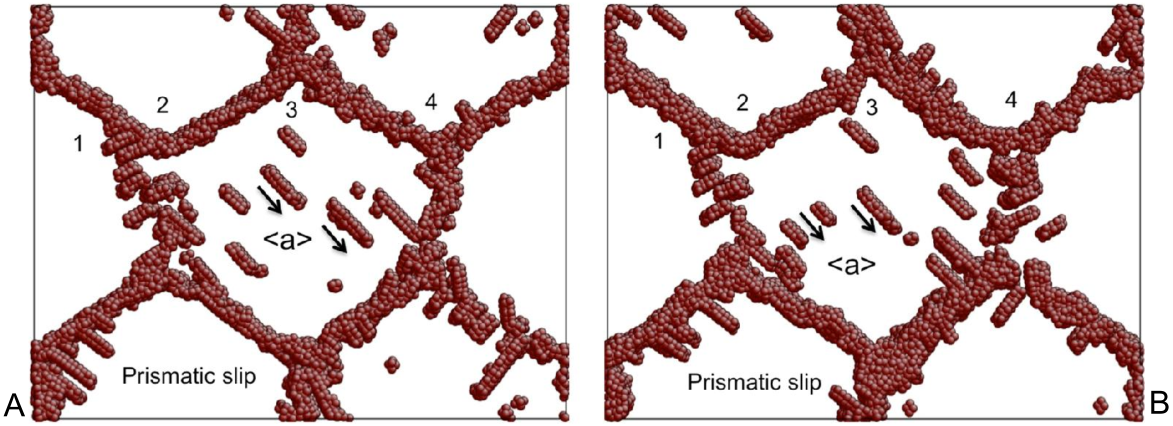

Figure 3-12. Prismatic <a> slip in 7.3% strained $[0001]$-textured structure. A) MA. B) COMB.

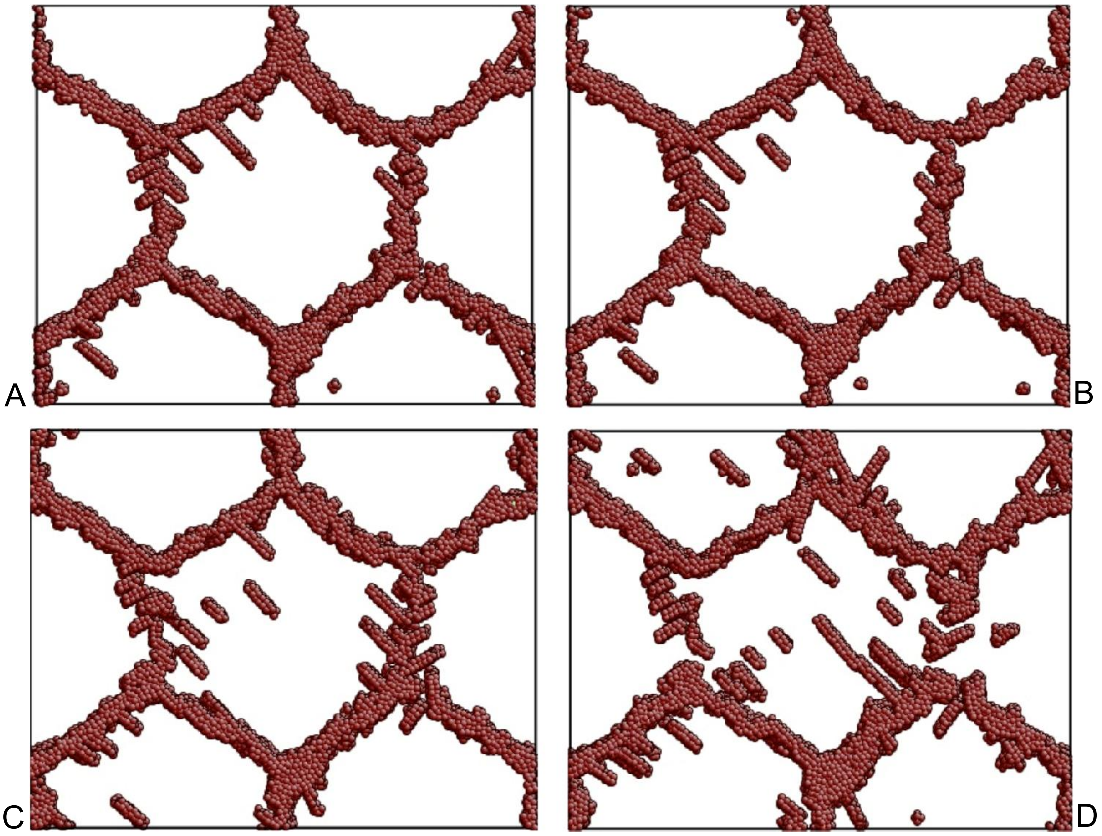

Figure 3-13. Snapshots of microstructure evolution during constant stress test for COMB potential. A) 5.1% strain. B) 5.5% strain. C) 6.2% strain. D) 8.2% strain.

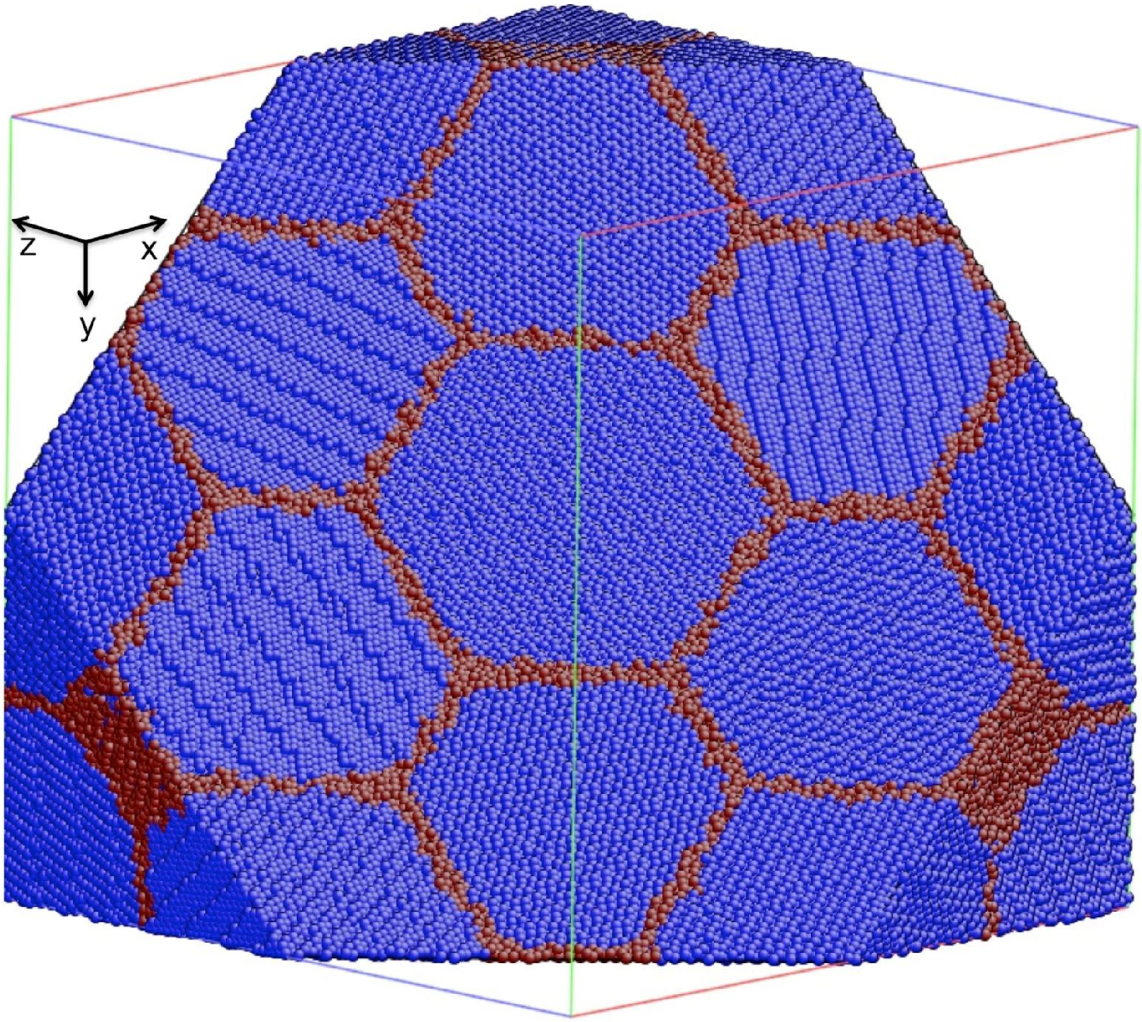

Figure 3-14. The 3D polycrystalline structure consists of 16 randomly oriented grains with the average grain size of 18 nm. The tensile stress is applied along the y direction.

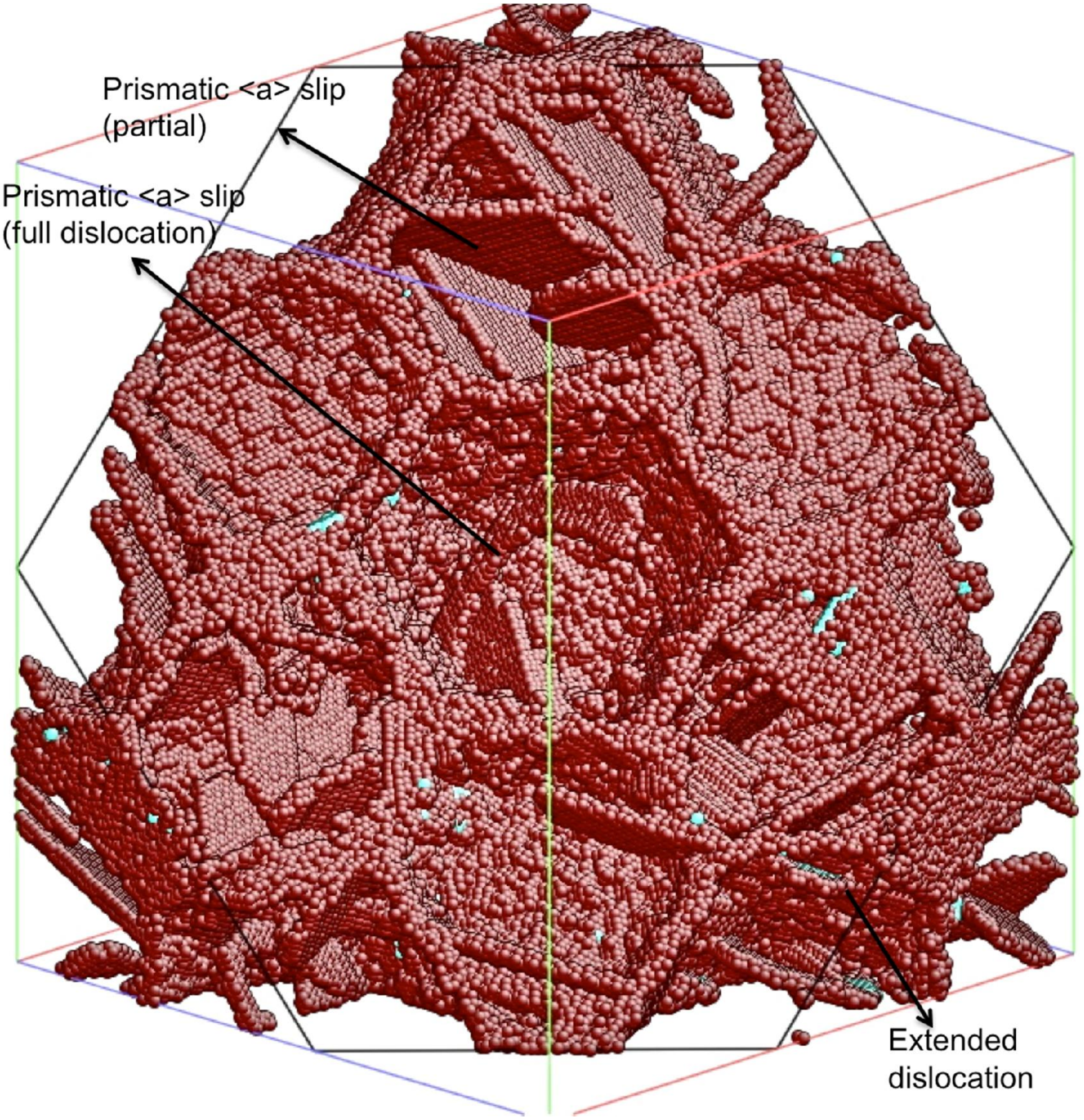

Figure 3-15. CNA map of 3D nanocrystalline Zr using MA potential after tensile test with 8.2% strain. Normal hcp atoms are removed from the strained structure.

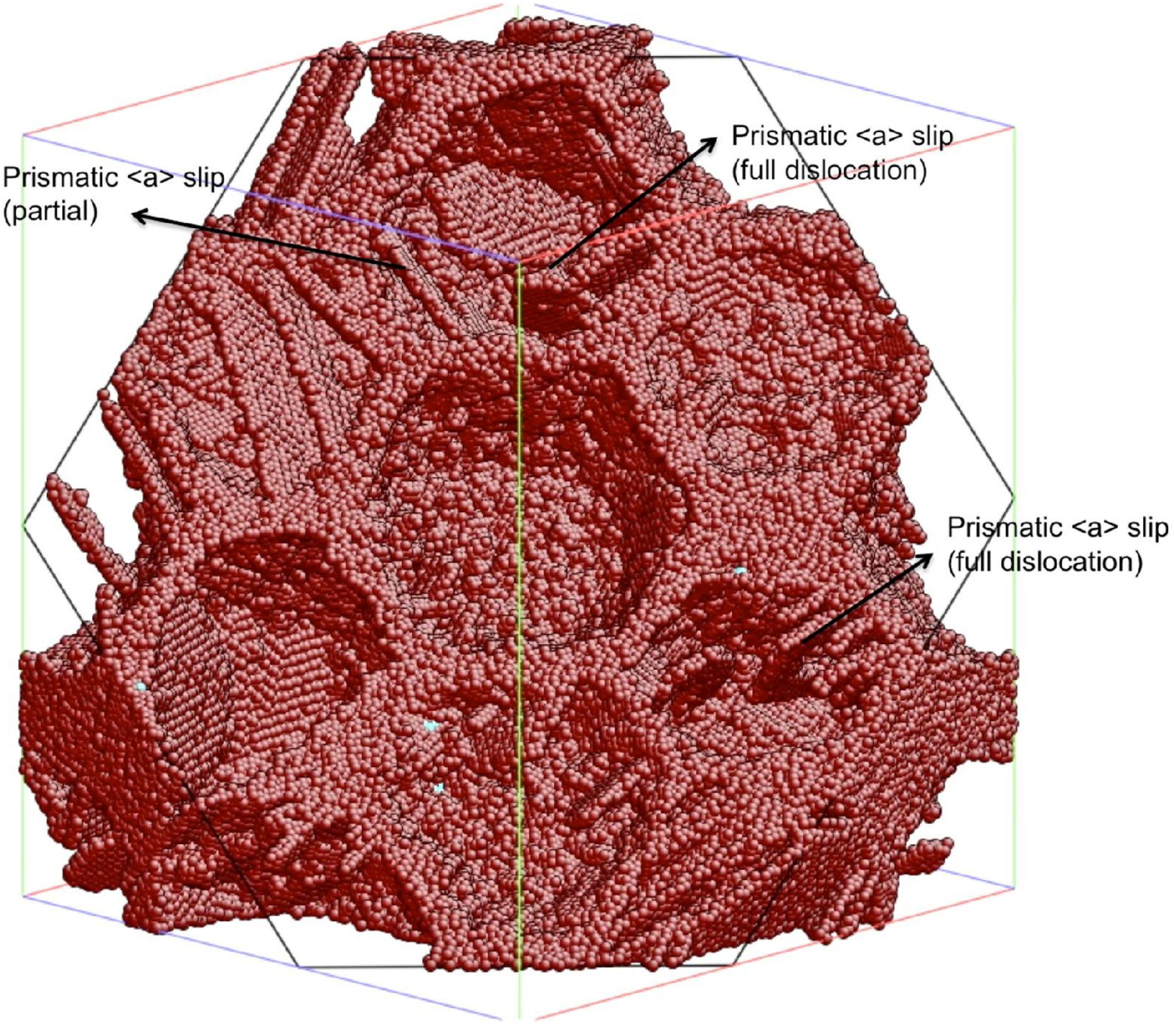

Figure 3-16. CNA map of 3D nanocrystalline Zr using COMB potential after tensile test with 8.2% strain. Normal hcp atoms are removed from the strained structure.

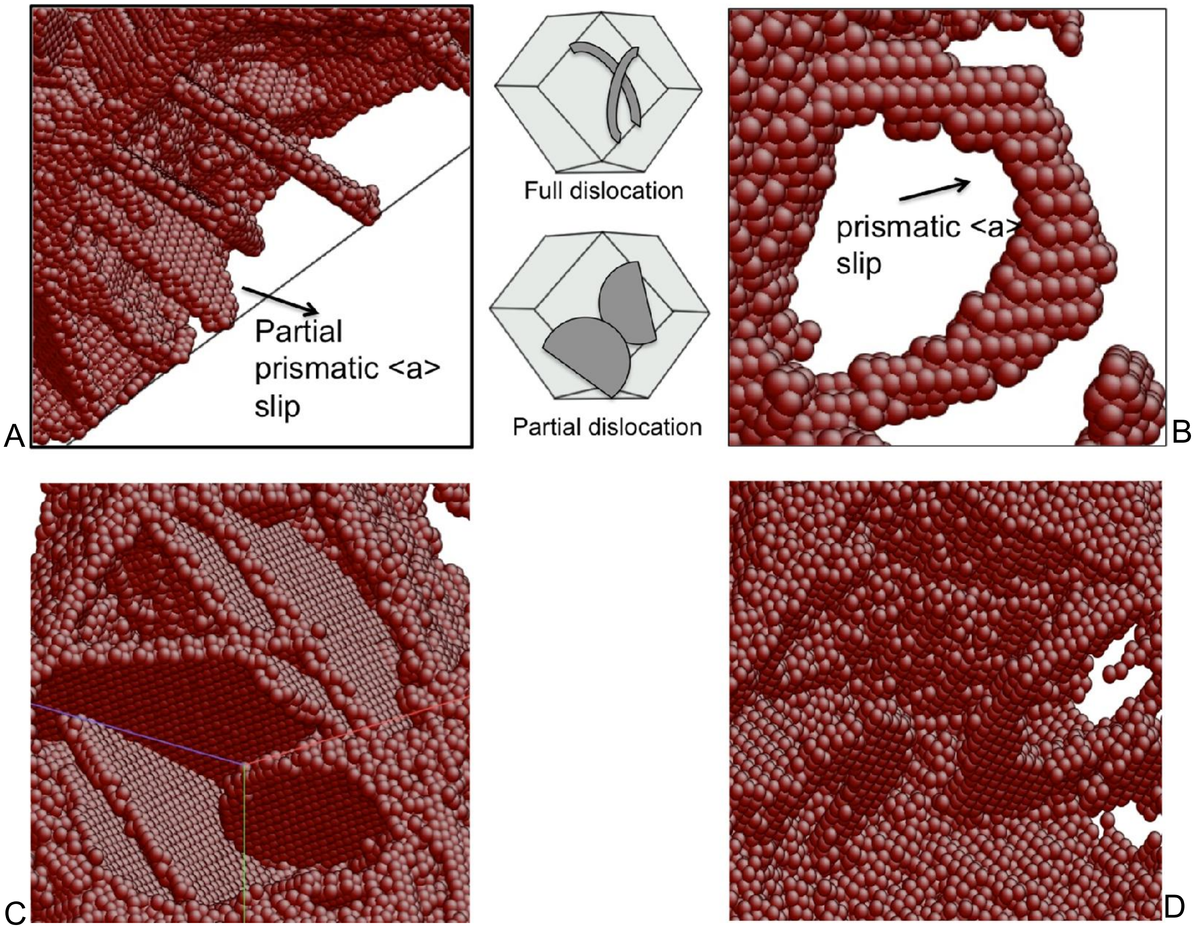

Figure 3-17. Prismatic <a> dislocation. A) Partial prismatic <a> dislocation. B) Full prismatic <a> dislocation. C) Partial prismatic <a> dislocations in one of the grain of MA potential. D) Full prismatic <a> dislocations in one of the grain of COMB potential. Normal hcp atoms have been removed.

CHAPTER 4
NANOINDENTATION OF ZR BY MOLECULAR DYNAMICS SIMULATION

Introduction to Nanoindentation

In Chapter 3, simulations under tension are carried out on polycrystalline Zr. In this chapter, nanoindentation is going to be used as the tool to study the deformation mechanism of single crystal Zr with different surface orientations. Nanoindentation is now an important and widely-used method used to probe the mechanical properties of materials at the nanoscale. In particular, it is commonly used for measuring basic mechanical properties such as hardness and elastic modulus [145]. With further development, other mechanical properties can also be determined using nanoindentation [146, 147]. To observe the nucleation and propagation of dislocations and evolution of defect structures, nanoindentation has been combined with electron microscopy to characterize deformation processes at the nanoscale in real time. Nili et al. have discussed the application and development of in situ nanoindentation technology to several different materials systems [148]; opportunities and challenges of in situ nanoindentation and scratch testing combined with SEM have also been reviewed [149]. Despite the development of in situ nanoindentation, full observation of the nucleation and propagation of dislocations at the atomic level remains challenging.

Molecular dynamics (MD) simulation has been used as an effective tool to study the deformation process of metals [20-22, 24, 28, 150] at the atomic level. For example, Van Swygenhoven and coworkers have shown that the stable and unstable stacking fault energies have a strong influence on deformation behavior in fcc metals[24]. Work on Zr by

---

The work in this Chapter has been published in Z. Z. Lu, M. J. Noordhoek, A. Chernatynskiy, S. B. Sinnott and S. R. Phillpot, *Journal of Nuclear Materials*, 2015, **467**, 742.

Lu using polycrystalline models discussed the relationship between deformation behaviors and the stable and unstable stacking fault energies [150]. The nanoindentation process has been studied using MD in fcc [151-154], bcc [155, 156] and hcp [157] metals. Indeed, computational methods have played a very important role in elucidating the atomic-level mechanisms of dislocation nucleation and propagation under nanoindentation [146].

In this chapter, we perform MD simulations of nanoindentation of a Zr single crystal. Two different empirical potentials are used in the simulation: a Charge Optimized Many Body (COMB) potential [132] and the Mendelev and Ackland Embedded Atom Method (MA EAM) potential [103]. The details of the above two potentials are introduced in the interatomic section of Chapter 2. And the simulation results of 2D textured models and 3D models under tensile condition using the above two potential are analyzed in Chapter 3. The nucleation and propagation of dislocations are analyzed from the atomistic point view. The effects of four different surface orientations are discussed. The influence of stable and unstable stacking energies on deformation behavior is revealed from the comparison of the results of the two potentials. In future work, we will use the extension of the COMB potential to the Zr-H-O system [71] to analyze the effects of oxidation and hydriding on the deformation behavior under nanoindentation, and the hardness of Zr.

Simulation Setup

The LAMMPS MD simulator is used to perform the nanoindentation simulations [158]. The simulation system consists of an active region, a thermostat region and a fixed region, as shown in Figure 4-1. The active region interacts with the indenter and the movement of atoms in this region is governed purely by the forces on them, with no constraints. The thermostat region helps to control the temperature of the whole system;

a Langevin thermostat [83] is applied to this region to control the system's temperature. The fixed region is used to provide rigid support. Periodic boundary conditions are applied in the plane of the Zr film (x and y directions). Prior to the nanoindentation simulation itself, the system is equilibrated under NPT condition at 300K for 50ps. As shown in Figure 4-1, the rigid spherical indenter interacts with the active region. The indentation simulation is performed using the "fix indent" command built in LAMMPS. The force exerted by the spherical indenter on each atom in the Zr film is described by:

$$F(r) = - K(r - R)^2 \qquad r < R \tag{4-1}$$

$$F(r) = 0 \qquad r \geq R \tag{4-2}$$

Here, $K = 10$ eV/Å^3 is the force constant for interactions between the indenter and the film, r is the distance from the atom to the center of the indenter and R (=45Å) is the radius of the indenter.

Regarding the use of a spherical indenter, the simulation results in the elastic region can be easily compared with the classical Hertz Law. However, stress concentration at a sharper indenter tip could lead to stronger stress concentration and thus lower the stress needed for the first plastic event; for example, when using conical indenters, the both experiment and numerical results show that the hardness increases as the corner angle decreases [159]. For the spherical indenter, the hardness depends on the radius of the indenter rather than the indentation depth; the hardness increases as the indenter size decreases [160]. Using the spherical indenter allows us to determine the hardness. In addition, the weaker stress concentration for spherical indenter can reduce the dislocation pile up, making it easier to analyze the individual dislocation behaviors.

Hertz Law

The load-displacement curves are extracted from the indentation simulation. Prior to the first plastic event, the load-displacement curve shows the characteristic features of elastic response. Hertz continuum elastic contact analysis has been used to determine the elastic deformation behaviors for spherical indenter. Within Hertz theory [161, 162],

$$P = \frac{3}{4} E^* R^{\frac{1}{2}} h^{\frac{3}{2}} \tag{4-3}$$

where P is the applied load by the indenter, R is the radius of curvature of the indenter, h is the indentation depth, and E^* is the reduced modulus, defined as [161, 162],

$$E^* = \left\{ \frac{1-v_s^2}{E_s} + \frac{1-v_i^2}{E_i} \right\}^{-1} \tag{4-4}$$

where E_s and v_s are Young's modulus and Poisson's ratio of the sample and E_i and v_i are Young's modulus and Poisson's ratio of the indenter. For the hard indenter E=∞ and ν=0.

The Young's modulus E under a uniaxial stress $\sigma_{[11\bar{2}0]}, \sigma_{[10\bar{1}0]}, \text{and } \sigma_{[0001]}$ is described in terms of components of the compliance tensor S [163-166],

$$E_{[11\bar{2}0]} = (S_{11})^{-1} \tag{4-5}$$

$$E_{[10\bar{1}0]} = (S_{11})^{-1} \tag{4-6}$$

$$E_{[0001]} = (S_{33})^{-1} \tag{4-7}$$

$$E_{30^\circ\, orientation} = (S'_{33})^{-1} \tag{4-8}$$

$$S'_{33} = S_{11} \cdot sin^2(30^\circ) + S_{33} \cdot cos^2(30^\circ)$$
$$+(2S_{13} + S_{44}) \cdot cos^2(30^\circ) \cdot sin^2(30^\circ) \tag{4-9}$$

Under a uniaxial stress $\sigma_{[11\bar{2}0]}, \sigma_{[10\bar{1}0]}, \text{and } \sigma_{[0001]}$, the average Poisson's ratio can be expressed as [163-166],

$$\nu_{[11\bar{2}0]} = \frac{-(S_{12}+S_{13})}{2S_{11}} \tag{4-10}$$

$$\nu_{[10\bar{1}0]} = \frac{-(S_{12}+S_{13})}{2S_{11}} \tag{4-11}$$

$$\nu_{[0001]} = \frac{-(S_{13}+S_{13})}{2S_{33}} \tag{4-12}$$

$$\nu_{30°\ texture} = \frac{-(S'_{13}+S'_{13})}{2S'_{33}} \tag{4-13}$$

$$S'_{13} = S_{13} \cdot [sin^4(30°) + cos^4(30°)]$$

$$+(S_{11} + S_{33} - S_{44}) \cdot cos^2(30°) \cdot sin^2(30°) \tag{4-14}$$

The relationship between stiffness C and compliance S is [166, 167],

$$S_{11} + S_{12} = \frac{C_{33}}{C^2} \tag{4-15}$$

$$S_{11} - S_{12} = \frac{1}{C_{11}-C_{12}} \tag{4-16}$$

$$S_{13} = \frac{-C_{13}}{C^2} \tag{4-17}$$

$$S_{33} = \frac{C_{11}+C_{12}}{C^2} \tag{4-18}$$

$$S_{44} = \frac{1}{C_{44}} \tag{4-19}$$

$$C^2 = C_{33}(C_{11} + C_{12}) - 2C_{13}^2 \tag{4-20}$$

Through Equation 4-4 to Equation 4-20, the reduced modulus E^* of MA EAM and COMB potentials can be obtained, as shown in Table 4-1.

Hardness Calculation Method

The hardness, H, can also be extracted from the nanoindentation [168],

H=P/A (4-21)

Where P is the load in the direction perpendicular to the surface of the indenter and A is the imprinted area of the indenter on the surface. Equation 4-21 will be used to calculate the hardness value of the nanoindentation simulation. The load value P is calculated directly from the simulation by the LAMMPS code. The area A is calculated using

$$A=\pi\delta(2R - \delta) \tag{4-22}$$

Where R is the radius of the indenter and δ is the indentation depth.

The method used to calculate hardness is shown in Figure 4-2. In the elastic region, hardness as defined in Equation 4-21 is a strong function of the indentation depth, but once the plastic deformation begins, its value stabilizes and only fluctuates slightly, reflecting the various operant deformation processes. This is illustrated in the relationship between hardness and indentation depth in Figure 4-3. The hardness is thus obtained by calculating the instantaneous simulated values of the hardness over the indentation depths greater than about 9Å shown in the red dot line region in Figure 4-3. The hardness data in Figure 4-3 is sampled apart of 100fs, one phonon period. The reported hardness is the mean value. The reported error bars of the hardness are represented by the standard deviation from the average in this dataset.

Indentation Speed

In indentation experiments, the velocity of the indenter ranges from tens of nm s^{-1}, to 1 mms^{-1}, [157]. Because of the computational cost of MD simulation, the velocity of the indenter has to be of the order of ms^{-1}, which is much faster than experiment. In order to explore the effect of the indentation speed on the nanoindentation results, simulations were performed under different indenter velocities, ranging from 2 ms^{-1} to 50 ms^{-1}. Because simulations using the MA EAM potential are less time consuming than simulations with the COMB potential, this indentation speed test is performed using only the MA EAM potential and the $[0001]$ orientation. A relatively small system size is used to perform the indentation speed test.

From Figure 4-4, we can see that while the general shape and characteristics of the load-displacement curve are only weakly dependent on the indentation speed, the fine details are substantially different, especially for the fastest nanoindentation simulation of 50 ms^{-1}. These fine details are associated with the various dislocation nucleation and propagation processes, as we describe in detail below. In particular, the first peak in the load map before it drops takes place at the indentation depth of ~5 Å for 2, 5, 10 and 25 ms^{-1} speeds, but at somewhat deeper indentation depth for 50 ms^{-1}. In addition, the magnitude of this first load drop generally increases as the indentation speed decreases, with the 2, 5, and 10 ms^{-1} drops being very similar. Similarly, the 2nd and subsequent peaks on the load-displacement curves for 2, 5, 10, 25 and 50 ms^{-1} are all at different indentation depths. Overall, for slower speeds, there are more peaks and the load drop for each peak is larger. Detailed comparison of the processes, however, which is presented in Figure 4-5 for 5 and 50 ms^{-1}, clearly demonstrates that faster speed results in qualitatively different behavior; namely there are very few dislocation loops observed for 50 ms^{-1}, while they are present in all simulation with slower indentation speeds. For faster indentation speed, pyramidal dislocations mainly form, while for slower indentation speed, pyramidal, basal and prismatic dislocations all form. The hardness obtained from different indentation speeds also varies systematically: 4.5±0.2 GPa (50 ms^{-1}), 4.2±0.2 GPa (25 ms^{-1}), 4.0±0.2 GPa (10 ms^{-1}), 3.6±0.3 GPa (5 ms^{-1}) and 3.5±0.26 GPa (2 ms^{-1}). As the indentation speed decreases, the calculated hardness becomes smaller, becoming essentially independent of indentation speed at low speeds. Subsequent simulations use 5 ms^{-1} as the indentation speed as providing a realistic representation of the dislocation behaviors in Zr at a reasonable computational load.

Substrate Thickness Effect

Systems used in MD simulations have dimensions of tens or at most a few hundred nanometers. The characteristics of the load-displacement curve can be influenced by the system size. In order to understand how the substrate's thickness influences the load-displacement curve in both elastic deformation and plastic deformation regime, MD nanoindentation simulations with different active layer sizes are tested for the $[10\bar{1}0]$ orientation, using the MA EAM potential. It can be seen from Figure 4-6 that the thickness of the active layer has an effect on the load-displacement curve for small thicknesses of the active layer, converging for larger thicknesses, with the results for 168 Å and 190 Å being essentially identical. Further evidence that this system size is adequate come from the fact that the slope of the load-displacement curve matches the Hertz law result. For thicker active layer as shown in Figure 4-6, the first load drop related to the plastic deformation takes place at a smaller indentation depth. As for the characteristics of the dislocations, there are no fundamental structural differences for different active layer thickness, as shown in Figure 4-7. The dislocation loop travels downwards and stops at the bottom of the active region. The strain field of the dislocation loop is different for different thickness active region; in particular, the dislocation loops in the thicker active region are larger in size. As for simulations with the COMB potential, no dislocation loops have been observed, so the substrate thickness effect is smaller for COMB than MA EAM.

Indentation with Different Orientations

In indentation of a single crystal, the crystallographic orientation of the indented surface will promote some deformation modes and hinder others, thus eliciting different mechanical responses [33]. Murty and Charit performed a detailed experimental study of the orientation development and deformation behavior in zircaloys [42]. In this work, four different orientations as shown in Figure 4-8 are chosen to perform the indentation tests: $[0001]$, $[11\bar{2}0]$, $[10\bar{1}0]$ and the $[0001]$ orientation rotated by 30° around the c-axis ("the 30° orientation"), commonly used in zircaloy [42]. From the crystallography point of view, the $[11\bar{2}0]$ and $[10\bar{1}0]$ orientations promote prismatic <a> slip and basal <a> slip. The $[0001]$ orientation promotes pyramidal <a+c> slip. The 30° orientation promotes pyramidal <a+c> slip and basal <a> slip. The load-displacement curves for the two potentials in the elastic region are shown in Figure 4-9, while complete load-displacement curves are shown in Figure 4-10. The hardness values calculated from these data are shown in Figure 4-11. The hardness value is obtained from experiment done on Zr-1Nb-0.05Cu zirconium alloy [169]. The polycrystalline zirconium alloy has more different grain boundary structures and more different grain orientations, which can make it easier for dislocations to nucleate. So it is reasonable that the hardness value of the tested zirconium alloy is smaller than that of the simulation results.

Before the first dislocation activity, the characteristic of the load-displacement curve lies in the elastic regime. The MD results are consistent with the Hertz analysis; in particular, in the elastic regions shown in Figure 4-9, the load does indeed vary as $h^{3/2}$ for both potentials and for all four surface orientations; the reduced modulus values, E^* arHe shown in Table 4-1. These E^* values indicate that the slope of the load-displacement curve of $[0001]$ orientation should be steeper than that of the $[11\bar{2}0]$ orientation and $[10\bar{1}0]$ orientation. Classical theory predicts $E^*_{[11\bar{2}0]} = E^*_{[10\bar{1}0]}$; thus the load-displacement curves of $[11\bar{2}0]$ and $[10\bar{1}0]$ orientations should be the same in the elastic region. For the MA EAM, Figure 4-9A, they match exactly with each other while for the COMB potential, Figure 4-9C, there is a small deviation. In addition, the load-displacement curves of $[11\bar{2}0]$ and $[10\bar{1}0]$ orientations from the simulations also quite closely match the Hertz law for the two potentials, particularly for the MA EAM potential.

By contrast, the load-displacement curves obtained from the simulations for the $[0001]$ orientation are steeper than the Hertz Law predictions for both potentials, with the disagreement being larger for the MA EAM potential than for the COMB potential. For the 30° orientation, the load-displacement curves predicted by the Hertz Law are steeper than the simulation results for both potentials. Although the deviation of the simulation results from the Hertz Law predictions for $[0001]$ and the 30° orientation are slightly larger, the load-displacement curves still show elastic behavior. In summary, the overall elastic response can be quite well represented by Hertz theory.

The plastic deformation begins at the first load drop in the load-displacement curve. It is most pronounced for the $[0001]$ orientation, and less so for the other orientations considered. As shown in Figure 4-10A for the MA EAM potential, the 30° orientations support the largest load, while the $[10\bar{1}0]$ support the lowest load. As shown in Figure 4-10B for the COMB potential, the $[11\bar{2}0]$ orientation supports the largest load, while the 30° orientation supports the lowest load. The load drops in the load-displacement curve represent the plastic deformation events throughout the indentation simulation. The magnitudes of the load drop and the indentation depths where the load drop happens all vary slightly for different orientations of different potentials. One obvious similarity for both potentials is that the $[0001]$ orientation has the largest first load drop at around 5 Å indentation depth. The details of the plastic deformation events are discussed later.

The comparison of hardness for the four simulated orientations of two potentials is shown in Figure 4-11. The 30° orientation (MA EAM) and $[11\bar{2}0]$ orientation (COMB) have highest hardness value, while the $[10\bar{1}0]$ orientation (MA EAM) and the 30° orientation (COMB) have the lowest. However, as shown in Figure 4-3, the hardness fluctuates with the indention depth. So when taking into account the fluctuations represented by the errors bars in Figure 4-11, the difference of the hardness value for different orientations of the two potentials is not significant.

The atomic-level details of the deformed structures combined with the elastic properties provide insights into these differences in the hardness and load-displacement curves. The deformed atomic structures of the four orientations are shown in Figure 4-12 (MA EAM) and Figure 4-13 (COMB) where again atoms are color coded in accord with Common Neighbor Analysis (CNA) [126, 127]. The calculated total dislocation line length, dislocation segments and junctions of all the deformed structure using the Crystal Analysis Tool are listed in Table 4-2 [123-125]. The Crystal Analysis Tool has some difficulties in capturing the dislocation structure in the COMB simulations. So the dislocation density of the COMB simulations is not listed in Table 4-2.

MA EAM Indentation Analysis

From the deformed structures of four different orientations shown in Figure 4-12, we can see that dislocation loops are commonly activated for the MA EAM potential.

The dislocation loop consists of partial dislocations on the basal plane and dislocations on the prismatic planes. Dislocation loops are only observed traveling along the <a> direction on prismatic plane inside the bulk or on the surface in this nanoindentation simulation. The dislocation loop observed in this nanoindentation turns out to be the most stable interstitial loop in Zr, and has been observed by de Diego and coworkers in their simulation work [170]. They found that the rectangular self-interstitial loop that consists of prismatic dislocations and basal partial dislocations has the lowest formation energy and highest binding energy [170].

For the $[10\bar{1}0]$ and $[11\bar{2}0]$ orientations, as shown in Figures 4-12A and 4-12B, the dislocation loops form under the indenter and travel along the <a> direction on the prismatic plane. Despite their similar dislocation behaviors, there is a difference of hardness between the $[11\bar{2}0]$ orientation (5.27 GPa) vs. $[10\bar{1}0]$ orientation (4.65 GPa). When considering the elastic deformation contribution, as discussed in the previous section the $[11\bar{2}0]$ orientation and $[10\bar{1}0]$ orientation have similar load-displacement curves due to the same reduced modulus. With regards to the plastic deformation contribution, the Schmid factors [171] for prismatic and basal slips are identical for these two orientations: 0.433 (prismatic planes neither parallel nor perpendicular to the indentation direction) and 0 (prismatic planes parallel or perpendicular to the indentation direction) for prismatic slips and 0 for basal slip. However, for the $[10\bar{1}0]$ orientation, the surface is one of the prismatic planes; therefore dislocation loops travelling along the <a> direction on the surface are commonly observed in these nanoindentation simulations. This dislocation loop motion on the surface may contribute to the lower hardness for the $[10\bar{1}0]$ orientation. In addition, the size and the detailed atomic structures of dislocations are different for these two orientations, with the dislocation loops formed in the $[11\bar{2}0]$ orientation being generally larger. The detailed atomic structures of one of the dislocation loops from each orientation are shown in Figure 4-14. The sizes of the dislocation loop for $[10\bar{1}0]$ and $[11\bar{2}0]$ orientations are 42Å×55Å and 66Å×55Å correspondingly. The basal partial component of the dislocation loop is longer for $[11\bar{2}0]$ (66 Å) than for $[10\bar{1}0]$ (42 Å). In addition, more jogs are formed in the basal partial component of the dislocation loop for the $[11\bar{2}0]$ orientation than for the $[10\bar{1}0]$ orientation. From the dislocation structures we conclude that more plasticity events take place in the $[11\bar{2}0]$ orientation than in the $[10\bar{1}0]$ orientation. This is confirmed by the calculation results from the Crystal Analysis Tool: the $[11\bar{2}0]$ orientation yields longer total dislocation line length (1608 Å vs. 1315 Å for $[10\bar{1}0]$), more segments (72 vs. 51) and more junctions (36 vs. 23). From the load-displacement curve, we can see that for the $[10\bar{1}0]$ orientation the large load drops happen at an early stage of the plastic deformation, while for $[11\bar{2}0]$ orientation the large load drops happen at a later stage of the plastic deformation. After 15 Å indentation depth, the load response for $[11\bar{2}0]$ orientation becomes obviously larger than for the $[10\bar{1}0]$ orientation. This leads to the result that the hardness of $[11\bar{2}0]$ (5.27 GPa) is higher than that of $[10\bar{1}0]$ orientation (4.65 GPa). However, when taking into account the uncertainties associated with the fluctuations shown in Figure 4-3 and Figure 4-11, these values do not differ significantly. In summary, taking into account both of the contribution from elastic and plastic deformation, the $[11\bar{2}0]$ orientation yields similar hardness as $[10\bar{1}0]$ orientation does.

For the 30° and $[0001]$ orientations, as shown in Figures 4-12C and 4-12D, dislocation loops form under the indenter. For both orientations, the dislocation loops only travel along the surface. The second basal partial dislocation cannot nucleate to form a full dislocation loop. It is thus not surprising that dislocation loops are not observed to leave the surface to travel inside the bulk. Pyramidal slip is observed along with the dislocation loops.

Considering the elastic deformation, the reduced modulus of the $[0001]$ orientation has the highest value among the four orientations. The reduced modulus of the 30° orientation (129 GPa) lies between those of the $[0001]$ orientation (133 GPa) and $[11\bar{2}0]$ orientation (114 GPa) but very close to $[0001]$ orientation. Thus, from the viewpoint of elasticity, the $[0001]$ orientation should have the highest load response and the steepest slope of the load-displacement curve in the elastic region, which agrees with the simulation results as shown in Figure 4-10A.

Comparing the details of the plastic deformation of these two orientations may give some insights to the difference in the magnitude of the load drop. As shown in Figures 4-12C and 4-12D, the dislocation density is much higher for the $[0001]$ orientation than for the 30° orientation. In addition, the calculations from the Crystal Analysis Tool show that the $[0001]$ orientation has a total length of dislocation of 1132 Å compared to 765 Å for the 30° orientation, confirming that the 30° orientation has the lowest dislocation density. This lower dislocation density is consistent with the small load drop. The small dislocation density combined with the moderately reduced modulus results in the largest hardness value (5.68 GPa) for the 30° orientation among the four orientations. Although it has the largest reduced modulus, the $[0001]$ orientation has a hardness of only 5.13 GPa due to the relative ease with which plastic events are nucleated. Furthermore, this ease of nucleation for $[0001]$ orientation is consistent with the crystallography: the dislocation loop glides in the <a> direction on prismatic plane, which is parallel to the surface for the $[0001]$ orientation.

COMB Indentation Analysis

As we saw in Figure 4-11, the hardness values predicted from the COMB potential are similar to those predicted from the MA EAM potentials. Nevertheless, as we now discuss, the atomic-level details of the plastic response are somewhat different.

The deformed structures of four orientations are shown in Figure 4-13 for the COMB potential. The prismatic <a> and pyramidal dislocation are the most prevalent; moreover, there are very few basal partial dislocations. In the absence of basal partial dislocations, the dislocation loop of basal and prismatic dislocations seen in MA EAM simulation is not observed in the COMB simulation. The reasons for this difference will be discussed in the following section.

For the $[10\bar{1}0]$ and $[11\bar{2}0]$ orientations, as shown in Figures 13 (a) and (b), prismatic <a> dislocations and pyramidal dislocations are most commonly activated during the indentation test. In the elastic deformation regime, the $[10\bar{1}0]$ and $[11\bar{2}0]$ orientations yield very similar load-displacement curves because they have same reduced moduli. In combination with their similar dislocation behaviors, this results in similar hardness values, 5.37 GPa for the $[10\bar{1}0]$ orientation and 5.46 GPa for the $[11\bar{2}0]$ orientation.

For the 30° and $[0001]$ orientations, as shown in Figures 4-13C and 4-13D, pyramidal <a+c> dislocations predominate. For the $[0001]$ orientation, the load-displacement curve has the highest load response in the elastic regime, as shown in Figure 4-10B. Moreover, as in the case of the MA EAM potential, the load drop related to the first plastic event, at around 5 Å indentation depth, is the largest among the four orientations. The largest elastic deformation combined with the largest load drop leads to a moderate hardness value of 5.04 GPa, smaller than that of $[11\bar{2}0]$ and $[10\bar{1}0]$ orientations. For the 30° orientation, as a result of the smallest reduced modulus (121 GPa) among the four orientations, it has the lowest load response in the elastic regime, as shown in Figure 4-10B. The dislocation behavior of the 30° orientation is very similar to the $[0001]$ orientation. With the contributions from both elastic and plastic deformation, the 30° orientation yields the smallest hardness value of 4.79 GPa.

Comparison between MA EAM and COMB Potentials

In the elastic regime, both the MA EAM and COMB potential agree with the Hertz Law predictions especially for the order of the load response of four different orientations. In the plastic regime, the prismatic <a> dislocation and pyramidal dislocation are most commonly observed for both potentials. Among the four orientations, the $[0001]$ orientation has the largest first load drop for both potentials, which has a significant influence on the hardness value. And as we saw in Figure 4-11, the hardness values predicted from the COMB potential are similar to those predicted from the MA EAM potentials when taking into account the uncertainties represented by the error bars. Nevertheless, the atomic-level details of the plastic response are different. In contrast with the MA EAM potentials, no dislocation loops are emitted for the COMB potential. The reason for this difference is discussed as below.

As is well known, the stacking fault and unstable stacking fault energies play an important role in determining the dislocation behaviors [24]. A comparison of the stacking fault energies of MA EAM potential and COMB potential was reported previously [150]. Summarizing these previously reported results, the stable and unstable stacking fault energies along the basal partial <a> path for the COMB potential are higher than for the MA EAM potential, while the most reliable DFT values are the lowest. This explains why basal partial dislocations and stacking fault structures are rare in COMB; in this regard the MA EAM potential should have higher materials fidelity that the COMB potential. Also the ratio of energy barriers for basal slip and prismatic slip, $\frac{\gamma_{basal}}{\gamma_{prismatic}}$, is 1.13 for MA EAM and 1.41 for COMB potential, while the DFT [137] value is 1.26. That is, for the MA EAM potential prismatic dislocations should be only slightly more prevalent than basal partial dislocations. This is consistent with the dislocation loop consisting of basal partial dislocations and prismatic dislocations being commonly observed for MA EAM potential. By contrast, for the COMB potential prismatic dislocations are more likely to form than basal partial dislocations. For all four orientations, the COMB nanoindentation simulations display prismatic dislocations rather than basal dislocations. Because the stacking fault energies for the COMB potential is higher than for the MA EAM potential[150], the dislocation density for MA EAM potential is higher than COMB potential.

DFT calculations generally offer higher materials fidelity than calculations with classical potentials; thus the DFT results should more closely match experiment. While nanoindentation with DFT is not computationally feasible, the fact that the energy barrier ratio for DFT lies between the values for COMB and MA EAM suggests that formation and propagation of dislocation loops in Zr metal should take place, but not to the same degree as predicted by MA EAM potential.

Microstructure Evolution during Nanoindentation for $[10\bar{1}0]$ Orientation

The initial stages of dislocation evolution are shown in Figure 4-15 (MA EAM) and Figure 4-16 (COMB). When the dislocation starts to form in the area under the indenter, the deformed structures are similar for both potentials. The prismatic <a> dislocation and stacking fault on the basal plane are observed as shown in Figure 4-15A and Figure 4-16A. For the MA EAM potential, a prismatic <a> dislocation form first with glide plane is parallel to the surface. This is followed by the basal partial <a> dislocation that connects with one end of the prismatic <a> dislocation. Then another basal partial <a> dislocation forms and connects with the other end of the prismatic <a> dislocation. Thus the formation of a dislocation loop that consists of two basal partial <a> dislocations and one prismatic <a> dislocations is completed. The dislocation loop glides on the $[10\bar{1}0]$ surface along the <a> direction. In contrast, for the COMB potential, as shown in Figure 4-16, the prismatic <a> dislocation continues to glide on the initial prismatic plane when it forms. At higher stress the pyramidal dislocations form and glide in addition to prismatic ones; however, no basal dislocations are produced. This picture is consistent with the energy barrier ratios for the two potentials. In addition, pyramidal dislocations have only been observed for the COMB potential. Pyramidal <a+c> dislocation provides the needed deformation in <c> direction.

In addition, for the MA EAM potential, dislocation loops form under the indenter and glide into the bulk, as shown in Figure 4-17. The first defect structure consists of a leading prismatic dislocation and two basal partials, as shown in Figure 4-17A. This then evolves into a structure that consists of two basal partial dislocations and a prismatic dislocation gliding into the bulk along the prismatic plane, as shown in Figures 4-17B and 4-17C. The defect structure then starts to break off from the two dislocations. A similar break-off behavior was also observed in MD simulations of nanoindentation of a bcc metal [155]. The breaking off process of the defect structure is shown in Figure 4-18 from a different direction. We can see that while the two basal partial dislocations and a prismatic dislocation defect structure glide into the bulk through the screw <a> component of two dislocations, the two dislocations appear to have edge <a> components. The two dislocations also move in the <c> direction, as shown in Figure 4-18B. When the dislocations moving along the <c> direction finally meet, as shown in Figure 4-18C, the break-off behavior takes place. The final dislocation loop structure is shown in Figure 4-18D. Thus, while the COMB potential shows dislocation <c> component through pyramidal <c+a> slip, the MA EAM potential shows a dislocation <c> component in the dislocation loop formation process.

Microstructure Evolution during Nanoindentation for $[0001]$ Orientation

The initial dislocation behaviors of MA EAM and COMB potential for $[0001]$ orientation are shown in Figure 4-19. For MA EAM, the basal partial dislocation and prismatic dislocation start to form under the indenter. The basal partial dislocation and prismatic dislocation forming a dislocation loop glide on the surface (basal plane) along the <a> direction. For COMB, pyramidal <a+c> dislocations start to form under the indenter. While because of the higher energy barrier for basal partial dislocations compared to MA EAM, basal partial dislocations are not expected in the COMB potential, they are not observed in the MA EAM simulations either. It appears that the energy barrier for a pyramidal <a+c> dislocation to form is relatively low since we observe pyramidal dislocations in all four orientations for COMB. Also for MA EAM, the basal partial dislocation and prismatic dislocation seem to facilitate each other, because basal partial dislocations and prismatic dislocations always connect with each other to form a loop. Thus the COMB potential displays deformation in the <a> and <c> direction by pyramidal <a+c> dislocation, whereas the MA EAM potential displays the deformation in <a> and <c> direction by forming dislocation loops. The detail of the formation of dislocation loops is shown in Figure 4-20. First, the prismatic <a> dislocation forms connected with the basal partial dislocations as shown in Figure 4-20A. Then the basal partial dislocation grows with several jogs that contain a <c> component as shown in Figures 4-20B and 4-20C; the second prismatic dislocation then forms. The dislocation loop, consisting of two prismatic dislocations and one basal partial dislocation, moves along the surface (basal plane) as shown in Figure 4-20D. The movement of the dislocation loop along the surface is also seen in the $[10\bar{1}0]$ orientation. However due to the different orientation, the dislocation loop seen in $[10\bar{1}0]$ orientation consists of two basal partial dislocations and one prismatic dislocation.

Summary on Nanoindentation MD Simulation of Zr

In this work, nanoindentation MD simulation has been performed for four different orientations of single crystal Zr using MA EAM and COMB potentials. The load-displacement curves present the elastic characteristics in the elastic region for both potentials. The factors that influence hardness value have been illustrated. Both elastic and plastic deformations contribute to the hardness value. Due to the small differences in the reduced modulus for different orientations of the tested four orientations, the plastic deformation plays a more important role in determining the hardness value. The load drop associated with dislocation behaviors has a direct impact on the hardness value, with larger load drops tending to lead to a relatively small hardness. Furthermore, the dislocation behaviors and the atomic structures of the dislocations during the nanoindentation largely depend on the stable and unstable stacking fault energy and the ratio of unstable stacking fault energies on different slip planes. The rather small difference in $\frac{\gamma_{basal}}{\gamma_{prismatic}}$ values leads to very different dislocation behaviors in the nanoindentation test. For MA EAM, dislocation loops consist of basal partial dislocation and prismatic <a> dislocation are extensively observed. In contrast, for COMB, no basal dislocations or dislocation loops are produced. The comparison of the two potential during nanoindentation shows that the competition between different types of dislocation on different planes under nanoindentation is mainly determined by the small difference of the unstable stacking energy on the gliding plane.

In summary, while we see that the specifics of the plastic response depend on the energetics of the stacking faulty, which differ for the two potentials, the overall responses for all four surface orientations and for both potentials are rather similar. We can thus expect that they reasonably well describe the experimental mechanisms of deformation in Zr.

Table 4-1. The reduced modulus for MA EAM and COMB potentials.

	$E^*_{[11\bar{2}0]}$ (GPa)	$E^*_{[10\bar{1}0]}$ (GPa)	$E^*_{[0001]}$ (GPa)	$E^*_{30^\circ\ orientation}$ (GPa)
MA EAM	114	114	133	129
COMB	125	125	141	121
Experiment [163]	109	109	138	106

Table 4-2. Total dislocation line length, and number of dislocation segments and junctions calculated using the Crystal Analysis Tool.

	Total dislocation line length (Å)	Dislocatio Density (m^{-2})	Segments	Junctions
MA EAM $[11\bar{2}0]$	1608	1.17×10^{16}	72	36
MA EAM $[10\bar{1}0]$	1315	0.96×10^{16}	51	23
MA EAM [0001]	1132	0.9×10^{16}	67	32
MA EAM 30° orientation	765	4.02×10^{15}	32	14
COMB $[11\bar{2}0]$	219		3	0
COMB $[10\bar{1}0]$	203		7	1
COMB $[0001]$	0		0	0
COMB 30° orientation	6.1		1	0

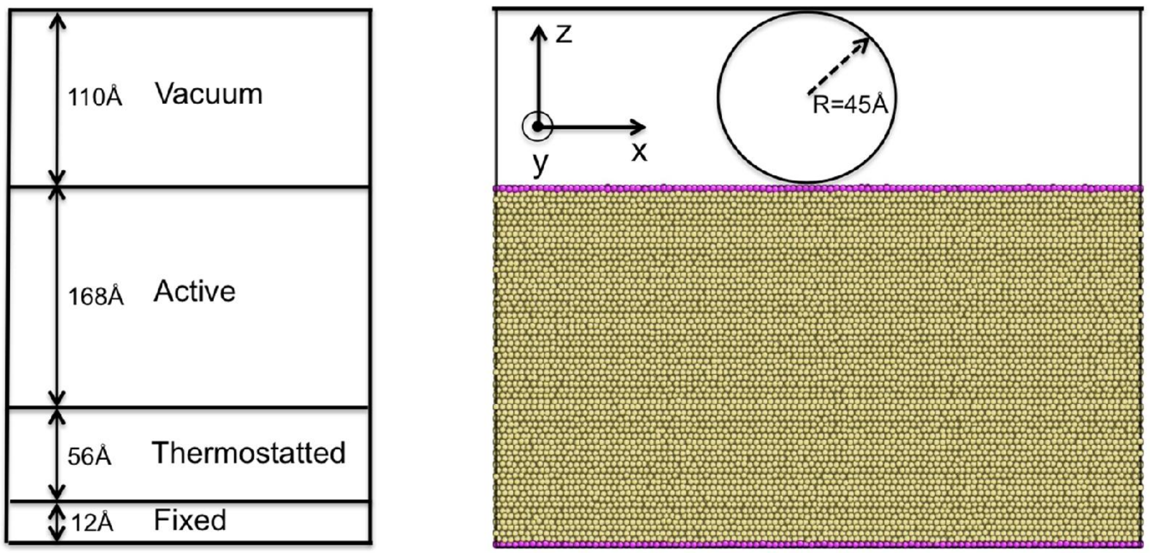

Figure 4-1. Schematic of the nanoindentation simulation.

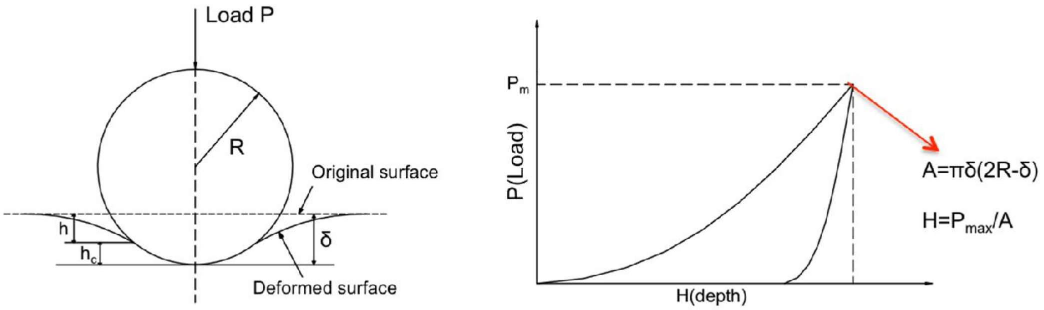

Figure 4-2. Method used to calculate hardness, after reference [145, 147].

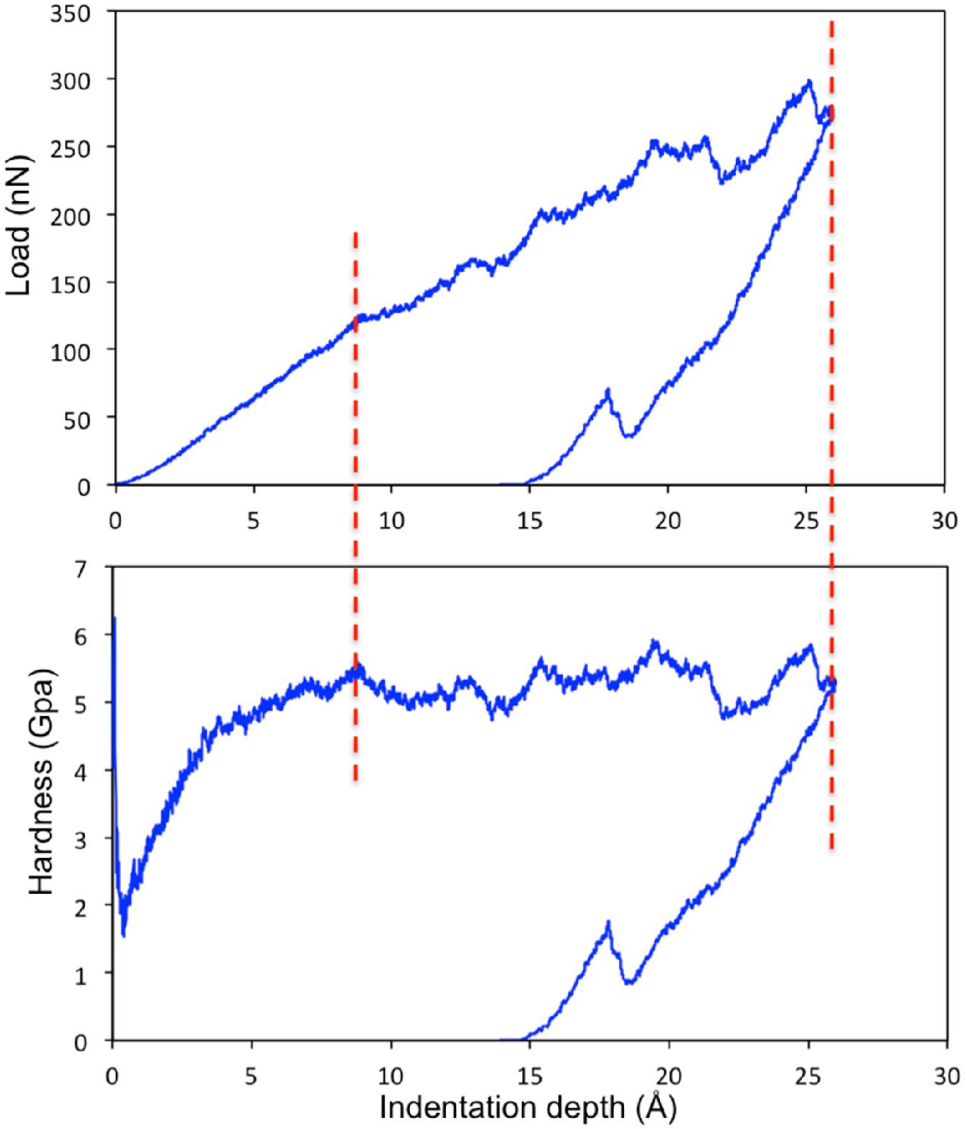

Figure 4-3. Relationship between load, hardness and indentation depth for $[11\bar{2}0]$ orientation. The reported hardness and its uncertainty are obtained for depths bounded by the red dotted lines.

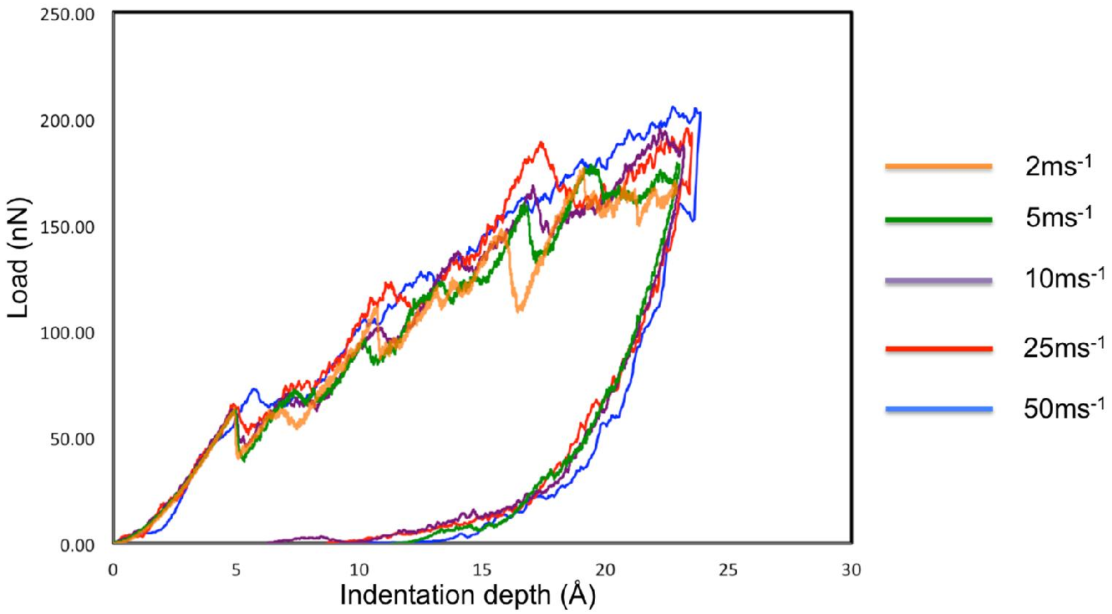

Figure 4-4. The loading and unloading curve of Zr using MA EAM potential at 2 ms^{-1}, 5 ms^{-1}, 10 ms^{-1}, 25 ms^{-1} and 50 ms^{-1}.

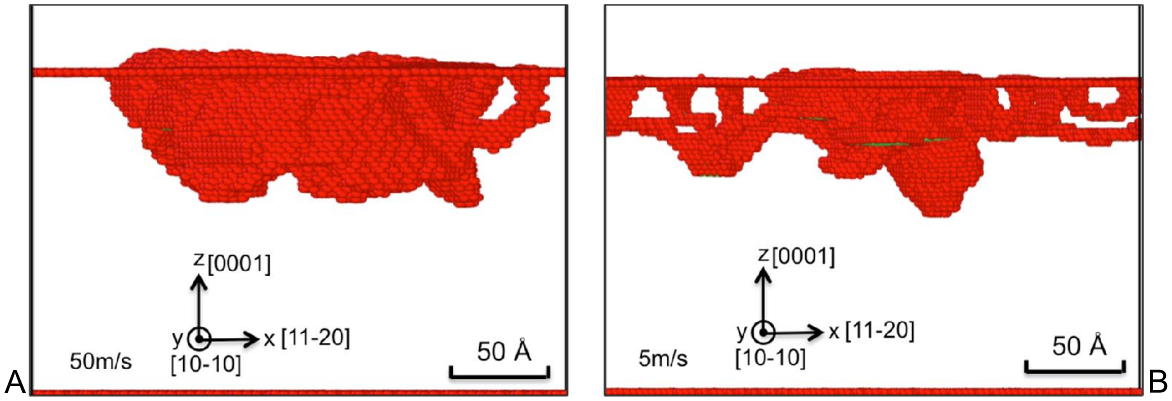

Figure 4-5. Indentation at 24 Å indentation depth of MA EAM potential using different indentation speed. A) 50 ms^{-1}. B) 5 ms^{-1}. Red atoms represent disordered atoms. Atoms in hcp environments are not shown.

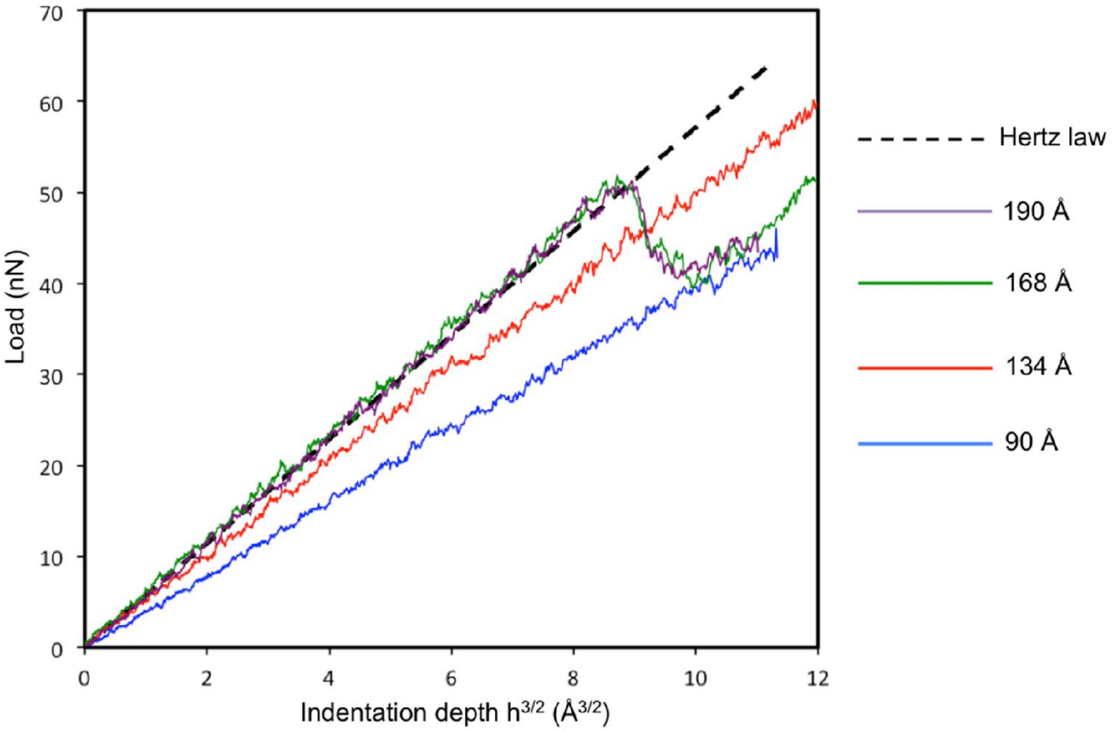

Figure 4-6. Load-indentation curves of $[10\bar{1}0]$ orientation using the MA EAM potential with the thickness of the active region ranging from 90Å to 190Å.

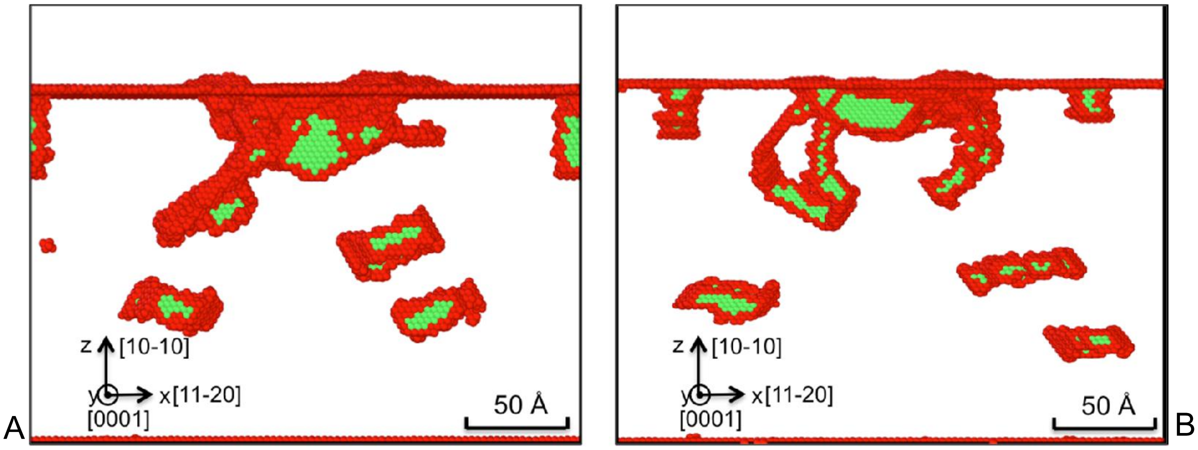

Figure 4-7. Deformed structures of $[10\bar{1}0]$ orientation using the MA EAM potential at 22Å indentation depth. A) 134Å thick active region. B) 168Å thick active region.

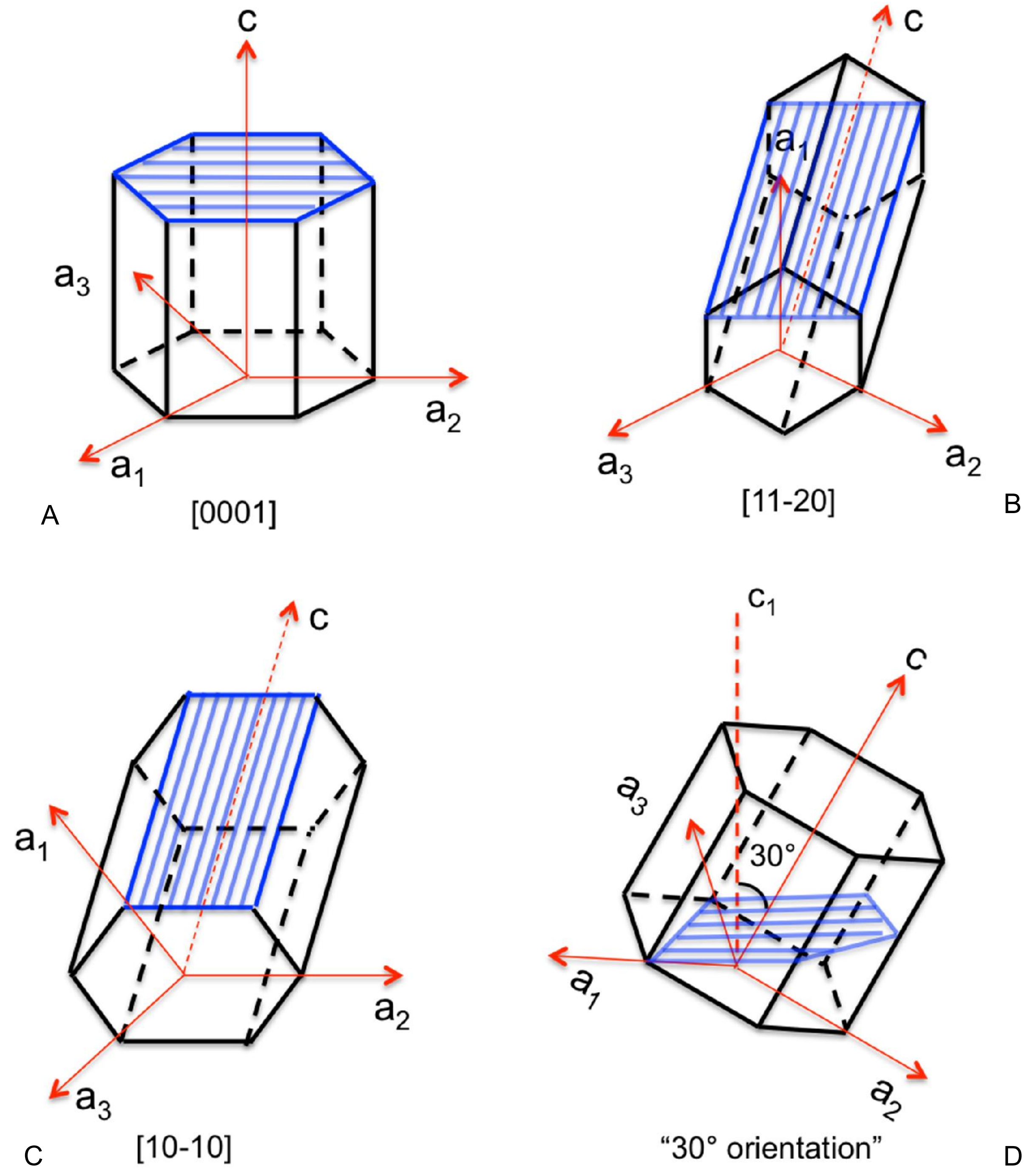

Figure 4-8. Four different orientations of Zr used in the nanoindentation simulation, with the surface plane shown in blue. A) $[0001]$ orientation. B) $[11\bar{2}0]$ orientation. C) $[10\bar{1}0]$ orientation. D) The “30° orientation”. The exposed plane in D is perpendicular to c_1.

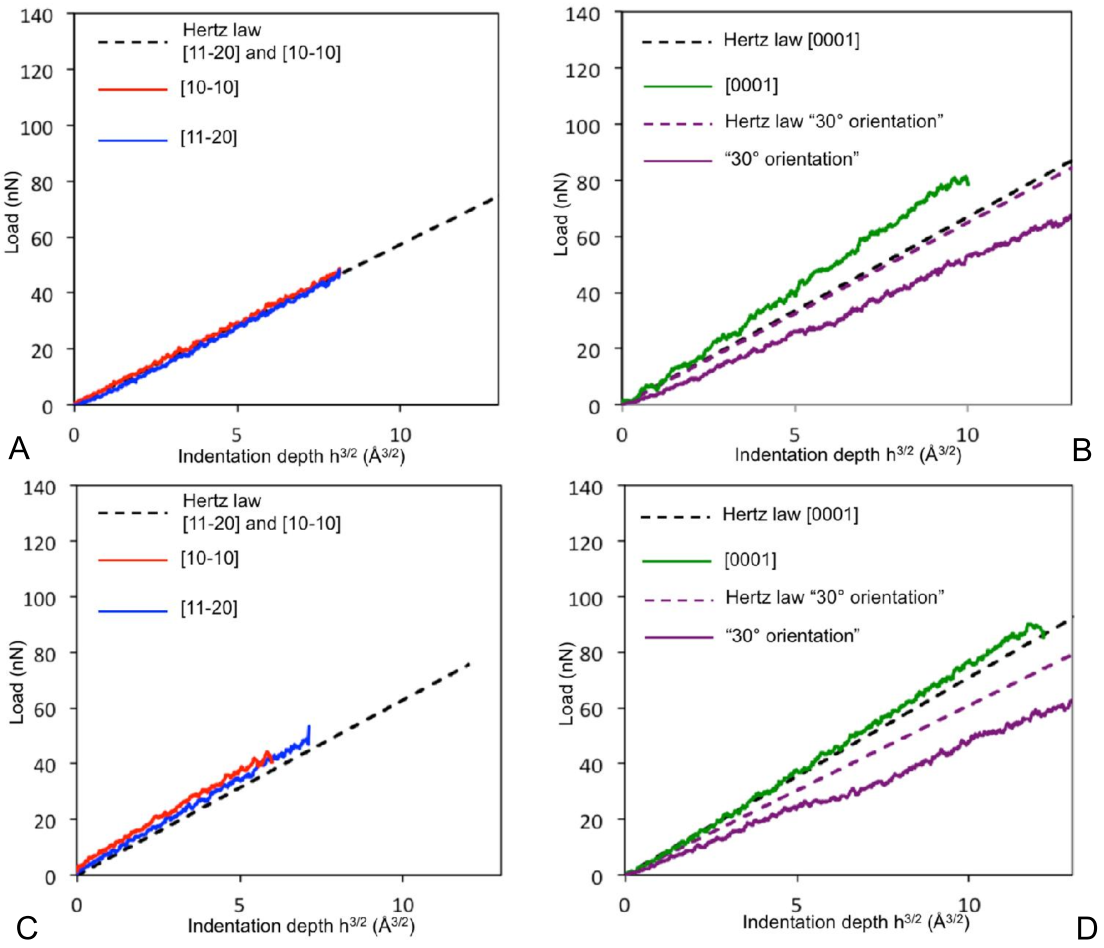

Figure 4-9. Load-displacement curves in the elastic region. A) MA EAM $[11\bar{2}0]$ and $[10\bar{1}0]$ orientation. B) MA EAM $[0001]$ orientation and 30° orientation. C) COMB $[11\bar{2}0]$ and $[10\bar{1}0]$ orientation. D) COMB $[0001]$ orientation and 30° orientation. All the data from the MD simulations are fitted using a moving average method.

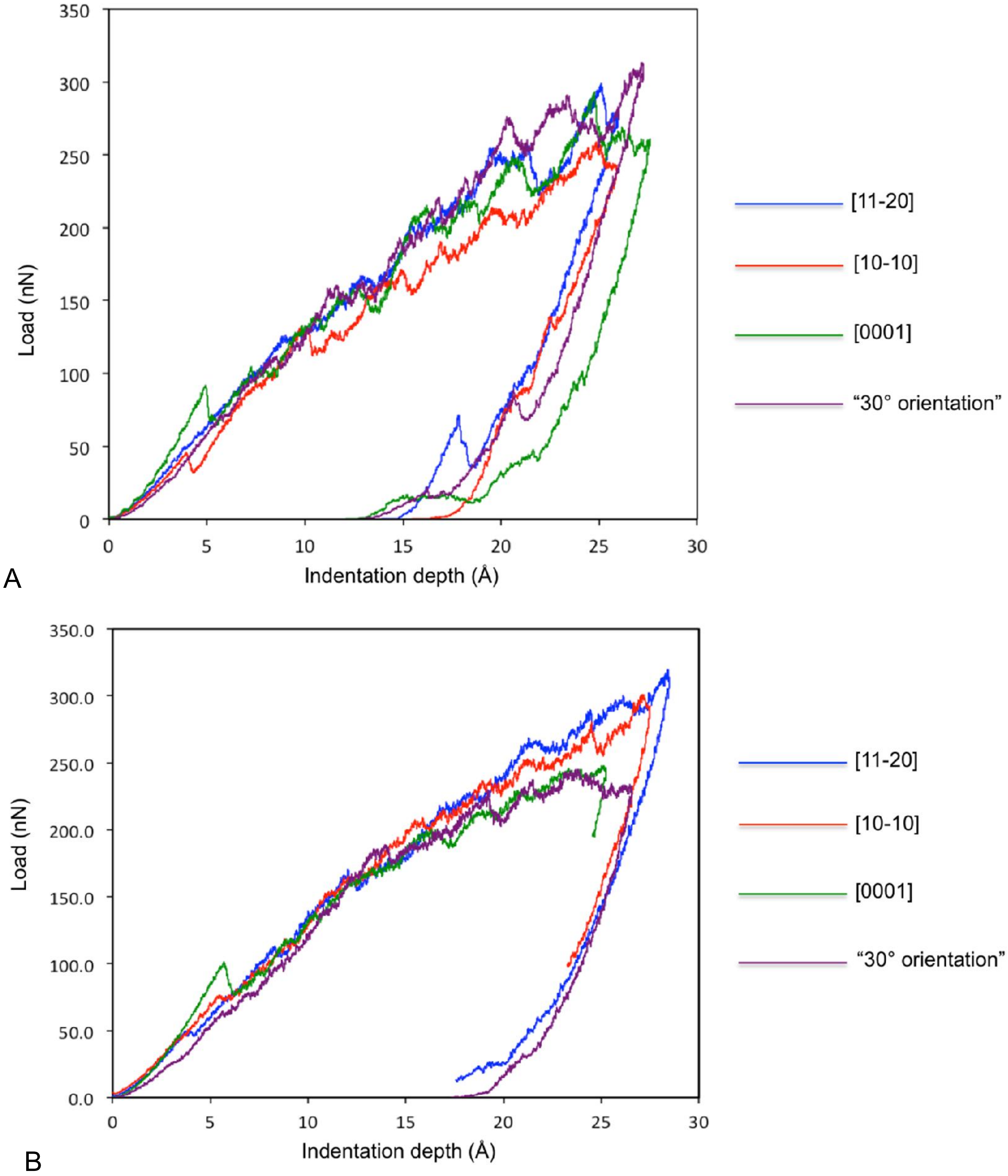

Figure 4-10. Load-displacement curve of four different orientations for the nanoindentation simulation. A) MA EAM potential. B) COMB potential.

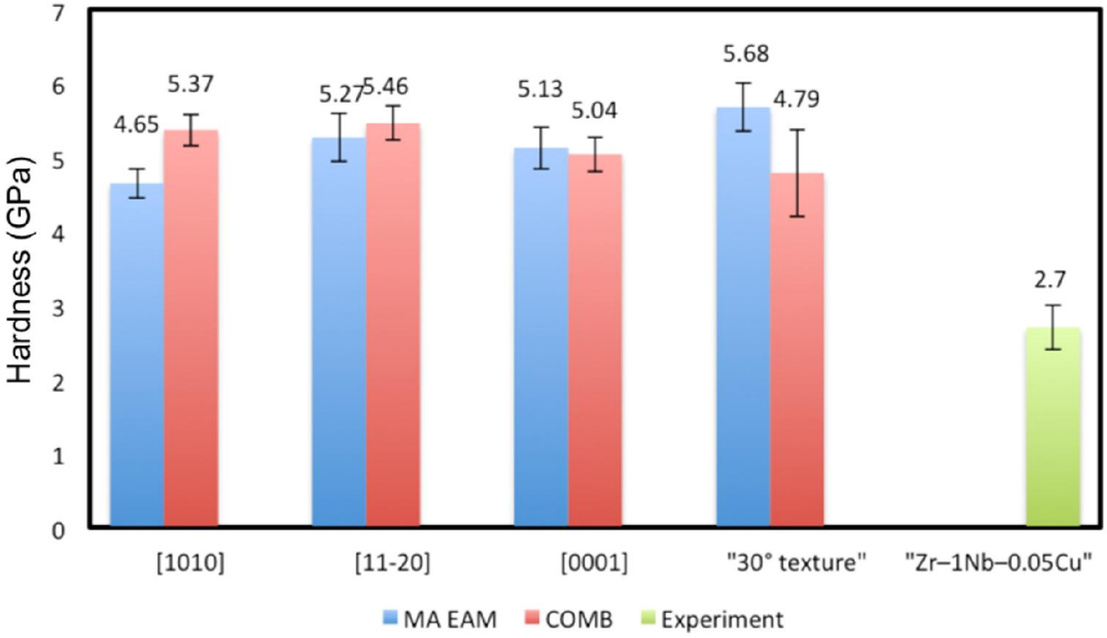

Figure 4-11. Hardness of four orientations using MA EAM and COMB potential. The experiment value is from reference [169].

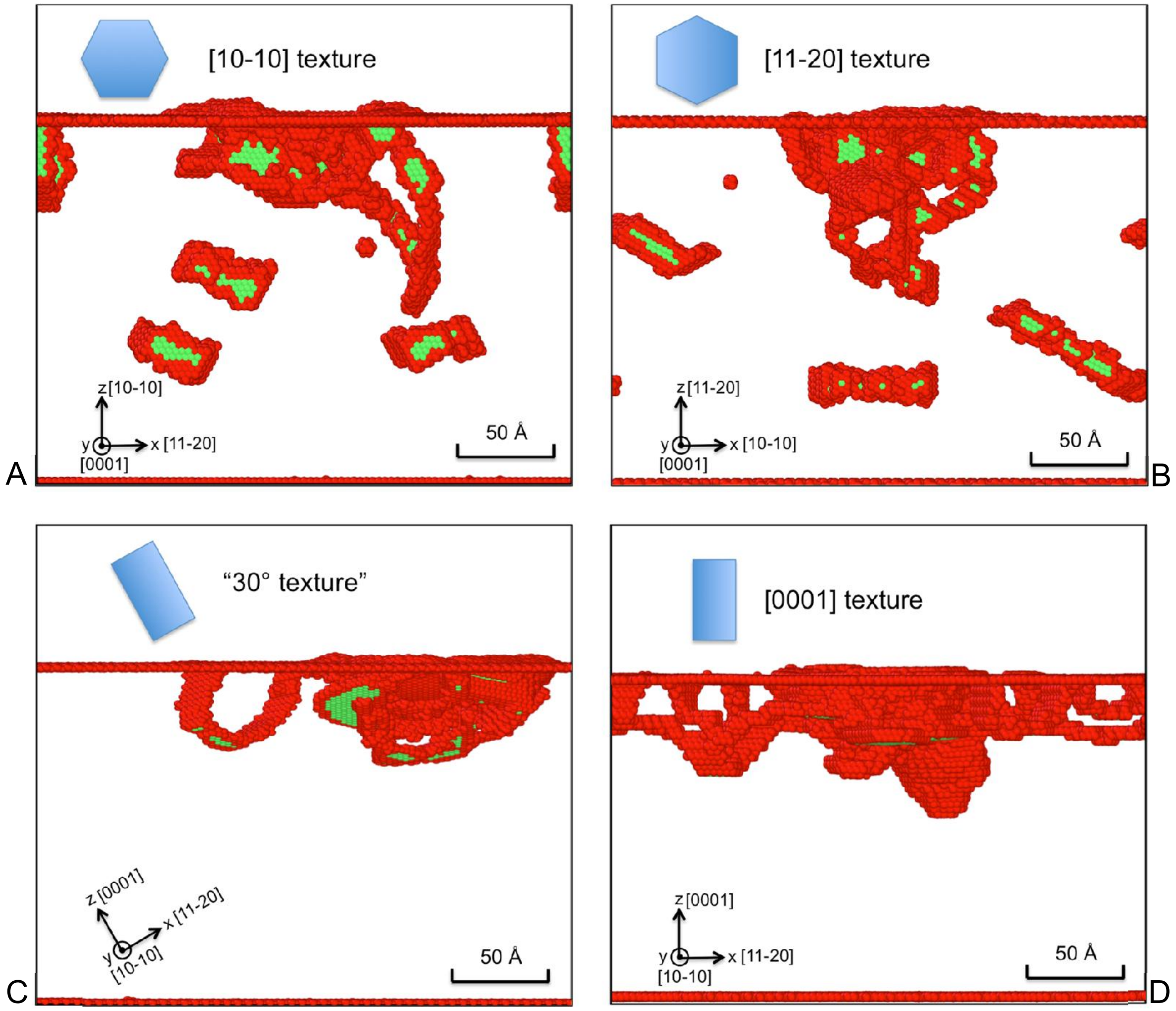

Figure 4-12. CNA analysis of Zr indentation at around 26 Å indentation depth using MA EAM. A) $[10\bar{1}0]$orientation. B) $[11\bar{2}0]$ orientation. C) 30° orientation along c-axis. D) $[0001]$ orientation. Red atoms represent the disordered atoms. Green atoms represent the atoms in fcc environment. The atoms in hcp environment are not shown.

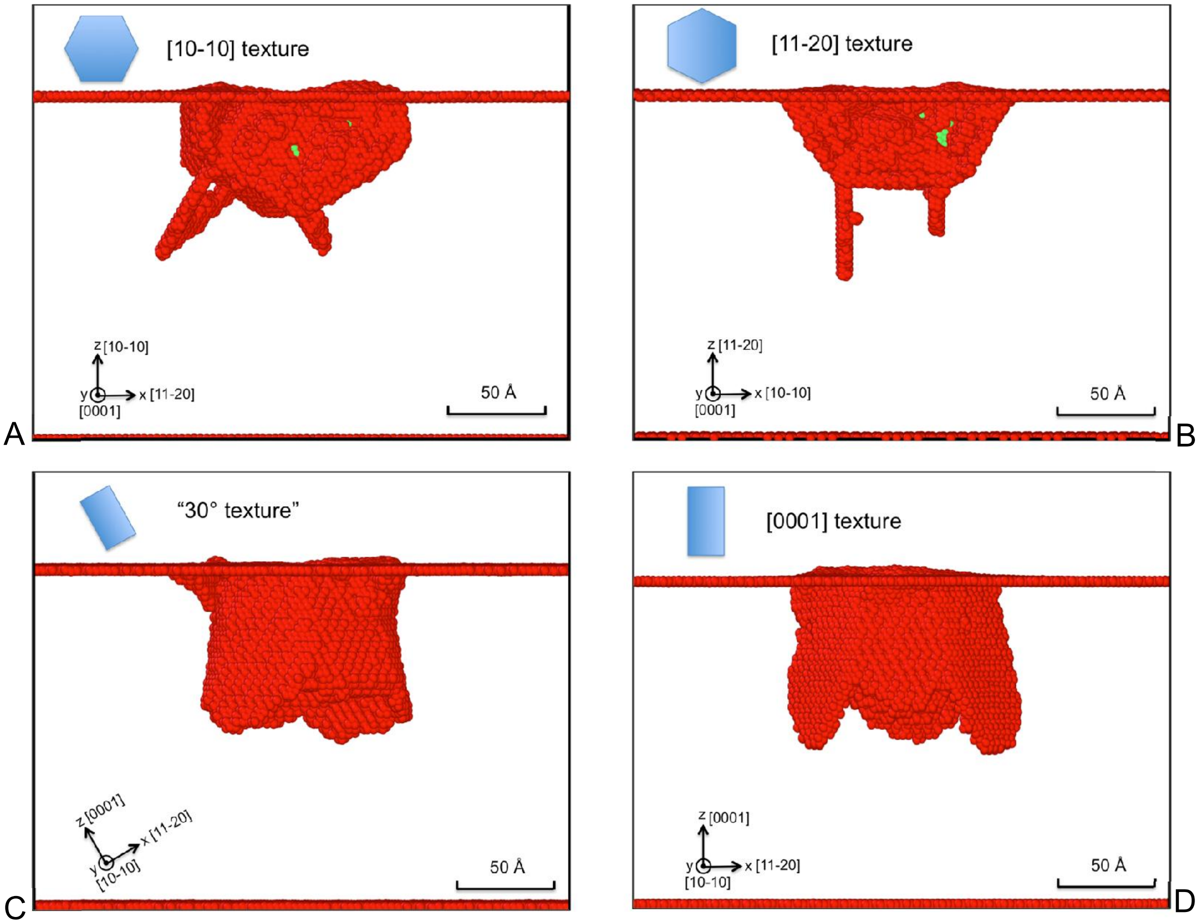

Figure 4-13. CNA analysis of Zr indentation at around 26Å indentation depth using the COMB potential. A) $[10\bar{1}0]$ orientation. B) $[11\bar{2}0]$orientation. C) 30° orientation along c-axis. D) $[0001]$ orientation.

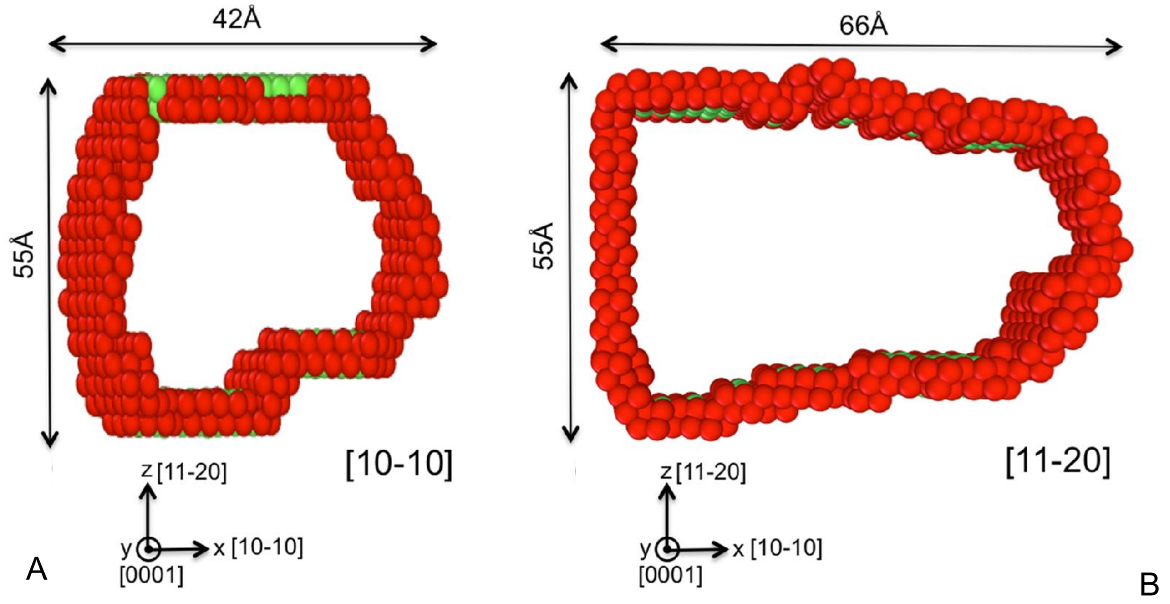

Figure 4-14. Atomic structures of dislocation loop formed during indentation simulation using MA EAM potential. A) $[10\bar{1}0]$. B) $[11\bar{2}0]$.

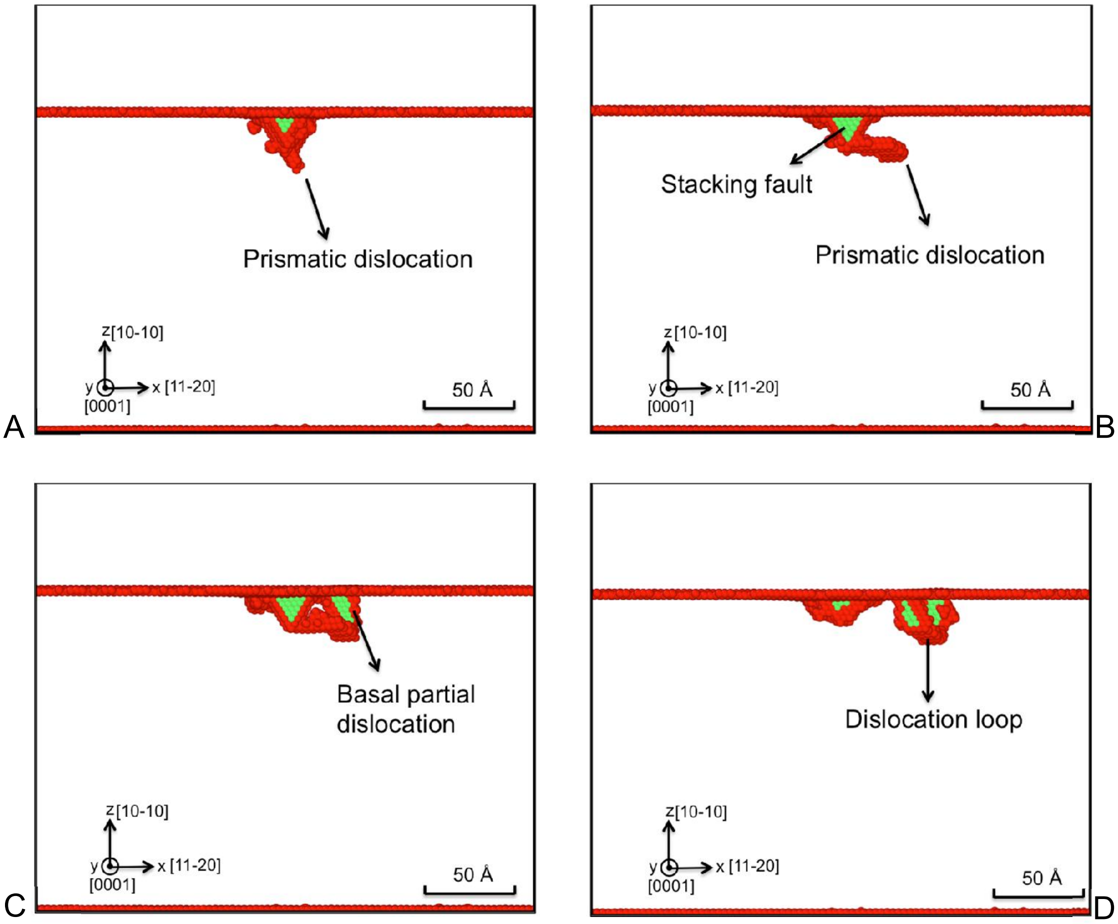

Figure 4-15. Initial stage of dislocation behaviors for MA EAM potential in $[10\bar{1}0]$ orientation.

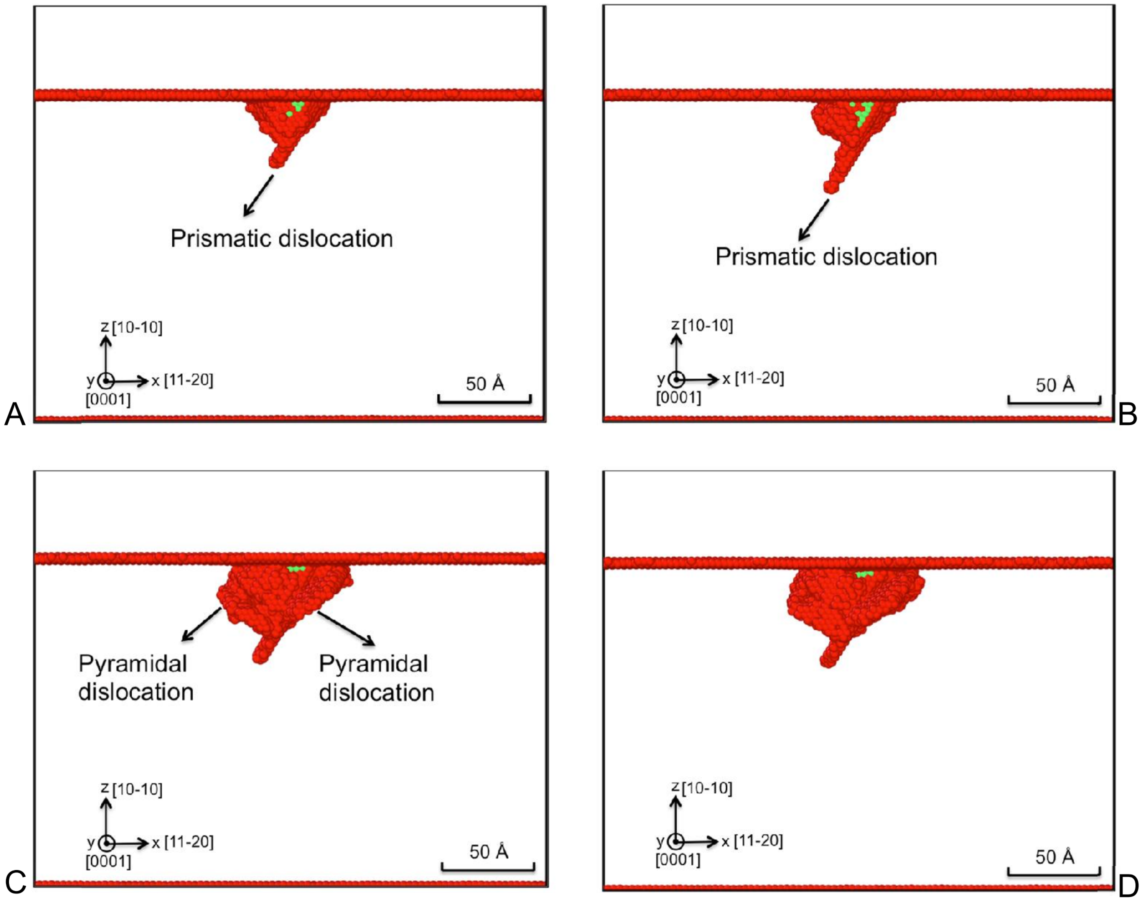

Figure 4-16. Initial stage of dislocation behaviors for COMB potential in $[10\bar{1}0]$ orientation.

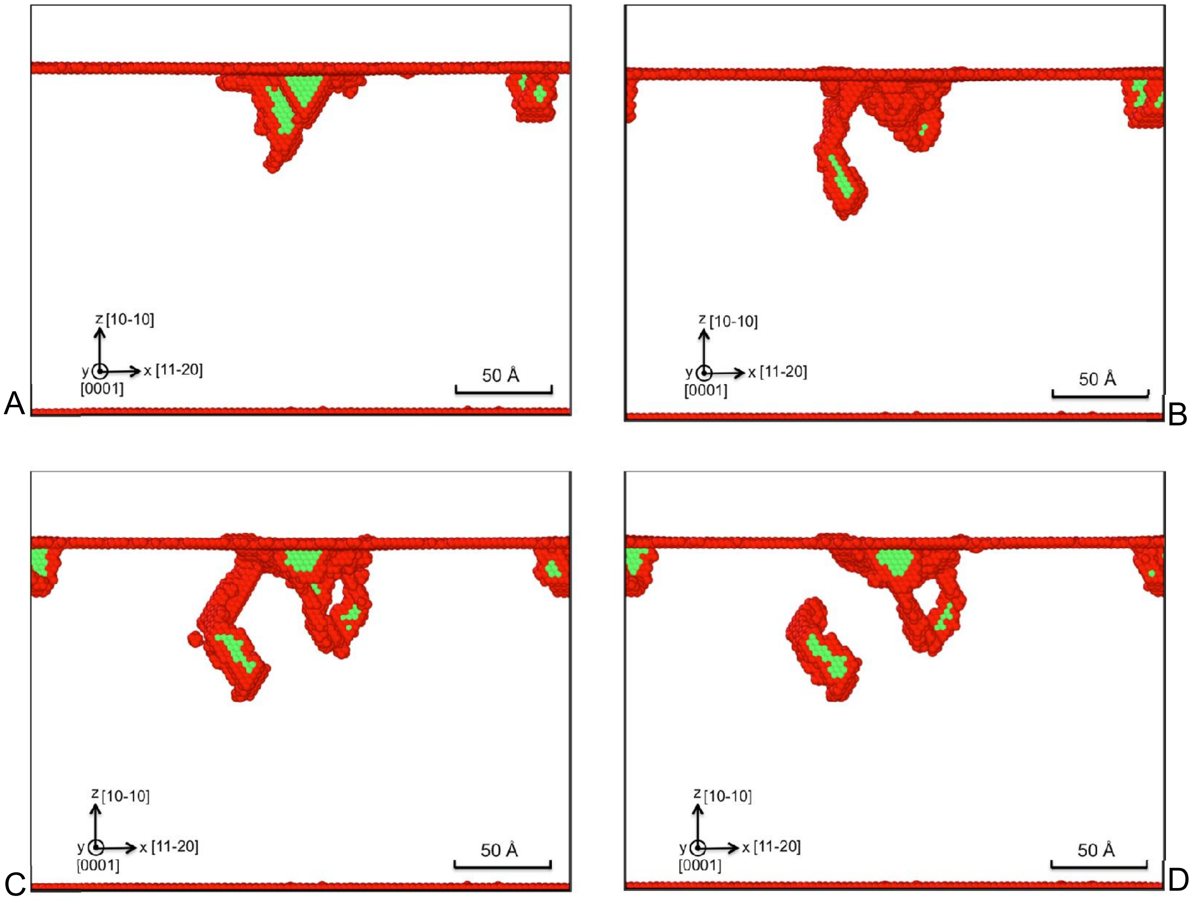

Figure 4-17. Formation of dislocation loop that glides into the bulk of MA EAM potential in the $[10\bar{1}0]$ orientation.

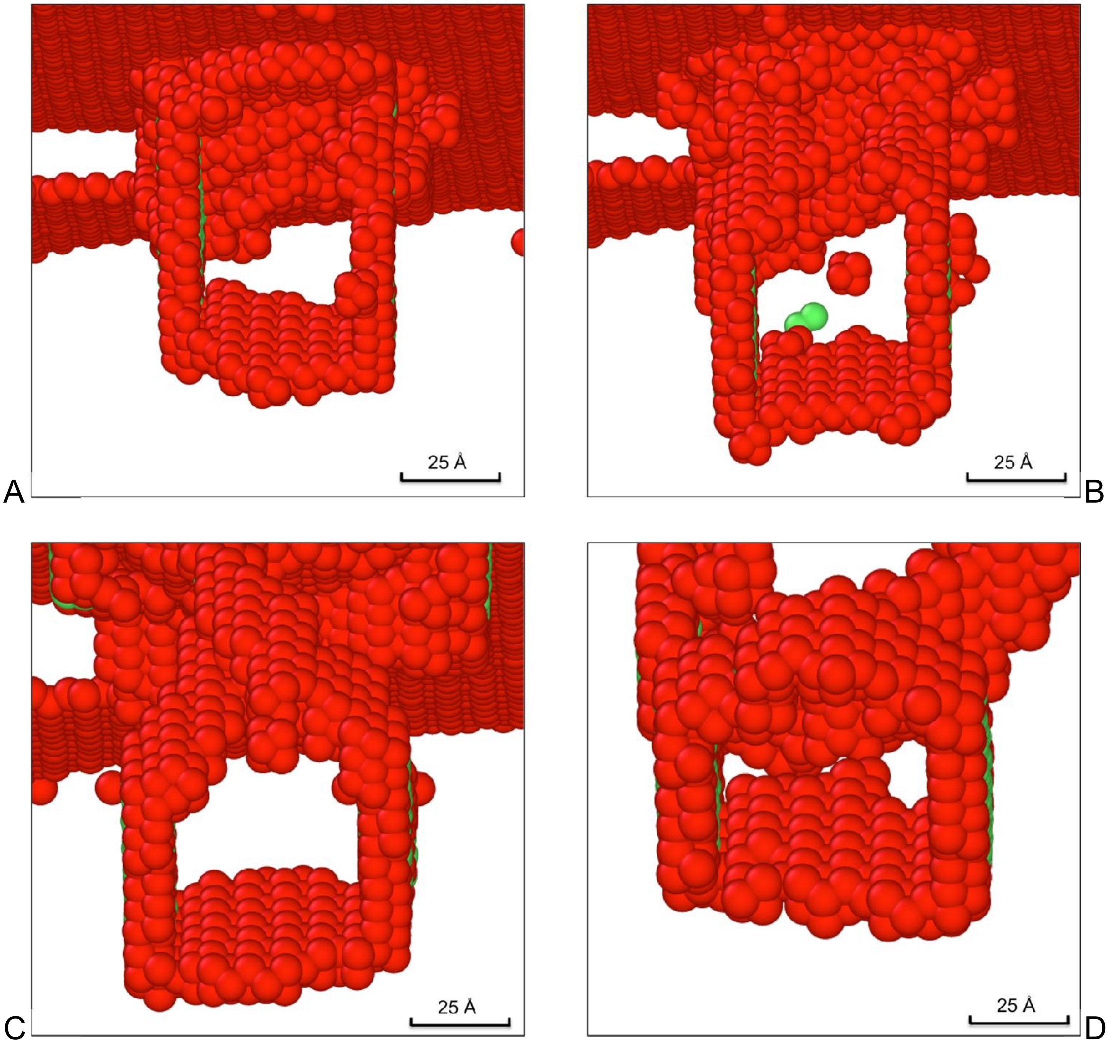

Figure 4-18. Dislocation loop formation process of MA EAM potential in $[10\bar{1}0]$ orientation.

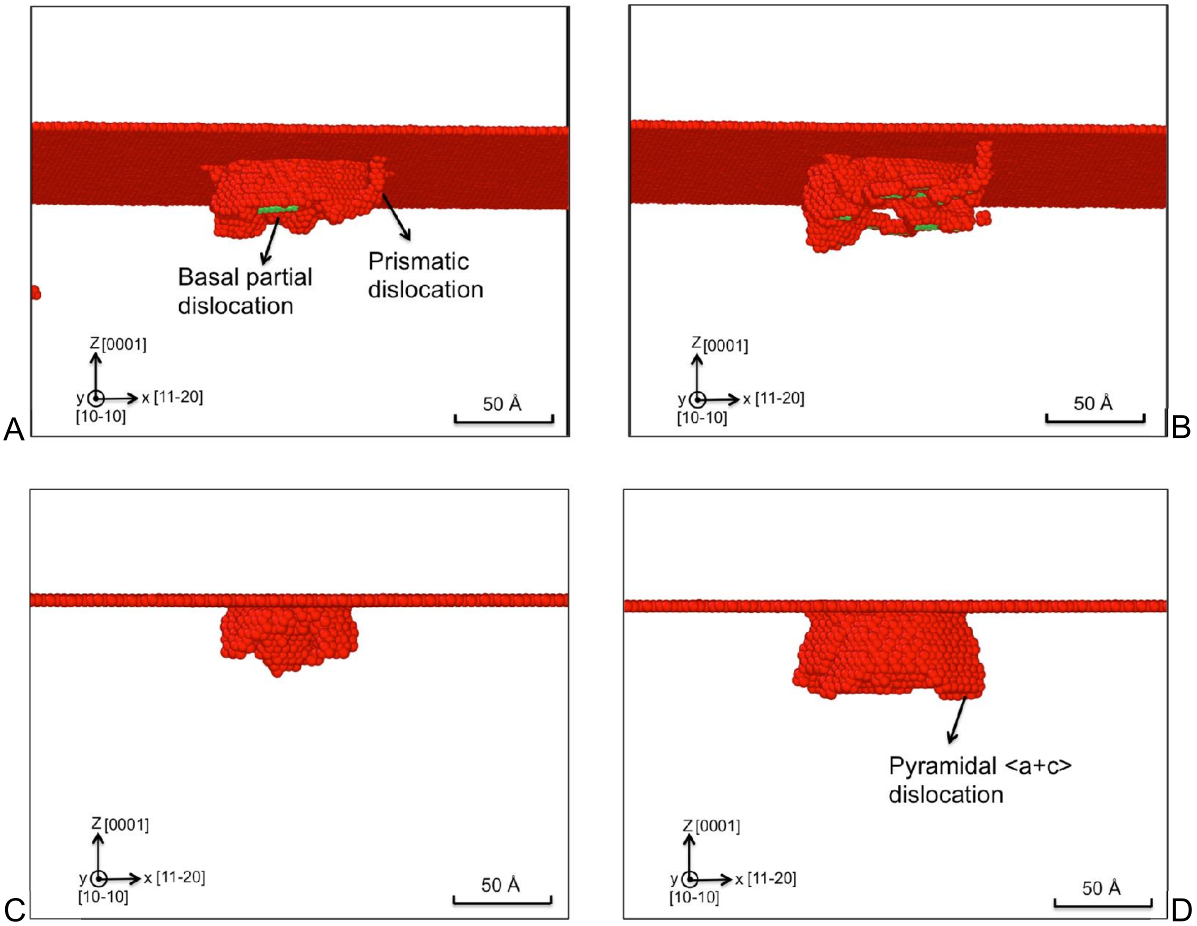

Figure 4-19. Microstructure evolution of $[0001]$ orientation during nanoindentation. A) and B) MA EAM. C) and D) COMB.

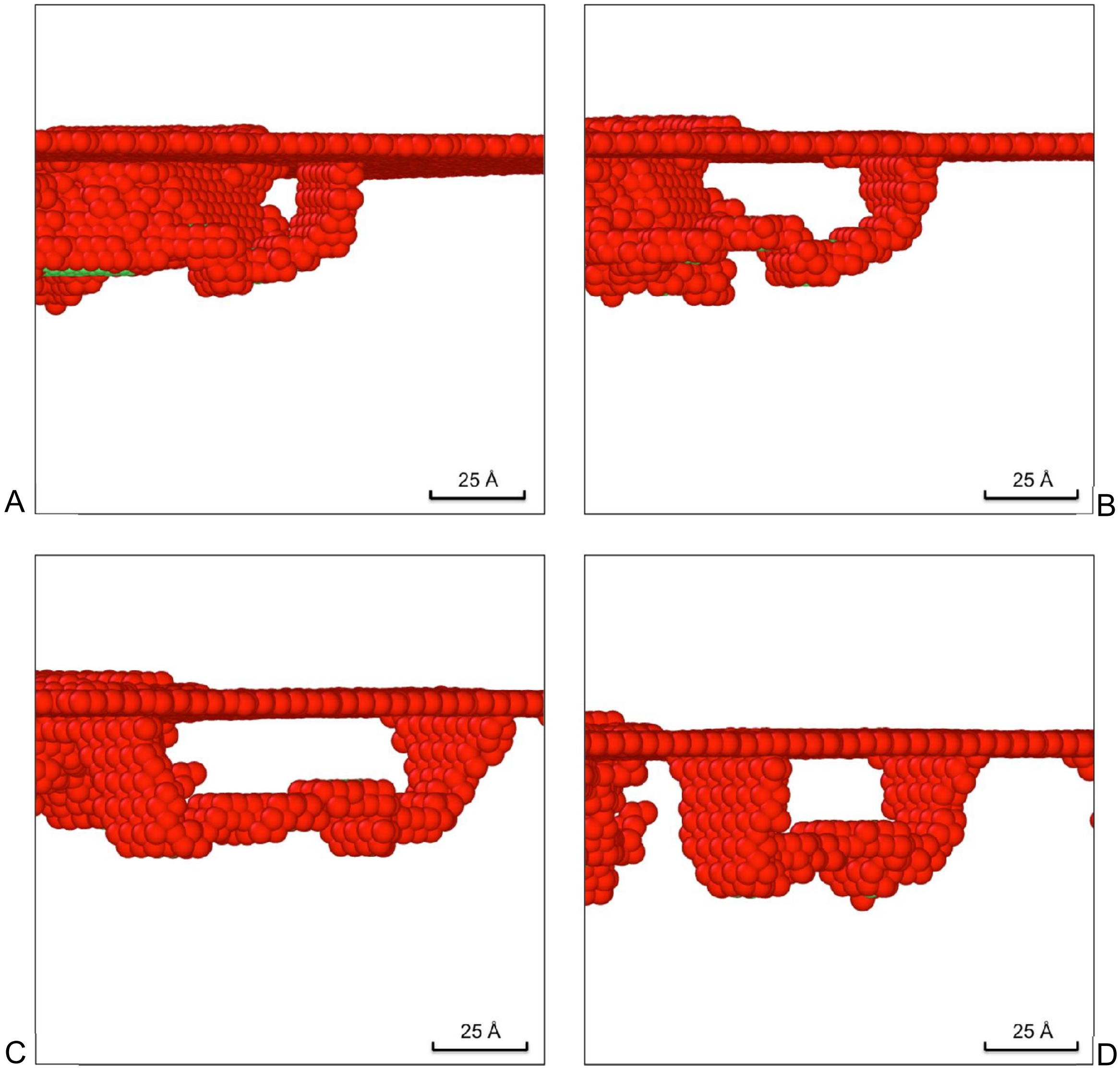

Figure 4-20. Details of dislocation loop formation in $[0001]$ orientation for MA EAM.

CHAPTER 5
NANOINDENTATION OF ZRO_2 BY MOLECULAR DYNAMICS SIMULATION

Motivation to study ZrO_2

One of the major products of the corrosion process of the zirconium clad inside the nuclear reactor is zirconia. The corrosion process of the cladding is discussed in the oxidation of zirconium section of Chapter 2. The properties of the corrosion product zirconia are discussed in the zirconia system section of Chapter 2. Since the mechanical integrity of the cladding is essential, it is important to understand its properties under high stress. In previous chapters we have elucidated the mechanical response of Zr under tension [150] and under nanoindentation (to understand hardness) [172]. It is also important to understand the effects of oxidation on the mechanical integrity of the clad. Therefore in this chapter, we analyze nanoindentation simulations of zirconia; in a follow-up chapter we will build on the study of Zr and this chapter to examine nanoindentation of a zirconia film on a zirconium substrate. In addition to its presence as a surface layer on clad, zirconia itself is also used as a ceramic biomaterial [173, 174], dental material [175], as a reinforced component in composite materials [176], a fuel cell electrolyte [177, 178], and as a thermal barrier coating [179]; in each of these applications its mechanical properties are important. In many of the above cases, the cubic zirconia is stabilized by another element, such as Y. But basic properties still come from the pure zirconia. So studying the pure zirconia will set the foundations to study all the above applications.

The empirical potential using COMB [180] formalism introduced in the interatomic section of Chapter 2 is capable of describing Zr-O-H system [71]. The details of ZrO_2 COMB potential are discussed in the following section.

COMB Potential of ZrO_2

In this nanoindentation simulation work, the third-generation charge-optimized many-body (COMB) potential is used to describe the Zr-O-H system [71, 132]; the potential developed by Noordhoek et al. [71] can describe zirconium, zirconia, zirconium hydride, and oxygen, hydrogen and water interacting with zirconium. The details of the COMB formalism and other examples of its applications are described in Chapter 2, and even more fully elsewhere [104, 180]. The development of a potential for such a wide range of materials inevitably requires some compromises with regards to any specific system. One of the compromises made in developing this COMB potential is that the ground state structure of ZrO_2 is the cubic fluorite phase.

In addition to the COMB potential, there are many other potentials for ZrO_2 in the literature [181-187]. Six interatomic potentials based on Buckingham potential form for yittria-stablized zirconia (YSZ) were assessed by Yin et al. [188]. For example, the Schelling potential, using Buckingham type short-ranged potential and a Coulomb electrostatics term, can describe both the cubic and tetragonal phases; this potential was also able to describe yttria-stablized zirconia (YSZ) [181]. However the Buckingham potential is a fixed charge potential and thus cannot describe zirconium or oxygen separately. The ReaxFF formalism, a variable charge reactive potential, has been parameterized for YSZ to study the oxygen ion transport [183]. The relative energies of a few phases agrees well with the quantum mechanics results. However the ReaxFF potential does not currently include the monoclinic phase and ZrH_x system. And the ability to describe the deformation behaviors is unknown.

In summary, the COMB potential is capable of describing many of the key properties of the Zr-O-H system [71, 132], albeit with less than ideal materials fidelity. The current parameterization of the COMB potential can only describe the cubic fluorite phase; while this is a clear limitation, the observed presence of the cubic fluorite on the Zr surface by electron diffraction [68-71] indicates that it can provide valuable information of such systems. Therefore, COMB will be used to study the mechanical properties of ZrO_2.

Here we only summarize the key properties of the potential with regards to representation of the c-ZrO_2; other properties are described elsewhere [71]. The elastic constants except for C_{44}, bulk modulus and shear modulus match well with DFT [189] results as shown in Table 5-1 [71]. Of the point defect formation energies listed in Table 5-2, the O vacancy, Zr vacancy and Zr interstitial formation energies predicted by COMB potential are higher than the DFT calculations, while that of the O interstitial is underestimated significantly comparing to DFT [71]. Due to the presence of the high stress concentration in nanoindentation simulation, the above discrepancy of the defect formation energy will not significantly influence the deformation outcomes. As in the Zr nanoindentation study of chapter 4 [172], the reduced modulus along [110] and [100] have been calculated, 370 GPa for [110] orientation and 468 GPa for [100] orientation. The reason for choosing the [110] and [100] orientations is given in the orientation section below.

Simulation Setup

Nanoindentation MD simulations of cubic zirconia were performed using LAMMPS [158]. The simulation set up is the same as that of the Zr nanoindentation simulations discussed in Chapter 4. The simulated system consists of 3 regions; from top to bottom: an active region, a thermostat region and a fixed region. The force exerted by the spherical indenter is applied to the active region, which is achieved by using the “fix indent” fix style in LAMMPS. The description of the applied force can be found in Equations 4-1 and 4-2. The details of the simulated system are shown in Figure 5-1.

Orientation

Both the [110] and [100] orientations of cubic zirconia have been observed in oxidized Zr by electron diffraction [68-71]; thus, these are chosen for our simulation study. The comparison of the [110] and [100] orientations will probe the anisotropy of ZrO_2. In addition, our simulation results can then be compared with those of the indentation experiments on [110] and [100] orientations of YSZ [190]. The (110) plane is the charge neutral plane as shown in Figure 5-2A. The structure in the [100] direction consists of alternating planes of Zr and O and thus has a dipole moment normal to the surface. Charged planes can be expected to reconstruct [191, 192]. For example, for (001) of rock-salt structure, the octopolar reconstruction can considerably lower the energy and reduce the surface stress [191]. In order to minimize the charged surface effect the top and bottom surface (100) plane are reconstructed by hand. First the top and bottom surfaces are set to be Zr planes. As a result, there is an extra Zr plane in the system. Then the atoms in the face center position of the top and bottom Zr planes are removed. Thus, after this modification, the (100) surface has a pyramid shape with (110) charge neutral plane facets and the ZrO_2 stoichiometry is conserved, as shown in Figure 5-2A.

Before nanoindentation, the two surface systems are fully relaxed under NPT condition. For the charge neutral (110) plane, the surface structure after relaxation is shown in Figure 5-2B. The surface oxygen layer splits into two oxygen layers. The Zr atoms stay at their lattice sites after relaxation. The charge of the surface Zr atoms is less positive than that of the Zr atoms in the bulk; and the charge of oxygen atoms at the surface becomes less negative. For the reconstructed (100) charged plane, the Zr and oxygen atoms at the surface leave their original position to form a relatively low energy configuration. The charge of Zr atoms at the surface becomes less positive compared to those in the bulk. And the charge of O atoms at the surface becomes less negative compared to those in the bulk.

Effect of Indentation Speed and Temperature

The possible effects of indentation speed and temperature are addressed first. Because it involves charge equilibration, the COMB potential is more computationally demanding than standard fixed-charge empirical potentials. Choosing the appropriate indentation speed that can both give physically reasonable results and minimize the computational time is thus important. Nanoindentation MD simulations on $CaCO_3$ minerals using $10ms^{-1}$ and $30ms^{-1}$ generates almost the same load-displacement curve [193]. Indentation simulations at $10ms^{-1}$ and $50ms^{-1}$ are tested here; as shown in Figure 5-3 for the [110] orientation, the load-displacement curves almost overlap at 300K. Most importantly, the load drops related to the plastic deformation both happen at approximately the same displacement of 13 Å.

Examining the effect of temperature using an indentation speed of $50ms^{-1}$, the load-displacement curves almost overlap with each other for 300K, 800K and 2000K especially before the first load drop. There is a small amount of elastic softening as the temperature increases; however, the load drops related to the plastic deformation takes place at an indentation of 13 Å for all temperatures.

The results indicate that the effects of temperature and indentation speed on the indentation simulation results are not that significant. In subsequent simulations, we thus use an indentation speed of $50ms^{-1}$ to minimize computing time and a temperature of 300K to minimize thermal fluctuations.

Using Hertz Law to Rescale MD Simulation Data

Hertz continuum elastic contact analysis has been widely used to describe the elastic deformation behavior for spherical indenter. Here, the Hertz Law will be used to rescale the MD data to the time and length scale of nanoindentation experiment. Within Hertz theory, the load applied by the indenter, P, is given by [161, 162],

$$P = \frac{3}{4} E^* R^{\frac{1}{2}} h^{\frac{3}{2}} \tag{5-1}$$

where R is the radius of curvature of the indenter, h is the indentation depth, and E^* is the reduced modulus, defined as [161, 162],

$$E^* = \left\{\frac{1-v_s^2}{E_s} + \frac{1-v_i^2}{E_i}\right\}^{-1} \tag{5-2}$$

where E_s and v_s are Young's modulus and Poisson's ratio of the sample and E_i and v_o are Young's modulus and Poisson's ratio of the indenter. For the hard indenter $E=\infty$ and $\nu=0$.

According to Equation 5-2, the reduced modulus E^* is the only materials related property. So we consider E^* as a constant, independent of the indenter size and indentation depth. The relationship between loads from different nanoindentation tests using different indenter sizes (R_1 and R_2) and indentation depth under the same indentation speed can be expressed as

$$\frac{P_1}{P_2} = \sqrt{\frac{R_1}{R_2}} \left(\frac{h_1}{h_2}\right)^{\frac{3}{2}} \tag{5-3}$$

where P_1 and P_2 are the load responses, and h_1 and h_2 are the indentation depths at different scales. In our study, P_1 is at the nN scale, while R_1 and h_1 are at Å scale. For the experiments we compare with, P_2 is at μN scale, and R_2 and h_2 are hundreds of nms. Hertz law is first used to examine whether the simulation results show elastic behavior in the elastic regime. According to Hertz law the load P should have linear relationship with $h^{3/2}$. Furthermore, the simulation results are rescaled to compare with the experiments [190] according to Equation 5-3.

Elastic Deformation

At the beginning of the indentation test, the system deforms elastically. In the elastic region, the load vs $h^{3/2}$ curves are compared for the data from the simulation and the data calculated according to Hertz Law. As shown in Figure 5-4, the load vs $h^{3/2}$ curves obtained from the simulation are linear, which represents the elastic behavior. The reduced modulus calculated using the potential predicted elastic constant of [110] and [100] orientations are 370 GPa and 468 GPa. According to Equation 5-1, the slope of the load-displacement in the elastic region of the [100] orientation should be steeper than that of the [110] orientation. In the simulations, the slope of the [100] orientation is initially slightly steeper than that of the [110] orientation, which is consistent with the order predicted by the Hertz law. However the [100] orientation shows a softening with increasing load. The above difference can be caused by the system size effect observed in the Zr nanoindentation simulation discussed in chapter 4 [172].

Having established that the elastic part of the indentation displays Hertz Law, we can rescale the length scale of MD to compare with experimental results, obtained for much larger indenters (350nm) and indentation depth at nanometer scale. The rescaling is based on Equation 5-3. The rescaled results are compared to the nanoindentation experiments on yttria-stabilized zirconia with 10%mole of yttria [190]. According to an experimental study of yttria-stabilized zirconia with mole% of yttria ranging from 11% to

18%, the Young's and shear moduli decrease as the mole% of yttria increases, while the anisotropy factor increases as the mole% of yttria increases [194].

As shown in Figure 5-5, the rescaled load-displacement curves from the MD simulations match quite well with those from the indentation experiments on single crystal YSZ. The simulation results match better with the experiments for [110] orientation. For [100] orientation, the simulation results agree well with the experiment for low loads prior to the softening discussed above.

The YSZ indentation experiments show that the slope of load-displacement of [100] orientation is steeper than that of [110] orientation, which is consistent with MD results and Hertz Law prediction. The difference between the load-displacement of [110] and [100] orientations in our simulation is smaller than that in the experiments, which can be caused by the increased anisotropy factor due to the yttria doping [194].

Plastic Deformation

The first load drop typically represents the initiation of the plastic deformation. As shown in Figure 5-6, the first load drop for the [110] orientation takes place at ~13 Å indentation depth, while for [100] orientation, the first load drop is at ~10 Å. After rescaling, the first load drop should be at ~10nm for [100] orientation and ~13nm for [110] orientation. The earlier yield for [100] orientation simulation agrees reasonably well with the indentation experiments on YSZ, which the first load drop for [100] and [110] orientations at 14nm and 22 nm respectively [190]. The simulated yield strength of the [110] orientation (~800nN) is twice as much as that of the [100] orientation (~400nN). This is also in consistent with the experimental results [190] which the yield strength of the [110] and [100] orientations are ~500μN and ~250μN respectively.

The deformed atomic structures at an indentation depth of 25Å are shown in Figure 5-7. The atomic pileups represented by the uncoordinated atoms in Figure 5-7 are seen in both [110] and [001] orientations. It is obvious that the shapes of the deformed regions are very different for the two orientations. The origin of this difference resides in the anisotropy and the limited slip systems of ZrO_2. For the [110] orientation, as we can see from the side view (001) plane, Figure 5-7A, and from the side view (110) plane, Figure 5-7C, that the boundary between the deformed and the un-deformed regions lie along the <110> direction. The boundary between the deformed region and un-deformed region in the [100] orientation is also along the <110> direction as shown in Figure 5-7B. This preference for deformation along the <110> direction during nanoindentation is consistent with <110> being the dominant slip direction for the ZrO_2 system. As introduced in the simulation analysis tool section in chapter 2, the Dislocation Extraction Algorithm (DXA) can be used to capture dislocation structures. First, the DXA is applied to the deformed structure with O atoms being removed so that the Zr can be treated as an fcc sublattice. No dislocation structures are captured by the DXA. By contrast indentation simulations of fluorite-structured CaF_2 did show the generation of dislocations as the first plastic event took place [195].

As the DXA is unable to capture any dislocations in the deformed structure, more detailed analysis of evolution of the atomic structure is necessary in order to understand how the structure transforms around the first load drop at the atomic level. First, the volume change during indentation at different places in the pile up region of [110] orientation is analyzed. A few tetrahedra defined in Figure 5-8 are chosen from different deformed regions to study the volume change. In the pile up region, the volume of the system decreases significantly at the load drops in the load-displacement curve. As shown in Figure 5-8, the volume of the tetrahedron in the blue circle region shows no significant change through the indentation process. The volume of the tetrahedron in the purple region starts to decrease significantly at an indentation depth of ~14 Å, which corresponds to the first load drop in the load-displacement curve. Furthermore, starting at ~18 Å indentation depth, the volume of the tetrahedron in the red circle region shows significant decreases, which correspond to the second load drop in the load-displacement curve. The volume of the tetrahedron in the green circle region starts to decrease at ~16 Å. That is, the region close to the indenter deforms first, then the further region deforms subsequently. Although no dislocation lines are captured in the deformed structure, the significant volume decreases proves that the load drop is caused by some structural changes.

Next, we analyze the evolution of the atomic structure of [110] orientation at the load drop. We first examine representative (100) and (110) planes in the [110] orientation to see how the system deforms. We pick out one (110) plane and one (100) plane inside the regions that deform during the nanoindentation. For the (100) planes shown in Figures 5-9(a) and (b), the atomic position in the deformed area only change slightly along [100] direction although there is force applied along [100] direction by the indenter. For the (110) plane shown in Figures 5-9(c) and (d), the atomic plane deforms significantly along the [110] direction. For the spherical indenter used here, the forces applied along [110] (x-axis) and [100] (y-axis) are equal. By the comparison shown in Figure 5-9, we can conclude that the structure prefers to deform along [110] direction with [100] direction being the hard direction.

The Zr atoms on ZrO_2 lie on an fcc lattice and thus have 12 Zr neighbors. Close to indenter, there are a number of 13-coordinated Zr atoms, shown as red atoms in Figure 5-7. The structural change in the above 13-coordinated atoms region is shown in Figure 5-10. The xz-(100) plane deforms along [100] to transform to a closed packed plane with 13 coordination numbers during indentation. The distance between nearest neighbor is ~2.8 Å. The structure of xy-(100) plane stays unchanged during the indentation. So the highly deformed region can be regarded as a closed pack structure with AAA stacking sequence along y-<100> direction. The transformation of the O lattice is similar to the Zr as shown in Figure 5-11. On the xz-(100) plane, the O atoms squeeze along [110] direction. The O atoms also form a higher density structure.

The charge distribution of [110] and [100] orientation after nanoindentation simulation is shown in Figure 5-12. The pile up region and the boundaries between the deformed and un-deformed region can also be represented by the charge distribution. As we can see the charge of Zr atom becomes less negative in the deformed region; the charge of the O atoms become less negative.

Hardness

The hardness for the two orientations is calculated using the same method discussed in the hardness calculation method section of Chapter 4 [172]. Briefly, as shown in Figure 5-13, the hardness keeps increasing with indentation depth until the first load drop. After the first load drop, the hardness value stays relatively constant. We take as a representative hardness the average between the two dashed lines. The quoted error represents the standard deviation within the two red dotted lines region. The nanoindentation simulation yields a hardness value of 19.8±0.6 GPa for [110] orientation and 14.6±0.3 GPa for [100] orientation.

Our previous nanoindentation MD study on single crystal Zr with different orientations using COMB potential gave calculated hardness over the range from 3.5 GPa to 6 GPa. The comparison of load-displacement curve of [0001] Zr and [110] ZrO_2 is shown in Figure 5-14. The load response of ZrO_2 is much higher than that of Zr as we expected. Moreover, the plastic deformation happens much earlier for Zr than for ZrO_2 consistent with the stronger propensity of hcp metals to deformation than ionic materials.

Summary on ZrO_2

This work addresses the deformation process of cubic ZrO_2 in both [110] and [100] orientations. In the elastic deformation regime, the MD simulation results agree with the Hertz Law. After rescaling, the MD data is very comparable to the experiments. Furthermore, the anisotropy predicted by MD simulation is confirmed by the experiment and the classical theory. Yield behaviors are seen in both [110] and [100] orientations. The earlier yielding for [100] orientation is consistent with the experiment. All the above agreement with experiment proves the fidelity of this ZrO_2 potential. In the plastic deformation regime, the structural transformation at atomic level is analyzed. The reason for the absence of dislocation line structure is not clear. The analysis of the structural transformation indicates that the structure tends to deform along [110] direction. As the COMB potential is a variable charge potential, the charge evolution is also analyzed. When Zr and O atoms are at surface area or in the deformed region, both of their charge tends to decrease. This study on ZrO_2 builds the foundation to study the ZrO_2/Zr system.

Table 5-1. Comparison of cubic zirconia's properties obtained by experiment, DFT and COMB.

Property	Experiment [44, 196]	DFT [189]	COMB [71]
a_0 (Å)	5.0858	5.116	5.1247
C_{11} (GPa)	417	520	486
C_{12} (GPa)	82	93	94
C_{44} (GPa)	47	61	98
B (GPa)	194	235	228
G (GPa)	95	122	134

Table 5-2. Point defect formation energies predicted by DFT and COMB in cubic zirconia.

Point defect	DFT (cubic phase) [71, 197]	COMB (cubic phase) [71]
O vacancy (eV)	6.15	11.2
O interstitial (eV)	3.46	0.37
Zr vacancy (eV)	15.00	27.9
Zr interstitial (eV)	1.78	4.17

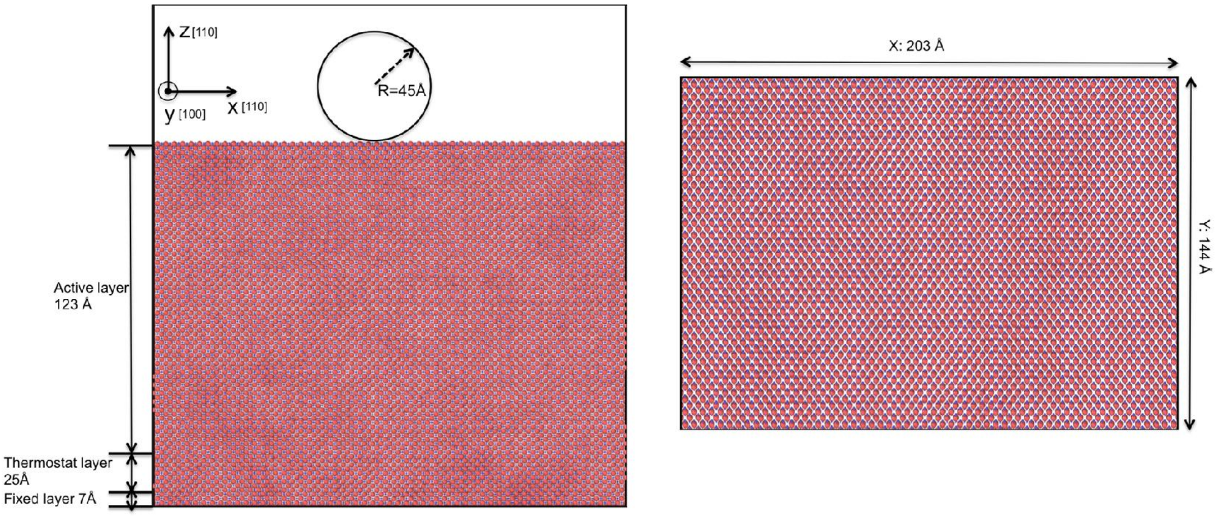

Figure 5-1. Details of the simulated [110] oriented ZrO_2 system.

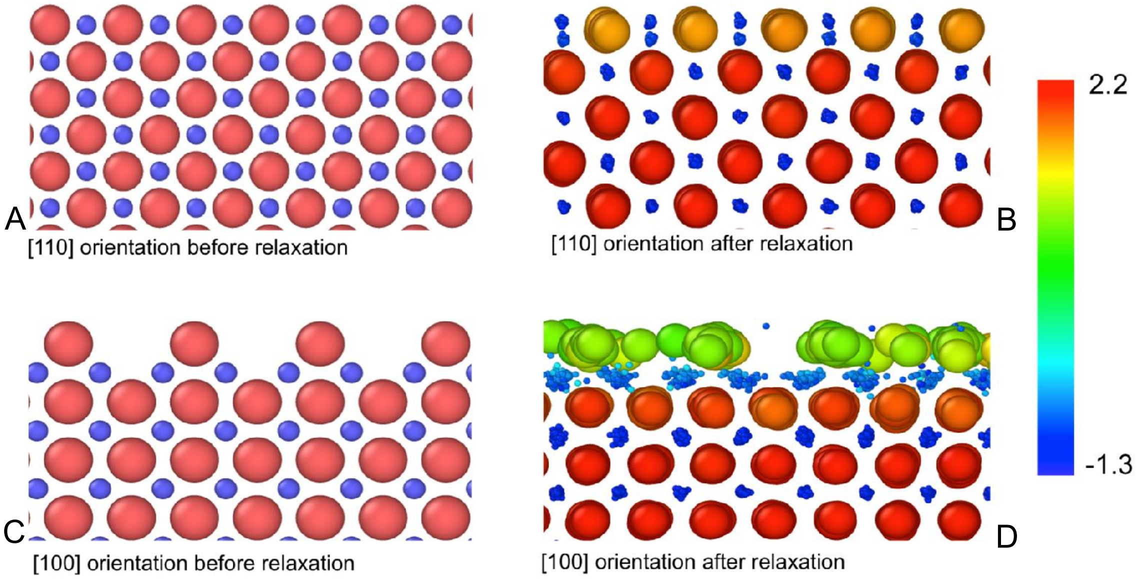

Figure 5-2. Side view of slice through the zirconia surface. A) [110] orientation before relaxation. B) [110] orientation after relaxation. C) Modified [100] orientation before relaxation. D) Modified [100] orientation after relaxation. a) and c) are color coded by atom type. Red atoms are Zr. Blue atoms are O. b) and d) are color coded by charge. For the (110) surface the Zr and O are in the same plane into the image. In the (100) surface the Zr and O are separated by a quarter of a lattice parameter into the image. For [100] orientation, the bottom of the system has been modified in the same way as the surface. The bottom has the same structure as the surface. Thus the stoichiometry has been preserved.

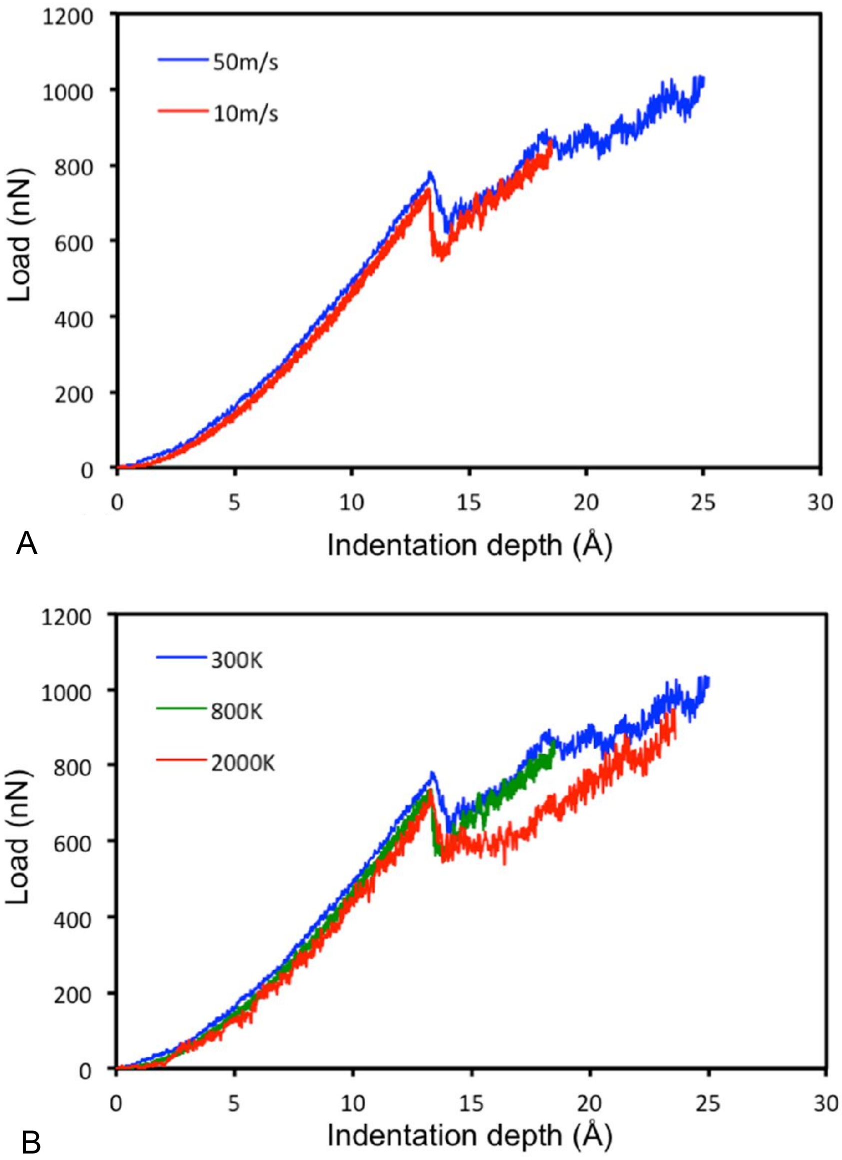

Figure 5-3. Load-displacement curve for [110] orientation using different indentation speed and under different temperatures. A) load-displacement curve for [110] orientation at indentation speeds 50ms^{-1} and 10ms^{-1} at 300K. B) load-displacement curve for [110] orientation at 300K, 800K and 2000K at 50ms^{-1} indentation speed.

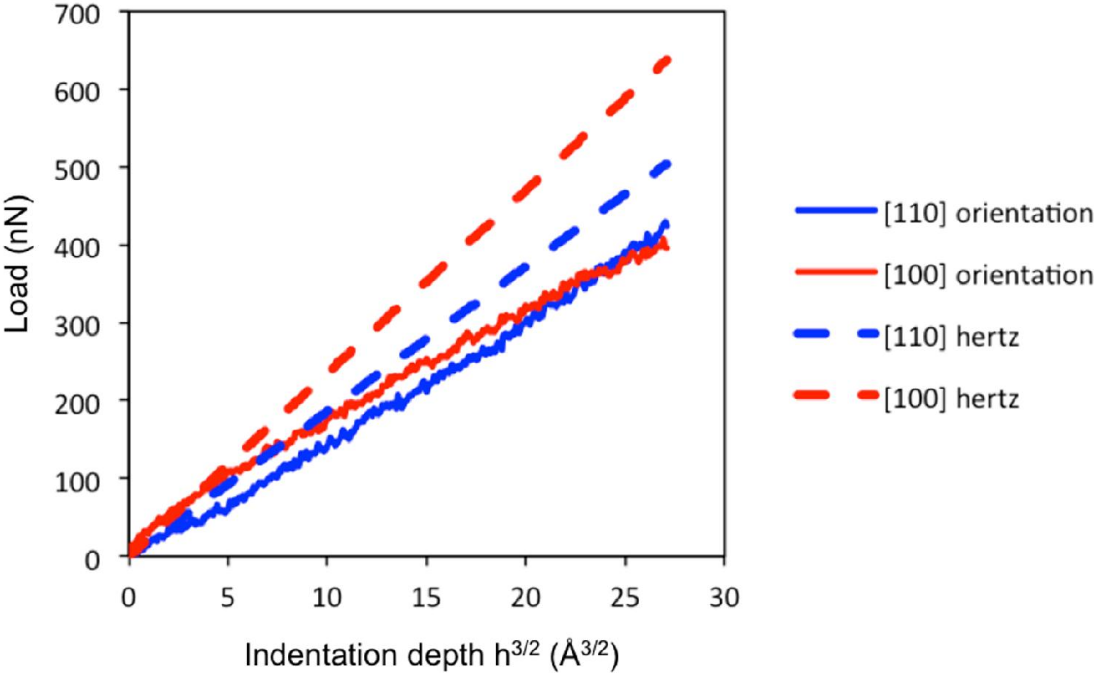

Figure 5-4. Load vs $h^{3/2}$ in the elastic region for [110] and [100] orientation obtained from both simulation and Hertz law.

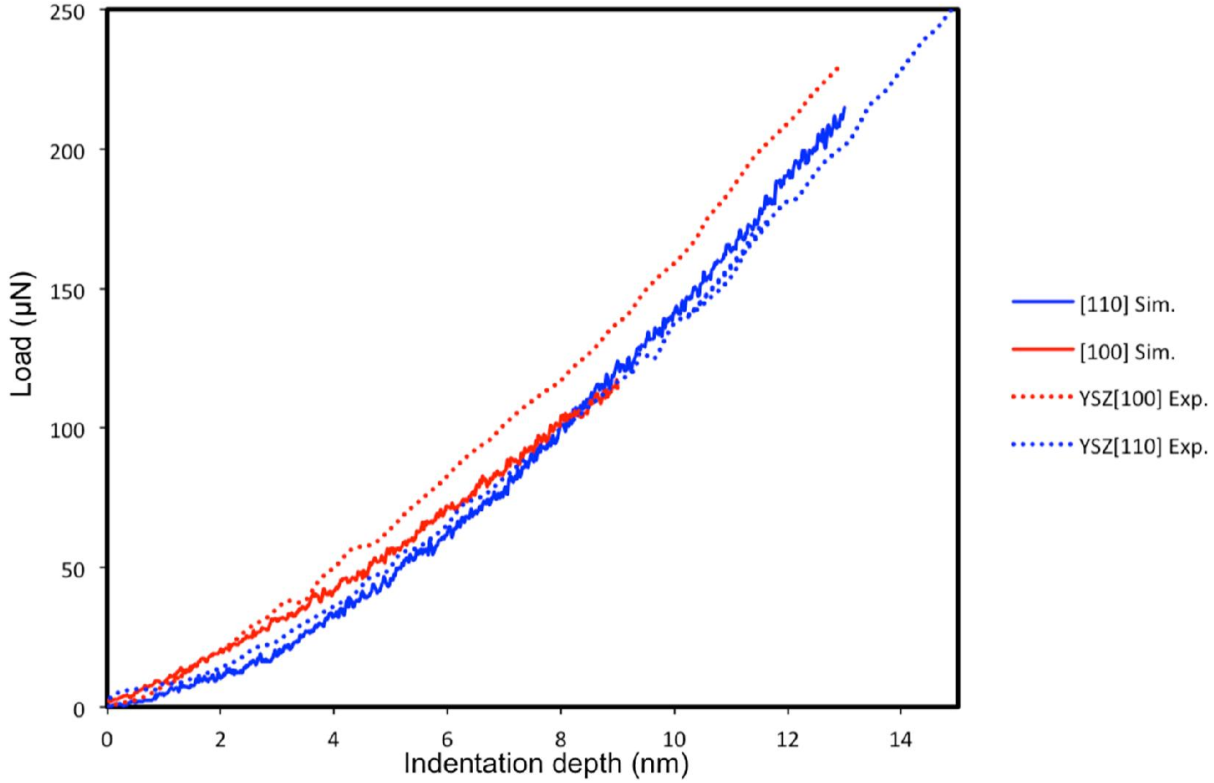

Figure 5-5. Load-displacement curve comparison between rescaled MD data and experimental data. The experimental data shown as YSZ [100] Exp. and YSZ [110] Exp. is obtained from reference [190]. [110] Sim. and [100] Sim. are the simulation results.

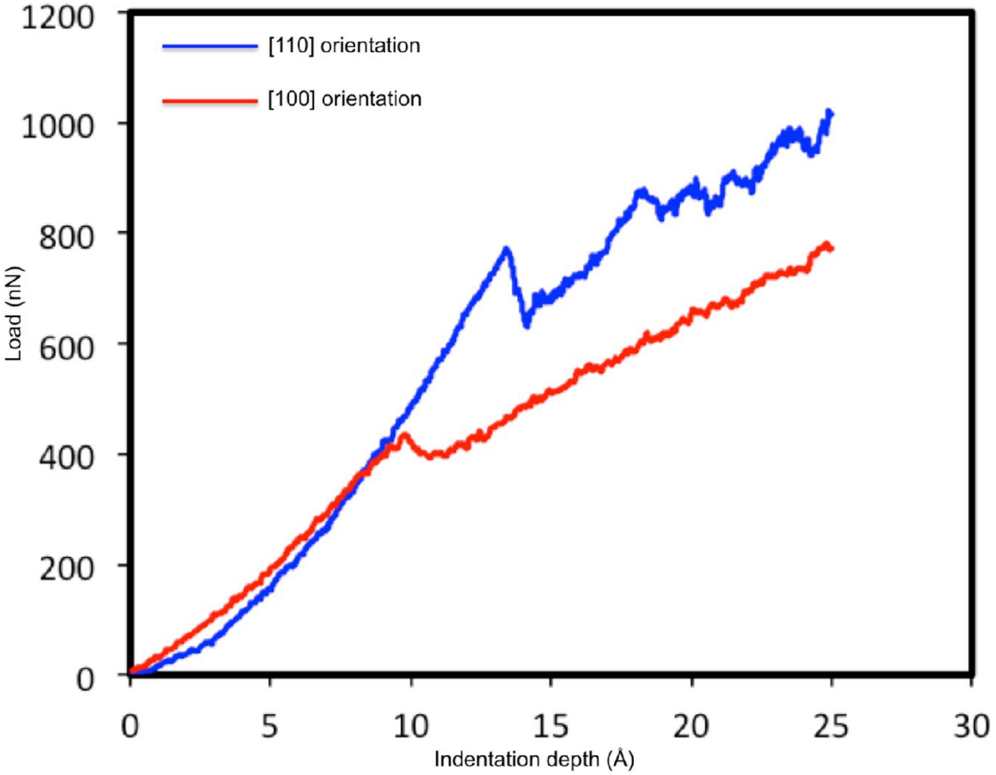

Figure 5-6. Load-displacement curves for [110] and [100] orientation under indentation at 300K for speed of $50ms^{-1}$.

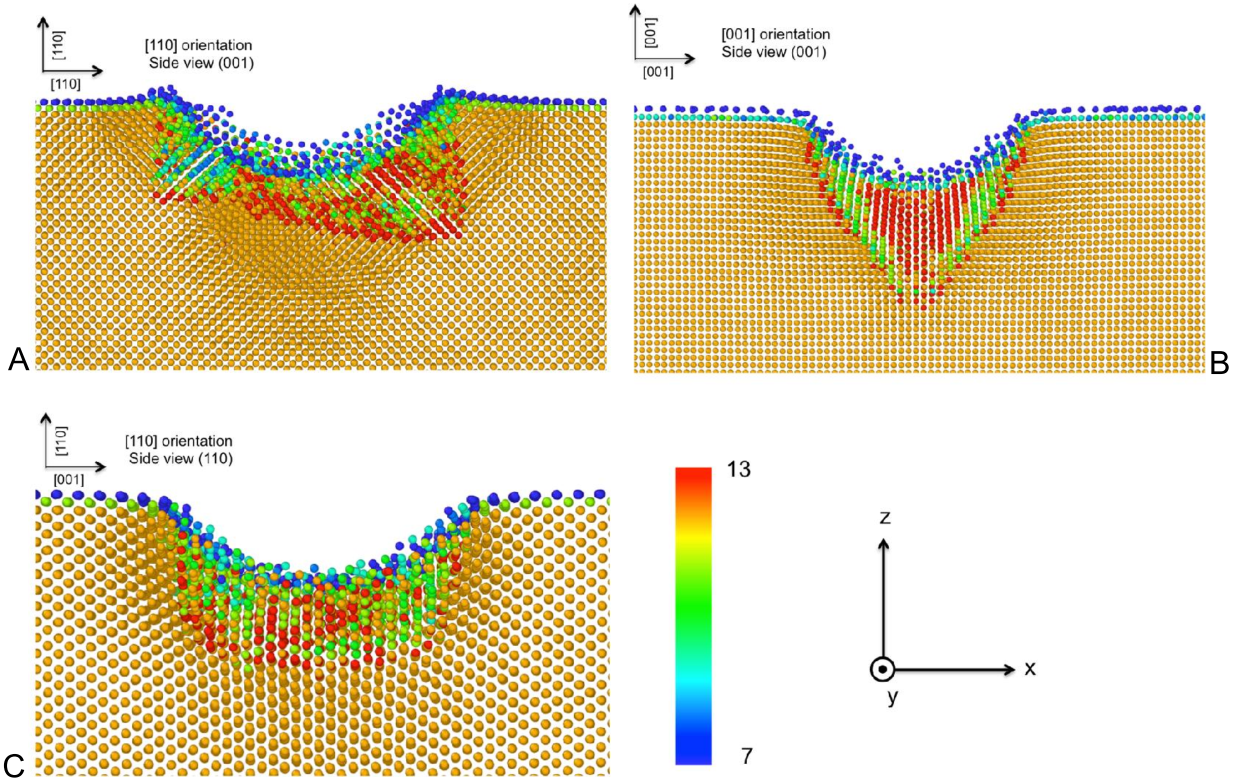

Figure 5-7. Side view of deformed structure of ZrO_2 at indentation depth of 25Å. A) [110] orientation side view (001) plane. B) [001] orientation side view (001) plane. C) [110] orientation. The color scheme represents the coordination number. Only Zr atoms are shown in the figure.

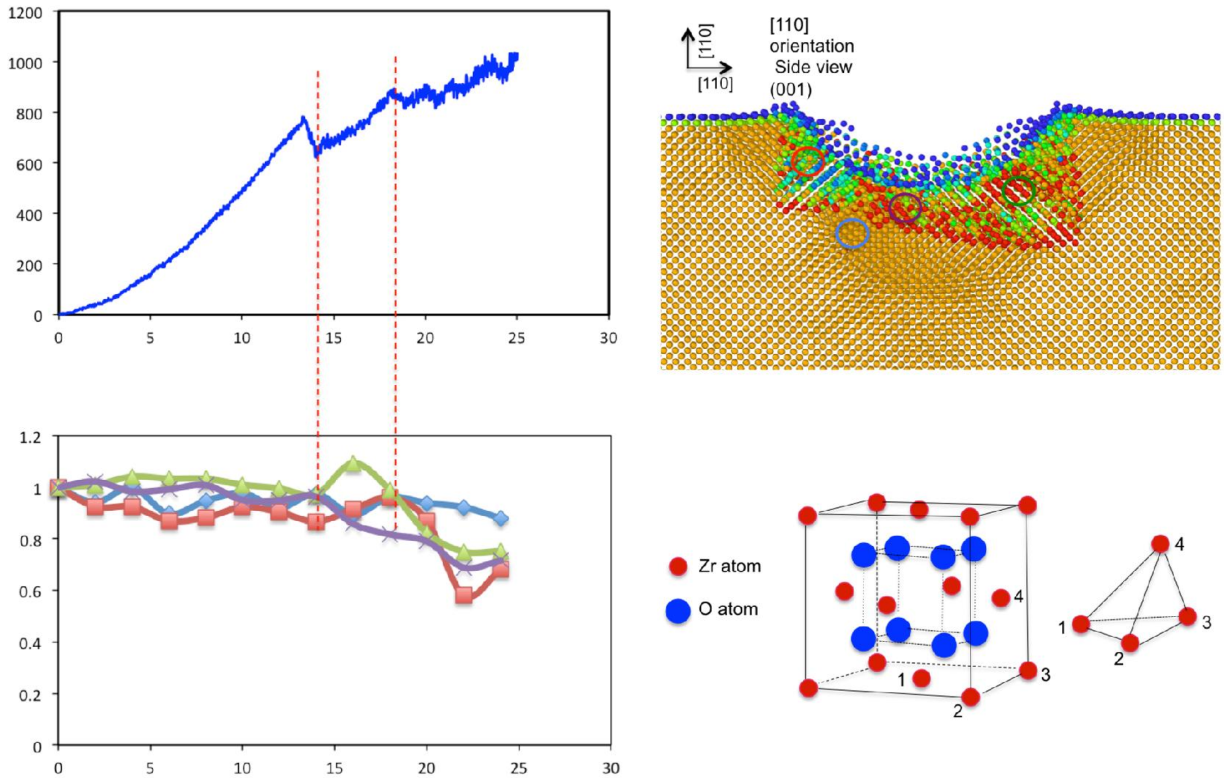

Figure 5-8. Volume change of a tetrahedron in the deformed area during nanoindentation simulation for [110] orientation. Atom 1, 2, 4 and 4 form the tetrahedron.

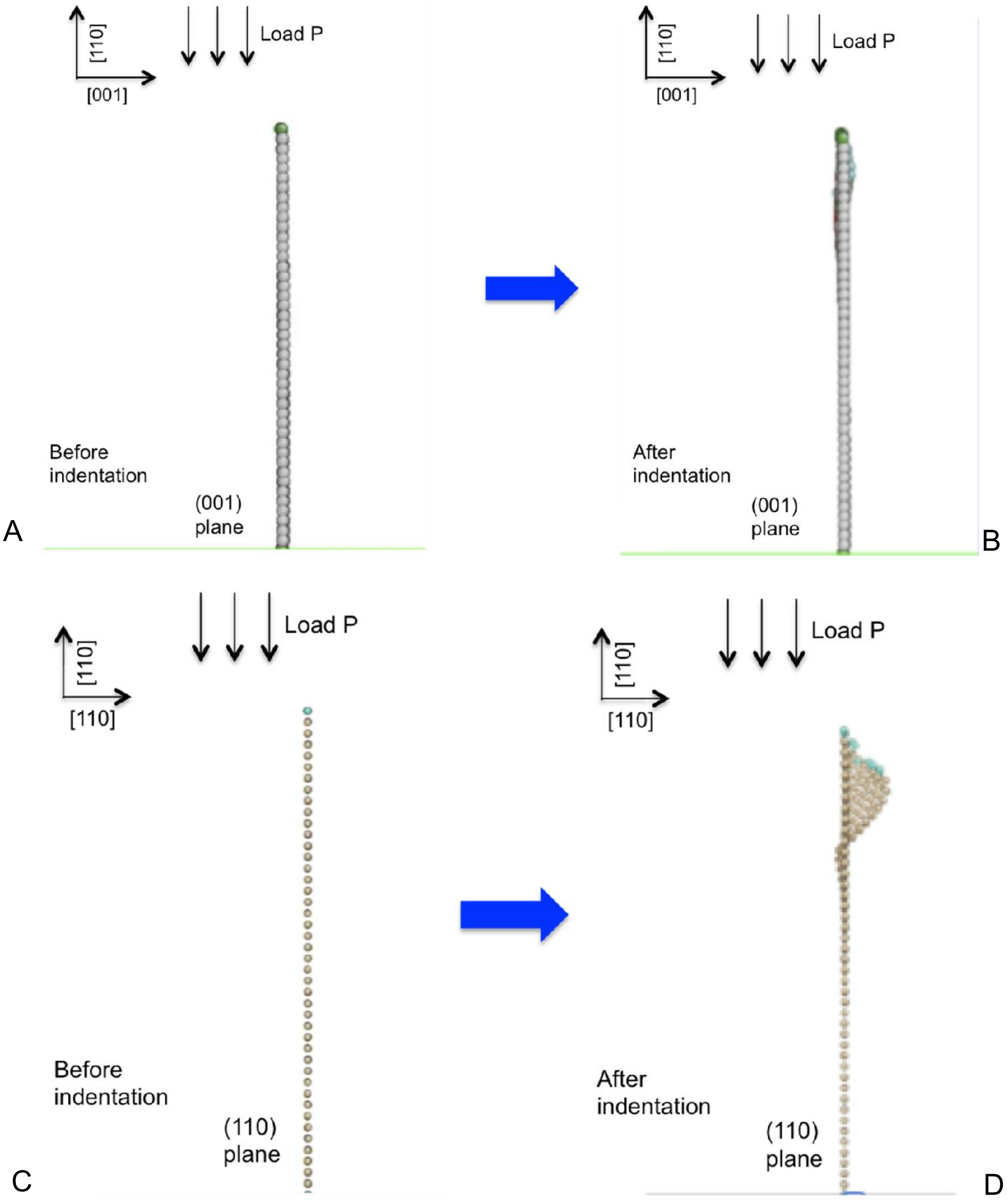

Figure 5-9. Analysis of indentation in [110] orientation. A) One (100) plane before nanoindentation simulation. B) The same (100) plane after nanoindentation simulation. C) One (110) plane before nanoindentation simulation. D) One (110) plane after nanoindentation simulation. Both planes lie under the indenter.

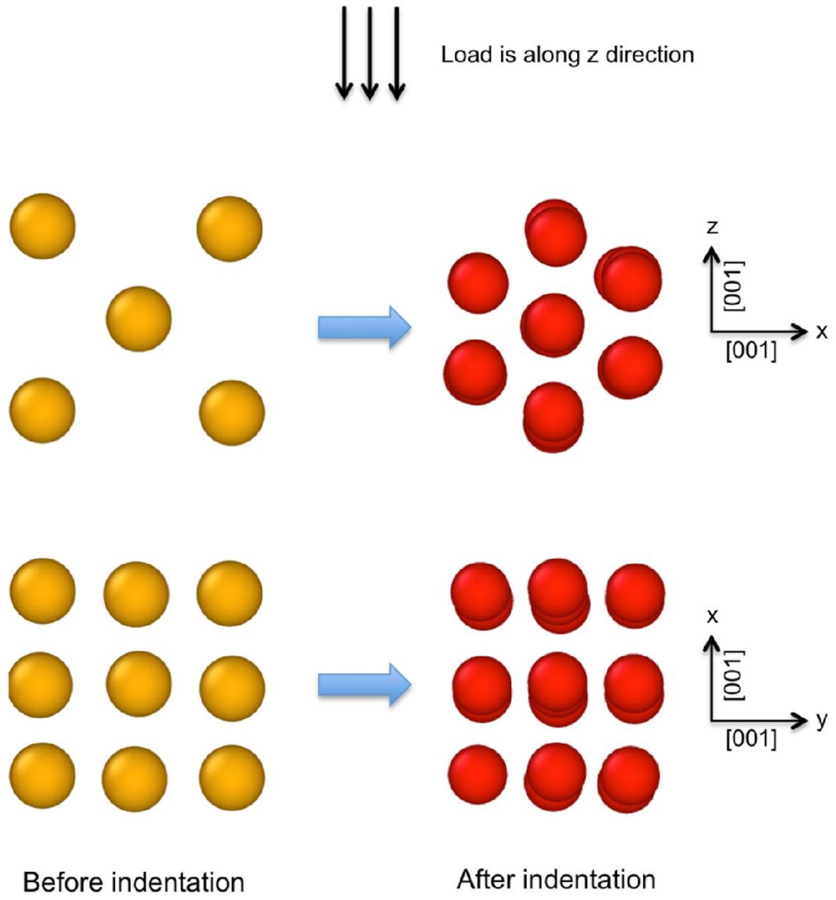

Figure 5-10. The transformation of highly deformed region with 13 coordination number in [100] orientation during indentation. Yellow atoms represent 12 coordination numbers. Red atoms represent 13 coordination numbers.

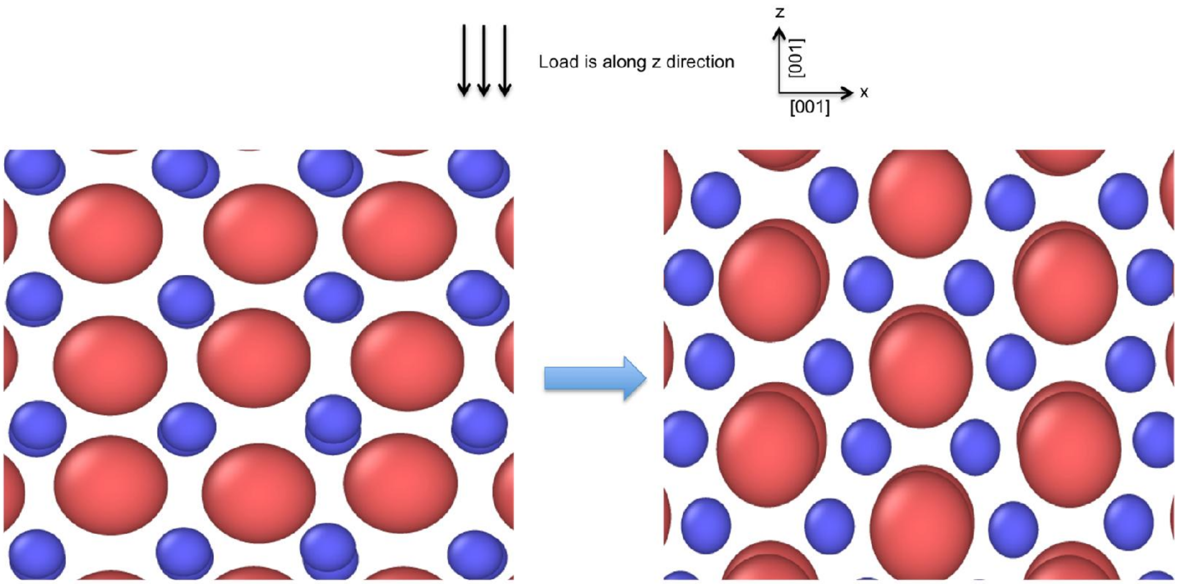

Before indentation

After indentation

Figure 5-11. The transformation of highly deformed region with both Zr and O atoms in [100] orientation. The atoms are color coded by atom type. Red atoms are Zr and blue atoms are O atoms.

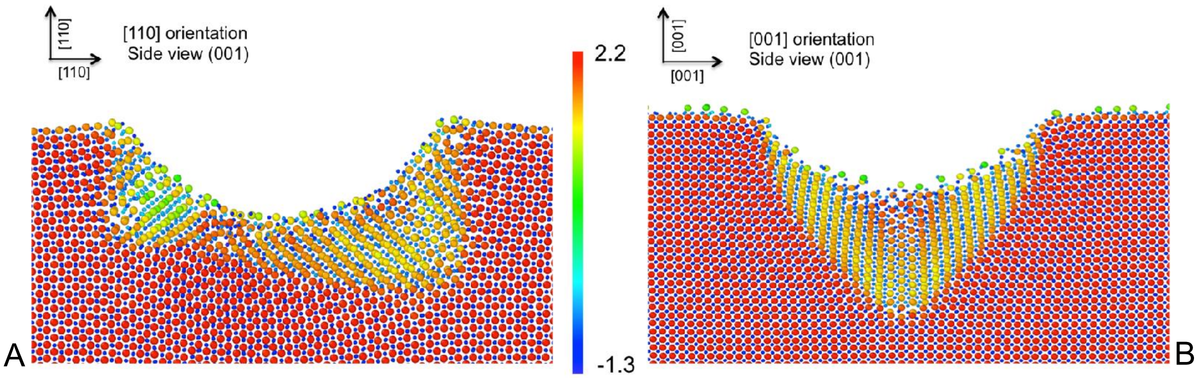

Figure 5-12. Charge profile in side view of deformed structure of ZrO_2 at indentation depth of 25Å. A) [110] orientation side view (001) plane. B) [001] orientation side view (001) plane. The atoms are color coded by charge.

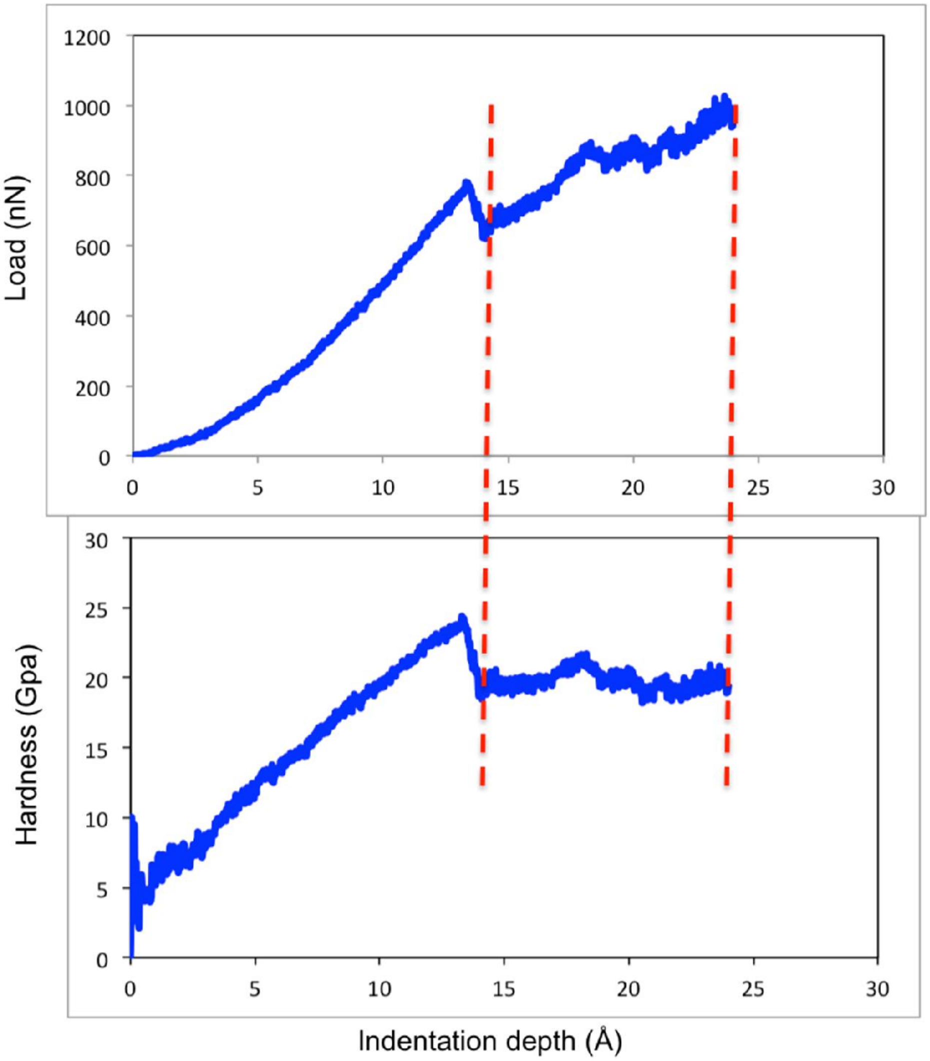

Figure 5-13. Hardness vs indentation depth for [110] orientation.

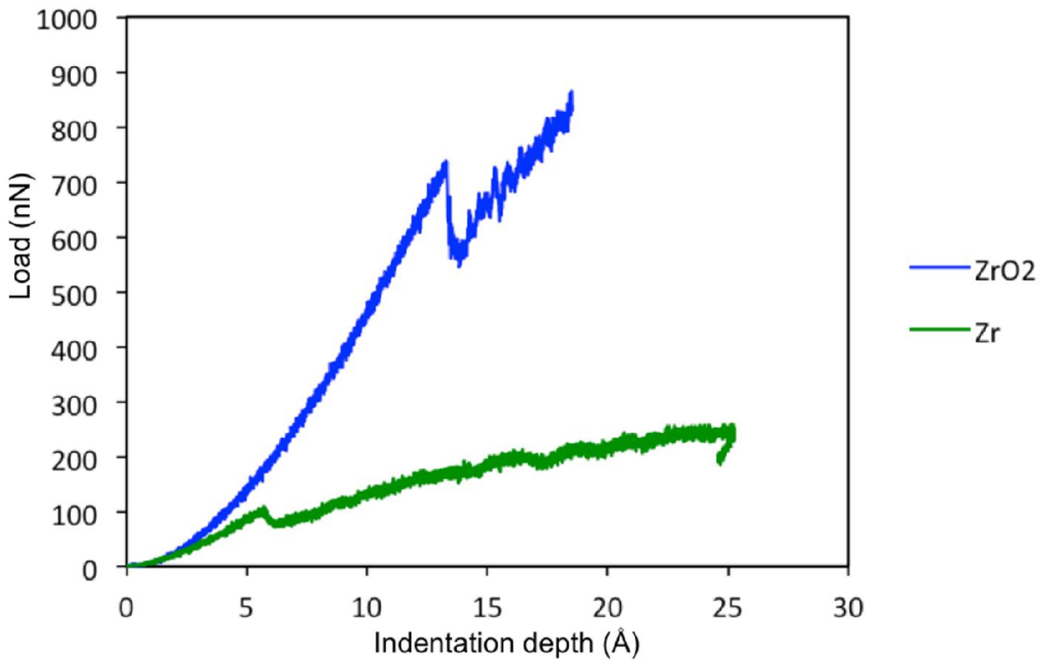

Figure 5-14. Load-displacement curve of [0001] Zr and [110] ZrO_2.

CHAPTER 6
NANOINDENTATION OF ZRO_2/ZR BY MOLECULAR DYNAMICS SIMULATION

Chapter 3 addressed the deformation behaviors of polycrystalline Zr. Nanoindentation simulations were performed on four orientations of single crystalline Zr and two orientations of single crystalline cubic ZrO_2 in Chapters 4 and 5 respectively. This understanding of the deformation behaviors of Zr and ZrO_2 constitutes a solid foundation to move on to the study of ZrO_2/Zr system; that is a thin ZrO_2 layer on top of a Zr substrate. In this chapter, the Zr and ZrO_2 interface is first studied by using COMB potential. Then the nanoindentation simulations of ZrO_2/Zr system are performed to study to deformation behaviors. Finally, the results from Zr, ZrO_2 and ZrO_2/Zr systems are compared.

Zirconia/zirconium Interface

As discussed in the oxidation of zirconium section of Chapter 2, a zirconium oxide layer forms during clad corrosion. The COMB potential can describe the Zr-O-H system. As discussed in Chapter 5, the ground state of ZrO_2 predicted by the COMB potential is cubic. The simulated metal/oxide system consists of [0001] orientation Zr and [110] orientation ZrO_2 as shown in Figure 6-1. Oxidation on Zr (0001) surface has been studied extensively [68, 198-203]. As discussed in the Orientation section of Chapter 5, the [110] orientation of ZrO_2 has been observed in oxidized Zr by electron diffraction [68-71]; (110) plane is a charge neutral plane that does not has a dipole moment normal to the surface plane. Discussed in the texture in zirconium section of Chapter 2, [0001] orientation is the main texture observed in Zircaloy [39]. So the Zr-[0001] orientation with ZrO_2-[100] orientation on top is chosen as the simulation system. A schematic of the simulated system is shown in Figure 6-1. In order to reduce the lattice mismatch between Zr and ZrO_2, the number of unit cells of Zr and ZrO_2 along x and y directions has been chosen such that total strain is less than 1% along x direction and less than 3% along y direction. The work of separation of Cu/ZrO_2 system calculated using DFT is 1.96 Jm^{-2} for one of the configurations of Cu-(001)/ZrO_2-(110) interface [204]. The work of adhesion of our simulated system is 2.31 Jm^{-2}, which is comparable to the above DFT results. The atomic structure of the system before and after relaxation is shown in Figure 6-2. The O atoms diffuse to the second layer of Zr substrate as shown in Figure 6-2B. The charge of the O atoms in the interface area becomes less negative. As shown in Figure 6-2C, the structure of three layers of Zr atoms in Zr substrate and two layers of Zr atoms in ZrO_2 at the interface changes. The charge of Zr in ZrO_2 becomes less positive at the interface while with the charge of Zr atoms in Zr substrate in the interface region becomes more positive. The oxygen density is shown in Figure 6-3 and the shear strain map at the interface is shown in Figure 6-4. The O atoms start to move around their perfect lattice sites during relaxation, which corresponds to the broadening of the O density peak in Figure 6-3. The first two peaks in Figure 6-3 at the ZrO_2 surface correspond to the splitting of the first O layer at the ZrO_2 surface, which is also seen at the surface of pure ZrO_2 after relaxation. The O density peaks start to decrease and broaden close to the interface. The O atoms diffuse across the interface to the second layer of the Zr metal substrate. After relaxation, a strain field exists at the interface, as shown in Figure 6-4. Two layers of ZrO_2 and three layers of Zr at the interface have been strained. The structures of the first layer of Zr, Figure 6-4B, and the first layer of ZrO_2, Figure 6-4C, are distorted, but do not transform to different structures. At the interface, the Zr substrate experiences higher shear strain than the ZrO_2 layer. The charge of Zr decreases from ZrO_2 to Zr across interface along with the charge of O decreases from ZrO_2 to Zr across interface as shown in Figure 6-5A. The above charge transfer at the interface result in the formation of a dipole moment at the interface seen in Figure 6-5B between 25 Å and 30 Å. In addition, the charge of Zr and O atoms decreases at the ZrO_2 surface seen in Figure 6-5A before 5 Å. A dipole moment forms within the ZrO_2 surface layer shown in Figure 6-5B before 2 Å. The total charge inside the ZrO_2 layer and Zr substrate is zero.

Simulation Setup

The nanoindentation simulation set up for ZrO_2/Zr system is the same as the set up for Zr and ZrO_2 systems introduced in Chapter 4 and Chapter 5. The simulation is performed at 300K with a $10ms^{-1}$ indentation speed. Common Neighbor Analysis [126, 127] and the Dislocation Extraction Algorithm (DXA) [123, 125] are used to analyze the deformed structures.

Load-displacement Curve and Hardness

The load-displacement curve and the hardness versus indentation depth are shown in Figure 6-6. In the load-displacement curve, no significant yielding is seen until 18 Å indentation depth where the load starts to decrease. The hardness first increases with the indentation depth. Then it becomes stable and fluctuates between 13 Å and 18 Å. After yielding at around 18 Å, the hardness starts to decrease. Unlike the case in Zr and ZrO_2 nanoindentation simulation seen in Figure 4-3 and Figure 5-13, the hardness first increases with the indentation depth and after certain indentation depth it becomes stable. As discussed in Chapter 4, hardness largely depends on the deformation behaviors. The above difference for ZrO_2/Zr might be explained by the later deformation analysis.

The comparison of load-displacement curve for Zr-(0001), ZrO_2-(110) and ZrO_2-(110)/Zr-(0001) is shown in Figure 6-7. It can be concluded from Figure 6-7 that the ZrO_2 is the hardest and Zr is softest, while the ZrO_2/Zr system resides in the middle. As a metal system, it is reasonable that the Zr system yields at the most shallow indentation depth, around 5 Å. However, the hardest ZrO_2 yields at around 13 Å, while the softer ZrO_2/Zr system yields at 18 Å. Based on the fact that the yield happens at 5 Å for pure Zr, the Zr substrate in ZrO_2/Zr system is expected to yield before 18 Å. It raises the questions as to at what depth the Zr substrate in ZrO_2/Zr system starts to yield and what activity causes the load drop at 18 Å indentation depth. The above questions are expected to be answered by the deformation analysis later.

Deformation Process during Nanoindentation Simulation

The deformed structure during nanoindentation simulation is shown in Figure 6-8. In Figure 6-8, the O atoms have been removed from the visualization. The Zr atoms are in an fcc environment in the ZrO_2 layer and in an hcp environment in the Zr substrate. So, CNA can be applied separately in Zr and ZrO_2 to identify fcc-like atoms, hcp-like atoms and disordered atoms. DXA can be used to extract dislocation lines. As discussed in Chapter 4, the DXA is not very successful of capturing the dislocations line in pure Zr COMB simulations. Thus, DXA will mainly be used here to capture the dislocation lines in ZrO_2. Dislocations start to nucleate in the Zr substrate at around 12 Å as shown in Figure 6-8A. The 12 Å indentation depth correspond to the b point in the load-displacement curve seen in Figure 6-6. It answers the question raised in the previous section that the Zr substrate starts to deform plastically at 12 Å before the yield point c seen in Figure 6-6 at 18 Å. However unlike pure the Zr system seen in Figure 6-7, no significant load drop is observed in the load-displacement curve for ZrO_2/Zr system when plastic deformation happens in Zr substrate. So, with the presence of the ZrO_2 layer, the plastic deformation of Zr substrate is delayed compared to the pure Zr system and can hardly be identified in the load-displacement curve. The dislocation lines in the top ZrO_2 layer are captured by DXA at an indentation depth of 18.5 Å as shown in Figure 6-8B. The green dislocation line in Figure 6-8B is a 1/6<110> Shockley partial, while the Burgers vector of the red dislocation cannot be identified by the DXA. The deformed structure corresponds to point c in Figure 6-6. This answers the other question raised in the previous section: the load drop at around 18 Å is caused by the plastic deformation in the top ZrO_2 layer. Before the formation of dislocation in ZrO_2 at around 18 Å, the ZrO_2 layer deforms the along [110] direction in the same way as discussed in Chapter 5 (see Figure 5-7). In addition, dislocation lines have been identified by DXA in ZrO_2 layer of ZrO_2/Zr system rather than in the pure ZrO_2 system. However, the ZrO_2 layer in ZrO_2/Zr system turns out to generate dislocations during nanoindentation simulation, which might be caused by the presence the heterogeneous interface and the fact that the ZrO_2 layer in ZrO_2/Zr system is a thin film.

The hardness of the ZrO_2/Zr system increases as the indentation depth increases until 13 Å, where the plastic deformation begins. Then it becomes stable and fluctuates between 13 Å and 18 Å. The above characteristic is the same as the pure Zr case seen in Figure 4-3. The hardness starts to decrease after 18 Å where the load starts to drop and the dislocations start to form in ZrO_2 layer. For pure ZrO_2 system, the hardness decreases after load drop and becomes stable later, as seen in Figure 5-13. So we speculate that if we indent deeper than 24 Å, the hardness might become stable. However, when we do actually indent deeper than 24 Å, the ZrO_2/Zr system fails and the ZrO_2 fragments in an explosive manner as it is not able to absorb more energy. The failed system is shown in Figure 6-9. In summary, before plastic deformation takes place in ZrO_2 layer, the characteristic of the relationship between hardness and indentation depth agrees with the pure Zr system. After plastic deformation takes place in ZrO_2 layer, characteristic of the relationship between hardness and indentation depth is similar to the pure ZrO_2 system.

The evolution of the volumetric strain is shown in Figure 6-10. The method to calculate atomic-level strain tensors can be found in References [205, 206]. The reference configuration of the system to calculate the atomic strain tensors is set to be the relaxed ZrO_2/Zr system before indentation. The first highly strained region locates at the interface right under the indenter as shown in Figure 6-10A. The stress firstly passes to the Zr substrate at the interface. In the above strained region, a dislocation starts to nucleate in the Zr substrate, which correspond to point a in the load-displacement curve shown in Figure 6-6. In Figure 6-10B, as the highly strained region continues to grow in the Zr substrate, the Zr surface that contacts with the indenter becomes highly strained. Then the highly strained region starts to appear inside the ZrO_2 layer as shown in Figure 6-10C. This region works as the dislocation nucleation site in the ZrO_2, which correspond to the point b in the load-displacement curve shown in Figure 6-6 where dislocation lines starts to be observed in ZrO_2. The strain does not accumulate at the interface except for the area right under the indenter.

Summary on ZrO_2/Zr

This work focuses on the deformation behaviors of ZrO_2/Zr system during nanoindentation simulation. The deformation behaviors are compared with those from pure Zr and pure ZrO_2 systems. The difference and similarities are illustrated.

In the load-displacement curve, the starting point of the plastic deformation in the Zr substrate can hardly be identified; the starting point of the plastic deformation in ZrO_2 layers is identified by the load decreases. The plastic deformation in both ZrO_2 layer and Zr substrate are delayed in ZrO_2/Zr system comparing to pure ZrO_2 and Zr case.

The relationship between hardness and indentation depth has two stages. The first can be represented by the pure Zr system. The second stage can be represented by the pure ZrO_2 system. The two stages are distinguished by the point where plastic deformation starts to take place in ZrO_2 layer.

The specific deformation processes in Zr substrate and ZrO_2 layer are the same as those in pure Zr and pure ZrO_2 except that dislocation lines are captured by DXA in ZrO_2 layers of ZrO_2/Zr system.

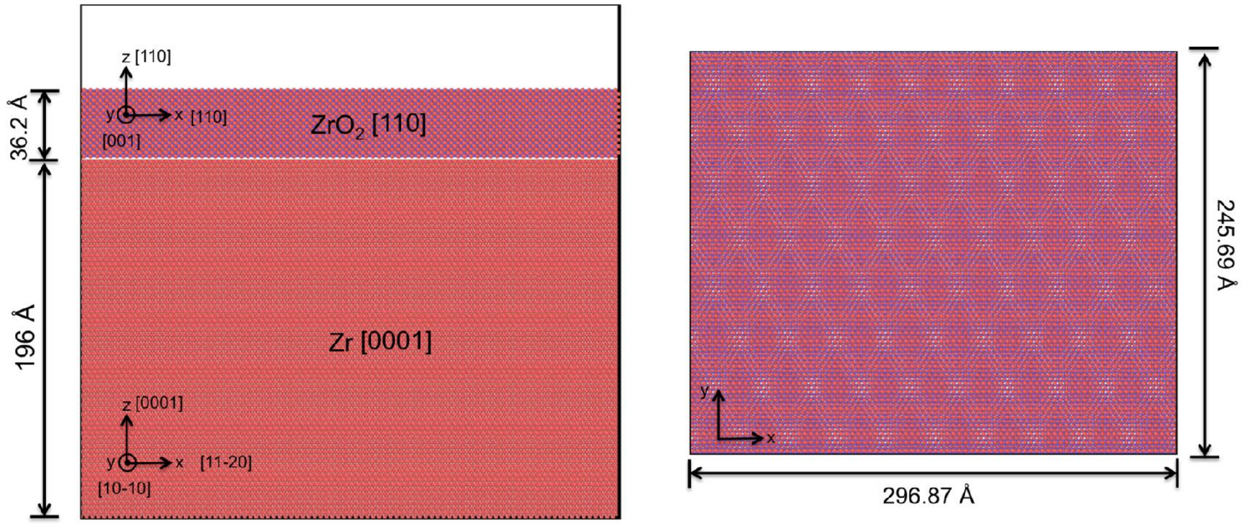

Figure 6-1. Schematic of the simulated ZrO_2/Zr system.

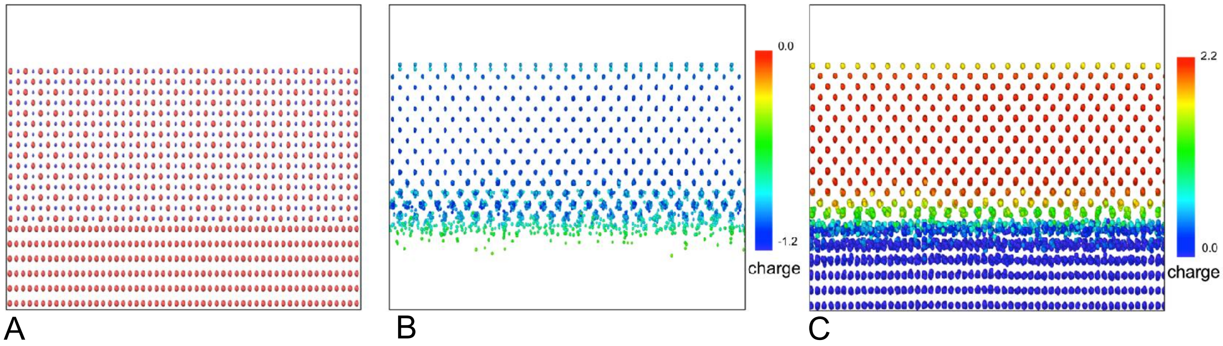

Figure 6-2. ZrO_2 and Zr interface. A) ZrO_2/Zr system before relaxation. Red atoms represent Zr and blue atoms represent O. B) Charge map of O atoms after relaxation. Only O atoms are shown. C) Charge map of Zr atoms after relaxation. Only Zr atoms are shown.

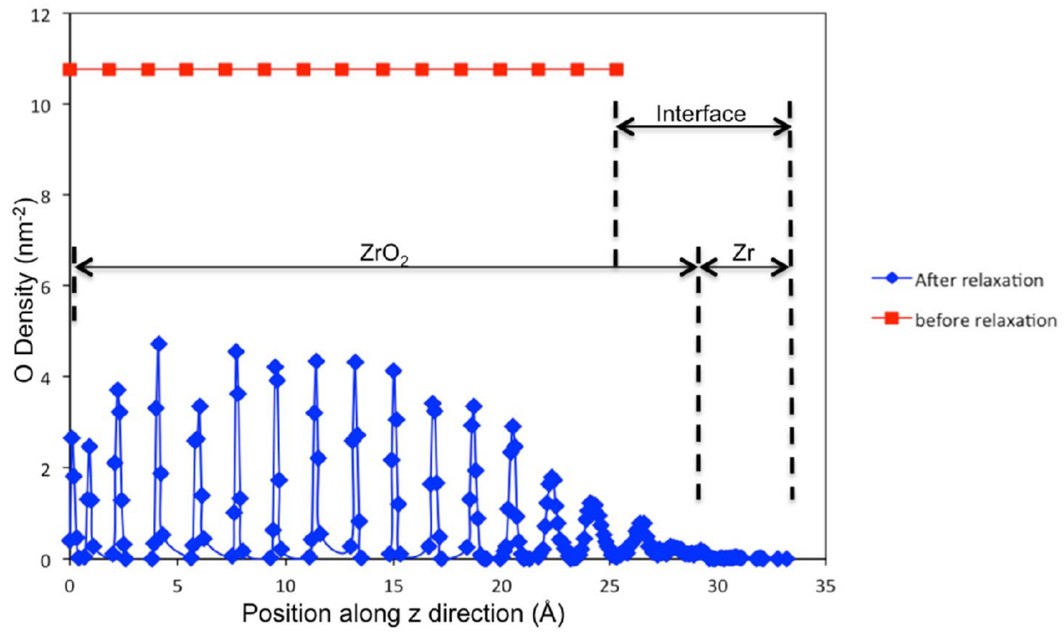

Figure 6-3. O density profile in ZrO_2/Zr system. Position at 0 Å represents the ZrO_2 surface.

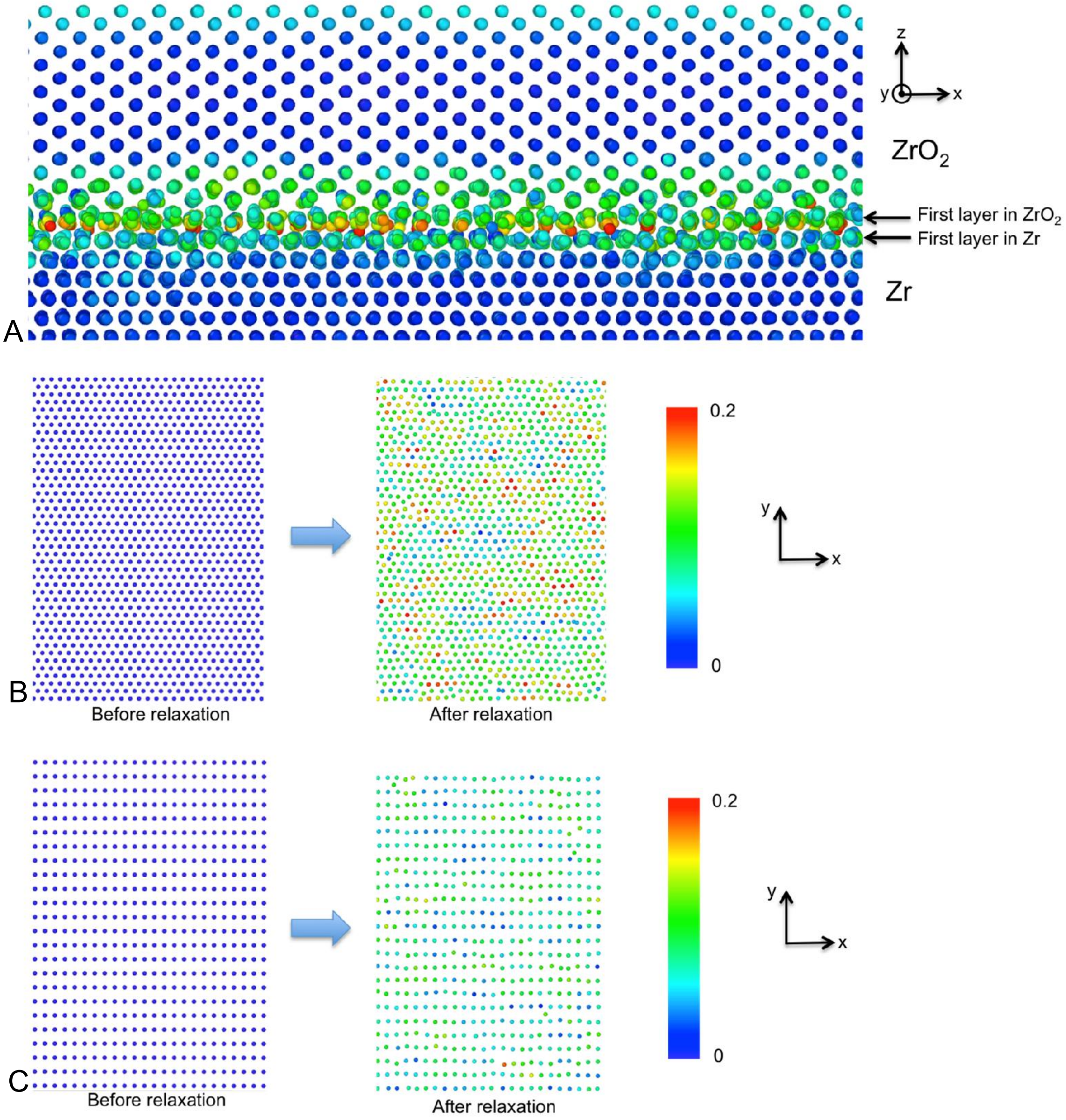

Figure 6-4. Shear strain map at the interface of ZrO_2/Zr system after relaxation. Color scheme represents the shear strain. O atoms have been removed. A) Side view of ZrO_2/Zr system. B) Top view of the first layer in Zr at the interface. C) Top view of the first layer in ZrO_2 at the interface.

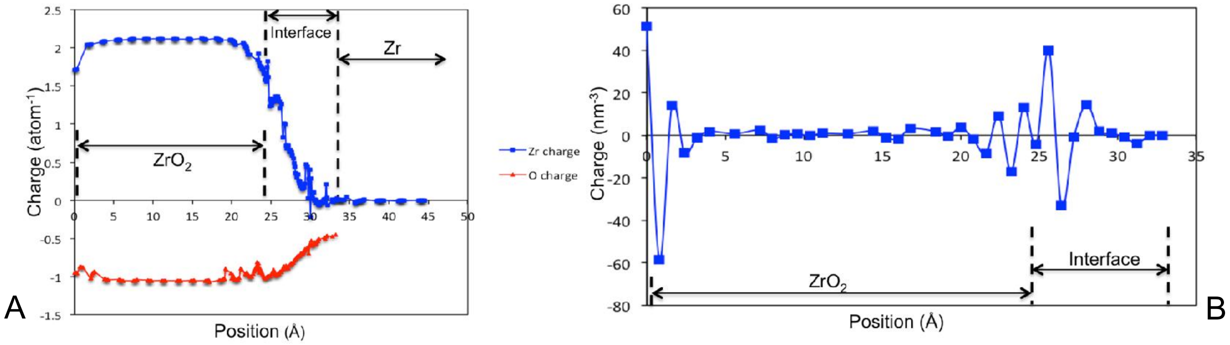

Figure 6-5. Charge profile across across the ZrO_2/Zr interface. A) Average charge of Zr and O across the ZrO_2/Zr interface. B) Total charge density across the ZrO_2/Zr interface.

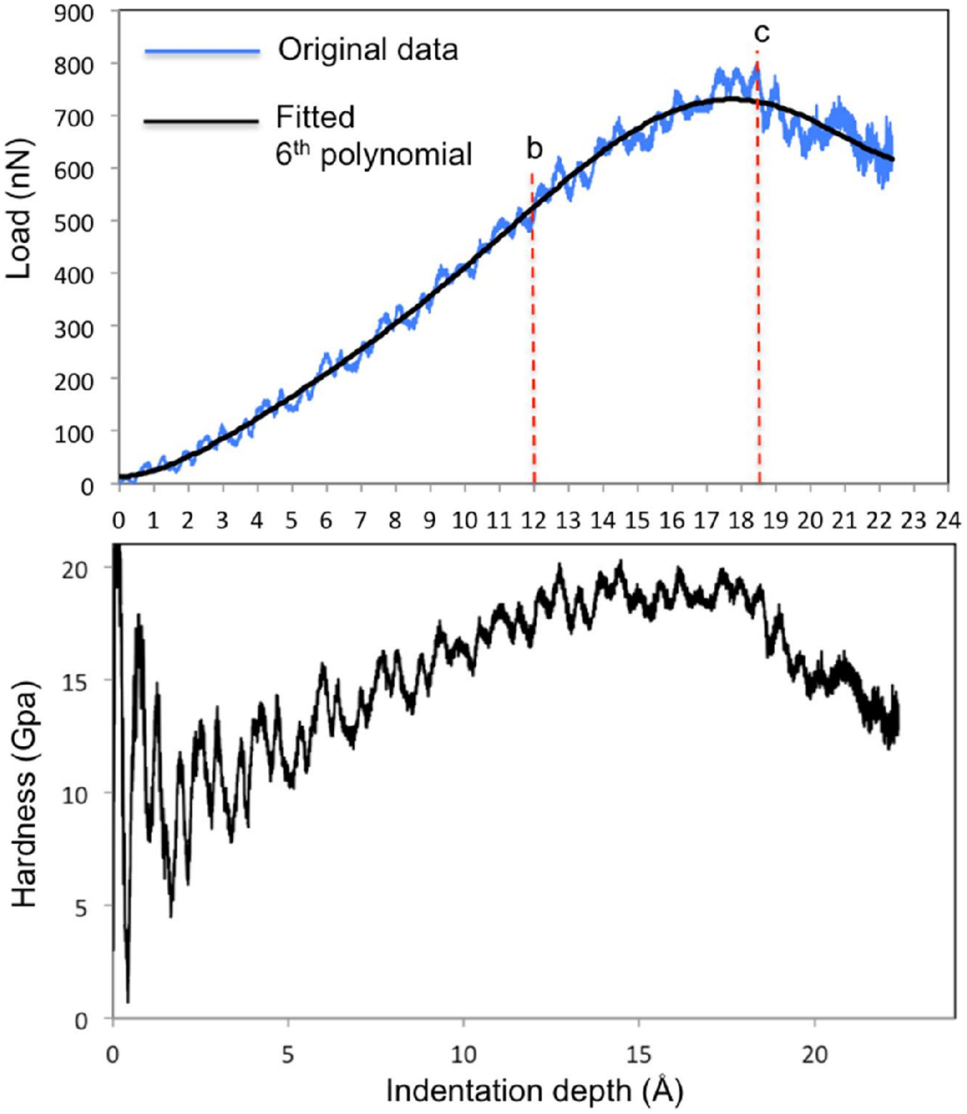

Figure 6-6. Load-displacement curve and hardness vs indentation depth.

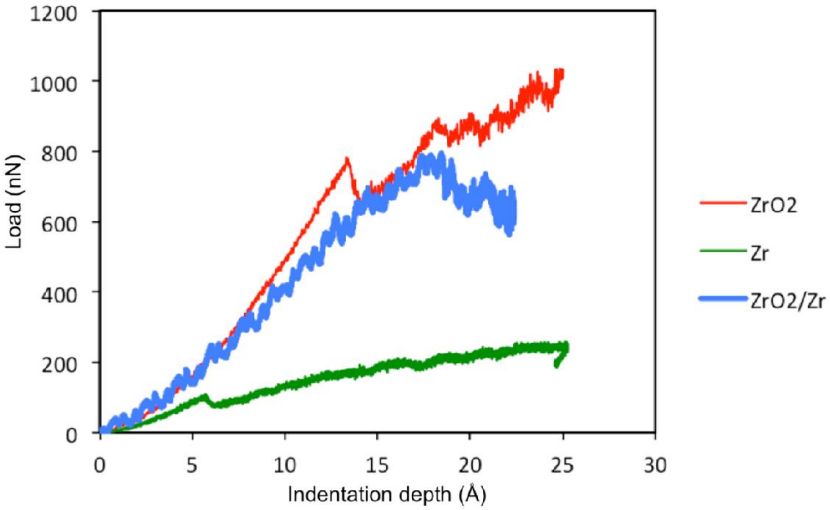

Figure 6-7. Load-displacement curve of Zr, ZrO_2 and ZrO_2/Zr system. Zr system is [0001] orientation. ZrO_2 is [110] orientation. And ZrO_2/Zr system is ZrO_2-(110) on top of Zr-(0001).

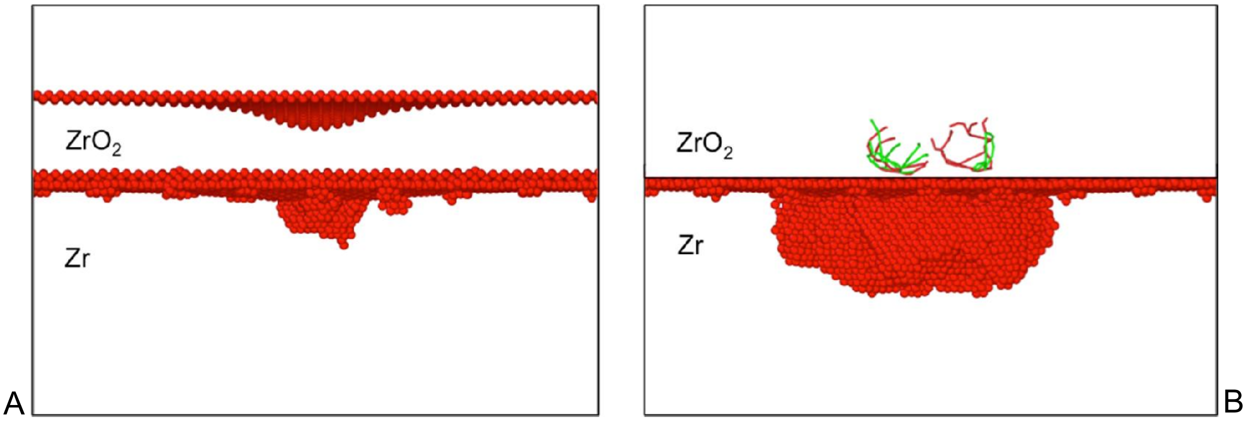

Figure 6-8. Deformed structure of ZrO$_2$/Zr system after nanoindentation. A) Deformed structure at 12.4 Å indentation depth. The red atoms represent disordered atoms. Atoms in fcc and hcp environment have been removed. B) Deformed structure at 19 Å indentation depth. The atoms in ZrO$_2$ layer have been removed. Only dislocation lines are shown. Green lines represent the Shockley partials. Red lines represent other dislocations types. The dislocation lines are captured using DXA.

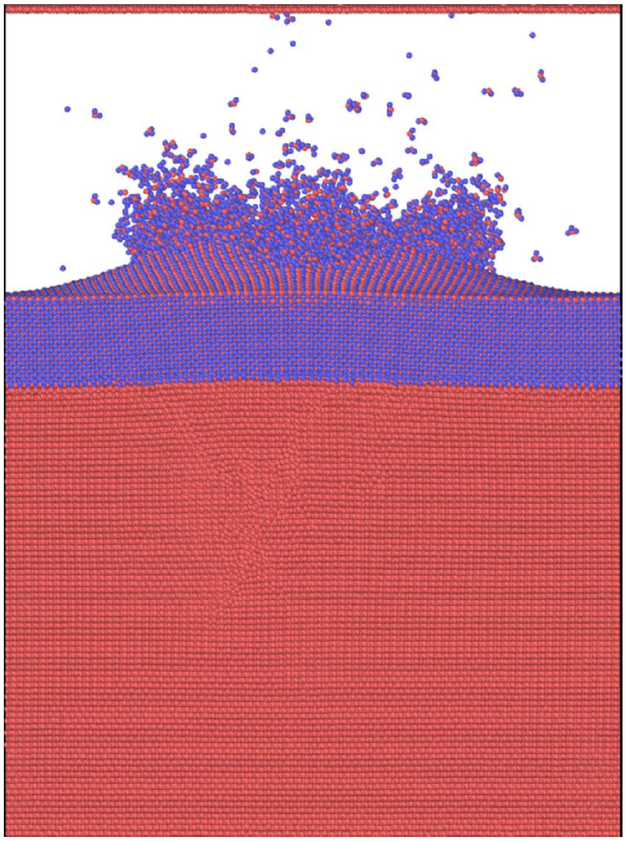

Figure 6-9. The failure of the ZrO_2 layer. Red atoms represent Zr atoms. Blue atoms represent O atoms.

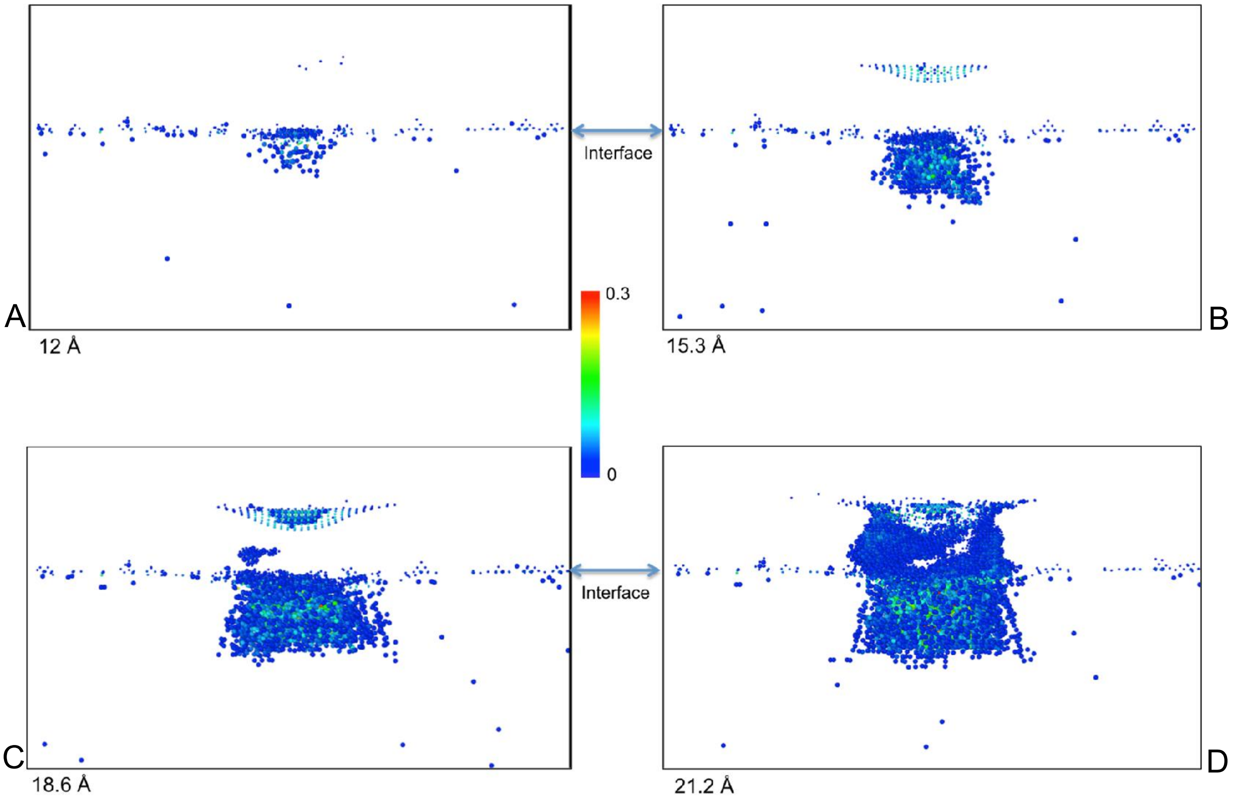

Figure 6-10. Evolution of volumetric strain during nanoindentation simulation. Atoms with volumetric strain value smaller than 0.02 are removed. A) Volumetric strain map at indentation depth of 12 Å. B) Volumetric strain map at indentation depth of 15.3 Å. C) Volumetric strain map at indentation depth of 18.6 Å. D) Volumetric strain map at indentation depth of 21.2 Å. The color scheme is volumetric strain.

CHAPTER 7
CONCLUSIONS

This work has studied the mechanical properties of Zr, ZrO_2 and ZrO_2/Zr systems using molecular dynamics as the simulation tool. Understanding the basic deformation behaviors of Zr-O system can help to design better zirconium-based cladding. Furthermore, our results are not only limited to the specific Zr and its oxide system but also a representative of at least some other hcp metal systems, fluorite ionic systems and metal-oxide heterogeneous systems. In addition, the nanoindentation simulation performed on the ZrO_2/Zr system is the first mechanical MD simulation done on ionic/metallic heterogeneous system.

The expected deformation modes including various dislocations have been observed in the 2D textured and 3D polycrystalline structures for both EAM and COMB potential. The two potentials' ability to describe mechanical properties is thus demonstrated.

For 2D textured structure, the activated deformation mode is determined by the texture. Despite differences in detail predicted by the two used potentials, the yield deformation behaviors are very similar. For the 3D structure, the experimentally observed primary slip system is prevalent, while the experimentally observed secondary slip systems are rare or absent. In the nanoindentation simulation, the dislocation processes are manifested in different ways. In particular, the various slip systems have more freedom to compete with each other. Moreover, the dislocation behaviors are well related to the unstable stacking fault energy. As a result, the yield deformation behaviors have a lot of difference for the two potentials, reflecting the differences in these energy barriers.

The stable and unstable stacking fault energy play an important in determining the deformation behaviors. The ratio of the stacking fault and unstable stacking fault energies along the dislocation gliding direction can determine whether the dislocation is a full dislocation or a partial dislocation. If the above ratio is close to unity, the dislocation will be a full dislocation; if the ratio is close to zero, the dislocation will be a partial dislocation. The partial dislocation can also form under scenario that the energy barrier along an indirect gliding path is smaller than that along the direct gliding path. The unstable stacking fault (energy barrier) on different gliding planes determines the primary slip system. The competition among different slip systems is controlled by the ratio of unstable stacking faults on different slip planes. In the nanoindentation simulation, $\frac{\gamma_{basal}}{\gamma_{prismatic}}$ equals 1.13 for MA EAM potential, so dislocation loops consist of both basal and prismatic dislocations are activated in the MA EAM simulation; $\frac{\gamma_{basal}}{\gamma_{prismatic}}$ equals to 1.41, only prismatic dislocation are activated. Additionally, from the potential fitting point of view, building an accurate stacking fault database is important for the potential to predict the right deformation behavior.

By comparing nanoindentation results of four different orientations we conclude that the hardness is determined by both the elastic deformation and plastic deformation. In the elastic region, the load-displacement curves agree well with Hertz Law. The larger reduced modulus leads to higher load response in the elastic region. The plastic deformation absorbs the energy and causes the load to drop. More dislocation activity lead to a larger load drop.

The comparison of Zr, ZrO_2 and ZrO_2/Zr systems give us some insights on how the deformation behaviors change in each individual system when different systems form a heterogeneous structure. The presence of the zirconium oxide layer on top of zirconium substrate significantly delays the plastic deformation in the zirconium substrate, as observed in the pure zirconium system. In addition, the study on ZrO_2/Zr system is the first MD simulation of the mechanical response of an ionic/metallic heterogeneous system.

LIST OF REFERENCES

1. M. Ruda, D. Farkas and G. Bertolino, *Computational Materials Science*, 2010, **49**, 743.

2. B. M. Ma, *Nuclear Reactor Materials and Applications*, Van Nostrand Reinhold Company, 1983.

3. H. Rickover, L. Geiger and B. Lustman, *History of the Development of Zirconium Alloys for Use in Nuclear Reactors*, Energy Research and Development Administration, Washington, DC (USA). Div. of Naval Reactors, 1975.

4. C. Lemaignan and A. T. Motta, in *Materials Science and Technology*, Wiley-VCH Verlag GmbH & Co. KGaA, 2006.

5. C. Whitmarsh, *Review of Zircaloy-2 and Zircaloy-4 Properties Relevant to NS Savannah Reactor Design*, Oak Ridge National Lab., Tenn., 1962.

6. M. Moalem and D. Olander, *Journal of Nuclear Materials*, 1991, **182**, 170.

7. C. Proff, *Microstructural Aspects of the Oxidation of Zirconium Alloys*, 2011.

8. J. J. Duderstadt and L. J. Hamilton, *Nuclear Reactor Analysis*, John Wiley and Sons, Inc.,New York., United States, 1976.

9. K. E. Sickafus, H. Matzke, T. Hartmann, K. Yasuda, J. A. Valdez, P. Chodak III, M. Nastasi and R. A. Verrall, *Journal of Nuclear Materials*, 1999, **274**, 66.

10. T. Claudson, J. Holmes, J. Straalsund and H. Brager, *Fast-Reactor Radiation-Induced Changes in Cladding and Structural Materials*, Battelle-Northwest, Richland, Wash., 1969.

11. S. J. Zinkle and J. T. Busby, *Materials Today*, 2009, **12**, 12.

12. A. K. Khan, Z. Yao, M. R. Daymond and R. A. Holt, *Nuclear Instruments & Methods in Physics Research Section B-Beam Interactions with Materials and Atoms*, 2012, **272**, 231.

13. F. Onimus, L. Dupuy and F. Mompiou, *Progress in Nuclear Energy*, 2012, **57**, 77.

14. F. Onimus, I. Monnet, J. L. Bechade, C. Prioul and P. Pilvin, *Journal of Nuclear Materials*, 2004, **328**, 165.

15. D. O. Northwood, R. W. Gilbert, L. E. Bahen, P. M. Kelly, R. G. Blake, A. Jostsons, P. K. Madden, D. Faulkner, W. Bell and R. B. Adamson, *Journal of Nuclear Materials*, 1979, **79**, 379.

16. P. Scott, *European Federation of Corrosion Publications*, 2007, **51**, 3.

17. P. Andresen, *Understanding and Mitigating Ageing in Nuclear Power Plants: Materials and Operational Aspects of Plant Life Management (Sawston, Cambridge, UK: Woodhead Publishing, 2010)*, 2010, 236.

18. K. Sieradzki and R. Newman, *Journal of Physics and Chemistry of Solids*, 1987, **48**, 1101.

19. R. Parkins, *Metallurgical Reviews*, 1964, **9**, 201.

20. J. Schiotz, F. Di Tolla and K. Jacobsen, *Nature*, 1998, **391**, 561.

21. J. Schiotz and K. Jacobsen, *Science*, 2003, **301**, 1357.

22. V. Yamakov, D. Wolf, S. Phillpot, A. Mukherjee and H. Gleiter, *Nature Materials*, 2002, **1**, 45.

23. V. Yamakov, D. Wolf, S. Phillpot, A. Mukherjee and H. Gleiter, *Nature Materials*, 2004, **3**, 43.

24. H. Van Swygenhoven, P. Derlet and A. Froseth, *Nature Materials*, 2004, **3**, 399.

25. M. Sangid, T. Ezaz, H. Sehitoglu and I. Robertson, *Acta Materialia*, 2011, **59**, 283.

26. A. H. Cottrell, *Dislocations and Plastic Flow in Crystals*, Clarendon Press, Oxford, 1961.

27. G. Zheng, Y. Wang and M. Li, *Acta Materialia*, 2005, **53**, 3893.

28. D. Kim, M. Manuel, F. Ebrahimi, J. Tulenko and S. Phillpot, *Acta Materialia*, 2010, **58**, 6217.

29. X. Liu, J. Adams, F. Ercolessi and J. Moriarty, *Modelling and Simulation in Materials Science and Engineering*, 1996, **4**, 293.

30. R. C. Pasianot and A. M. Monti, *Journal of Nuclear Materials*, 1999, **264**, 198.

31. C. Ruestes, G. Bertolino, M. Ruda, D. Farkas and E. Bringa, *Scripta Materialia*, 2014, **71**, 9.

32. C. Roberts, *Magnesium and Its Alloys*, Wiley, New York, 1960.

33. E. Tenckhoff, *Deformation Mechanisms, Texture, and Anisotropy in Zirconium and Zircaloy*, ASTM International, 1988.

34. J. X. Zheng-Johansson, O. Eriksson and B. Johansson, *Physical Review B*, 1999, **59**, 6131.

35. D. J. Bacon and V. Vitek, *Metallurgical and Materials Transactions a-Physical Metallurgy and Materials Science*, 2002, **33**, 721.

36. L. Addessio, E. Cerreta and G. Gray, *Metallurgical and Materials Transactions a-Physical Metallurgy and Materials Science*, 2005, **36A**, 2893.

37. I. N. Sokurskii and L. N. Protsenko, *The Soviet Journal of Atomic Energy*, 1958, **4**, 579.

38. R. Rose, K. Lunde and S. Aas, *Nuclear Engineering and Design*, 1975, **33**, 219.

39. S. Goel, R. Jayaganthan, I. Singh, D. Srivastava, G. Dey and N. Saibaba, *Materials & Design*, 2014, **55**, 612.

40. S. Goel, N. Keskar, R. Jayaganthan, I. Singh, D. Srivastava, G. Dey, S. Jha and N. Saibaba, *Journal of Materials Engineering and Performance*, 2015, **24**, 618.

41. S. Goel, N. Keskar, R. Jayaganthan, I. Singh, D. Srivastava, G. Dey and N. Saibaba, *Materials Science and Engineering: A*, 2014, **603**, 23.

42. K. L. Murty and I. Charit, *Progress in Nuclear Energy*, 2006, **48**, 325.

43. J. Park, *Bioceramics: Properties, Characterizations, and Applications*, 2008, 136.

44. C. J. Howard, R. J. Hill and B. E. Reichert, *Acta Crystallographica Section B-Structural Science*, 1988, **44**, 116.

45. M. Mamivand, M. A. Zaeem, H. El Kadiri and L.-Q. Chen, *Acta Materialia*, 2013, **61**, 5223.

46. R. H. Hannink, P. M. Kelly and B. C. Muddle, *Journal of the American Ceramic Society*, 2000, **83**, 461.

47. E. H. Kisi and C. Howard, *Crystal Structures of Zirconia Phases and Their Inter-relation*, Key Engineering Materials, 1998.

48. B. Basu, J. Vleugels and O. Van Der Biest, *Materials Science and Engineering: A*, 2004, **366**, 338.

49. R. Garvie, R. Hannink and R. Pascoe, *Nature*, 1975, **258**, 703.

50. J. M. Leger, P. E. Tomaszewski, A. Atouf and A. S. Pereira, *Physical Review B*, 1993, **47**, 14075.

51. O. Ohtaka, T. Yamanaka, S. Kume, E. Ito and A. Navrotsky, *Journal of the American Ceramic Society*, 1991, **74**, 505.

52. S. Block, J. D. Jornada and G. Piermarini, *Journal of the American Ceramic Society*, 1985, **68**, 497.

53. H. G. Scott, *Journal of Materials Science*, 1975, **10**, 1527.

54. U. Messerschmidt, D. Baither, B. Baufeld and M. Bartsch, *Materials Science and Engineering a-Structural Materials Properties Microstructure and Processing*, 1997, **233**, 61.

55. B. Baufeld, D. Baither, M. Bartsch and U. Messerschmidt, *Physica Status Solidi a-Applied Research*, 1998, **166**, 127.

56. G. David, R. Geschier and C. Roy, *Journal of Nuclear Materials*, 1971, **38**, 329.

57. C. Roy and G. David, *Journal of Nuclear Materials*, 1970, **37**, 71.

58. J. S. Moya, M. Diaz, J. F. Bartolome, E. Roman, J. L. Sacedon and J. Izquierdo, *Acta Materialia*, 2000, **48**, 4749.

59. G. J. Yurek, J. V. Cathcart and R. E. Pawel, *Oxidation of Metals*, 1976, **10**, 255.

60. L. Kurpaska, J. Favergeon, L. Lahoche, G. Moulin, M. El Marssi and J.-M. Roelandt, *Oxidation of Metals*, 2013, **79**, 261.

61. A. Garner, A. Gholinia, P. Frankel, M. Gass, I. MacLaren and M. Preuss, *Acta Materialia*, 2014, **80**, 159.

62. N. Ni, S. Lozano-Perez, M. L. Jenkins, C. English, G. D. W. Smith, J. M. Sykes and C. R. M. Grovenor, *Scripta Materialia*, 2010, **62**, 564.

63. J. Godlewski, J. Gros, M. Lambertin, J. Wadier and H. Weidinger, *ASTM—STP*, 1991, **1132**, 416.

64. J. Godlewski, *How the Tetragonal Zirconia is Stabilized in the Oxide Scale that is Formed on a Zirconium Alloy Corroded at 400 C in Steam*, Zirconium in the Nuclear Industry: Tenth International Symposium, 1994.

65. P. Bouvier, J. Godlewski and G. Lucazeau, *Journal of Nuclear Materials*, 2002, **300**, 118.

66. B. Cox, *Are Zirconia Corrosion Films a Form of Partially Stabilised Zirconia (PSZ)?*, Chalk River Nuclear Laboratories, 1987.

67. N. Petigny, P. Barberis, C. Lemaignan, C. Valot and M. Lallemant, *Journal of Nuclear Materials*, 2000, **280**, 318.

68. R. Ploc, *Journal of Nuclear Materials*, 1982, **110**, 59.

69. R. Ploc, *Journal of Nuclear Materials*, 1983, **113**, 75.

70. R. Ploc, *Journal of Nuclear Materials*, 1983, **115**, 110.

71. M. J. Noordhoek, T. Liang, T. W. Chiang, S. B. Sinnott and S. R. Phillpot, *Journal of Nuclear Materials*, 2014, **452**, 285.

72. F. C. Frank, *Philosophical Magazine*, 1951, **42**, 809.

73. Z. Ding, S. Li, W. Liu and Y. Zhao, *Advances in Materials Science and Engineering*, 2015, **2015**, 1.

74. D. Hull and D. J. Bacon, *Introduction to Dislocations*, Pergamon Press Oxford, 1984.

75. M. Chou, M. L. Cohen and S. G. Louie, *Physical Review B*, 1985, **32**, 7979.

76. J. R. Rice, *Journal of the Mechanics and Physics of Solids*, 1992, **40**, 239.

77. J. A. Zimmerman, H. Gao and F. F. Abraham, *Modelling and Simulation in Materials Science and Engineering*, 2000, **8**, 103.

78. E. Tadmor and S. Hai, *Journal of the Mechanics and Physics of Solids*, 2003, **51**, 765.

79. M. Shetty, *Dislocations and Mechanical Behaviour of Materials*, PHI Learning Pvt. Ltd., 2013.

80. R. M. Martin, *Electronic Structure: Basic Theory and Practical Methods*, Cambridge university press, 2004.

81. D. Sholl and J. A. Steckel, *Density Functional Theory: a Practical Introduction*, John Wiley & Sons, 2011.

82. D. C. Rapaport, *The Art of Molecular Dynamics Simulation*, Cambridge university press, 2004.

83. M. P. Allen and D. J. Tildesley, *Computer Simulation of Liquids*, Clarendon Press, 1987.

84. R. D. Skeel, in *The Graduate Student's Guide to Numerical Analysis' 98*, Springer, 1999, pp. 119.

85. L. Verlet, *Physical Review*, 1967, **159**, 98.

86. J. Haile, *Molecular Dynamics Simulation*, Wiley, New York, 1992.

87. H. J. Berendsen, J. P. M. Postma, W. F. van Gunsteren, A. DiNola and J. Haak, *The Journal of Chemical Physics*, 1984, **81**, 3684.

88. S. Nosé, *Molecular Physics*, 1984, **52**, 255.

89. S. Adelman and J. D. Doll, *The Journal of Chemical Physics*, 1974, **61**, 4242.

90. J. Doll, L. Myers and S. Adelman, *The Journal of Chemical Physics*, 1975, **63**, 4908.

91. S. A. Adelman and J. D. Doll, *The Journal of Chemical Physics*, 1976, **64**, 2375.

92. Y. H. Hu and S. B. Sinnott, *Journal of Computational Physics*, 2004, **200**, 251.

93. K. Huang, *Introduction to Statistical Physics*, CRC Press, 2009.

94. G. S. Grest and K. Kremer, *Physical Review A*, 1986, **33**, 3628.

95. H. C. Andersen, *The Journal of Chemical Physics*, 1980, **72**, 2384.

96. M. Parrinello and A. Rahman, *Journal of Applied Physics*, 1981, **52**, 7182.

97. R. LeSar, *Introduction to Computational Materials Science: Fundamentals to Applications*, Cambridge University Press, 2013.

98. J. Yu, S. B. Sinnott and S. R. Phillpot, *Physical Review B*, 2007, **75**, 085311.

99. A. C. Van Duin, S. Dasgupta, F. Lorant and W. A. Goddard, *The Journal of Physical Chemistry A*, 2001, **105**, 9396.

100. M. S. Daw and M. I. Baskes, *Physical Review Letters*, 1983, **50**, 1285.

101. M. S. Daw and M. I. Baskes, *Physical Review B*, 1984, **29**, 6443.

102. A. F. Voter, in *Inter-metallic Compounds: Principles and Applications*, eds. W. J.H. and F. R.L., John Wiley & Sons Ltd, London, 1994, vol. 1.

103. M. Mendelev and G. Ackland, *Philosophical Magazine Letters*, 2007, **87**, 349.

104. T. Liang, B. Devine, S. R. Phillpot and S. B. Sinnott, *The Journal of Physical Chemistry A*, 2012, **116**, 7976.

105. T. Liang, Y. K. Shin, Y.-T. Cheng, D. E. Yilmaz, K. G. Vishnu, O. Verners, C. Zou, S. R. Phillpot, S. B. Sinnott and A. C. van Duin, *Annual Review of Materials Research*, 2013, **43**, 109.

106. G. Abell, *Physical Review B*, 1985, **31**, 6184.

107. J. R. Chelikowsky, J. Phillips, M. Kamal and M. Strauss, *Physical Review Letters*, 1989, **62**, 292.

108. D. Pettifor, *Physical Review Letters*, 1989, **63**, 2480.

109. D. Pettifor and I. Oleinik, *Physical Review B*, 1999, **59**, 8487.

110. I. Oleinik and D. Pettifor, *Physical Review B*, 1999, **59**, 8500.

111. J. Tersoff, *Physical Review Letters*, 1986, **56**, 632.

112. J. Tersoff, *Physical Review Letters*, 1988, **61**, 2879.

113. A. K. Rappe and W. A. Goddard III, *The Journal of Physical Chemistry*, 1991, **95**, 3358.

114. F. Streitz and J. Mintmire, *Physical Review B*, 1994, **50**, 11996.

115. M. Noordhoek, *Development of Classical Interatomic Potentials for Applications in Corrosion and Phase Transitions*, UNIVERSITY OF FLORIDA, 2014.

116. A. Yasukawa, *JSME International Journal. Series A, Mechanics and Material Engineering*, 1996, **39**, 313.

117. J. Yu, S. R. Phillpot and S. B. Sinnott, *Physical Review B*, 2007, **75**, 233203.

118. B. Devine, T.-R. Shan, Y.-T. Cheng, A. J. McGaughey, M. Lee, S. R. Phillpot and S. B. Sinnott, *Physical Review B*, 2011, **84**, 125308.

119. J. C. Slater, *Physical Review*, 1930, **36**, 57.

120. K. C. Harper and M. S. Sigman, *Science*, 2011, **333**, 1875.

121. A. Stukowski, *Modelling and Simulation in Materials Science and Engineering*, 2010, **18**, 015012.

122. J. Li, *Modelling and Simulation in Materials Science and Engineering*, 2003, **11**, 173.

123. A. Stukowski and K. Albe, *Modelling and Simulation in Materials Science and Engineering*, 2010, **18**, 085001.

124. A. Stukowski, *Modelling and Simulation in Materials Science and Engineering*, 2012, **20**, 045021.

125. A. Stukowski, V. V. Bulatov and A. Arsenlis, *Modelling and Simulation in Materials Science and Engineering*, 2012, **20**, 085007.

126. A. Clarke and H. Jonsson, *Physical Review E*, 1993, **47**, 3975.

127. H. Jonsson and H. Andersen, *Physical Review Letters*, 1988, **60**, 2295.

128. J. D. Osorio, A. Lopera-Valle, A. Toro and J. P. Hernández-Ortiz, *DYNA*, 2014, **81**, 13.

129. P. Niranatlumpong, C. Ponton and H. Evans, *Oxidation of Metals*, 2000, **53**, 241.

130. S. Amelinckx, *Il Nuovo Cimento (1955-1965)*, 1958, **7**, 569.

131. C. Suryanarayana and C. C. Koch, *Hyperfine Interactions*, 2000, **130**, 5.

132. M. Noordhoek, T. Liang, Z. Lu, T. Shan, S. Sinnott and S. Phillpot, *Journal of Nuclear Materials*, 2013, **441**, 274.

133. G. Ackland, S. Wooding and D. Bacon, *Philosophical Magazine a-Physics of Condensed Matter Structure Defects and Mechanical Properties*, 1995, **71**, 553.

134. G. W. Simmons, H., *Single Crystal Elastic Constants: A Handbook*, MIT Press, Cambridge, MA, 1971.

135. C. Kittel, *Introduction to Solid State Physics*, Wiley, New York, 1986.

136. Y. Udagawa, M. Yamaguchi, H. Abe, N. Sekimura and T. Fuketa, *Acta Materialia*, 2010, **58**, 3927.

137. A. Poty, J. Raulot, H. Xu, J. Bai, C. Schuman, J. Lecomte, M. Philippe and C. Esling, *Journal of Applied Physics*, 2011, **110**, 014905.

138. V. Yamakov, D. Wolf, M. Salazar, S. Phillpot and H. Gleiter, *Acta Materialia*, 2001, **49**, 2713.

139. I. P. Jones and W. B. Hutchinson, *Acta Metallurgica*, 1981, **29**, 951.

140. J. R. Morris, J. Scharff, K. M. Ho, D. E. Turner, Y. Y. Ye and M. H. Yoo, *Philosophical Magazine A-Physics of Condensed Matter Structure Defects and Mechanical Properties*, 1997, **76**, 1065.

141. J. P. Hirth and J. Lothe, *Theory of Dislocations*, McGraw-Hill, New York, 1967-1968.

142. L. Wang, P. Eisenlohr, Y. Yang, T. R. Bieler and M. A. Crimp, *Scripta Materialia*, 2010, **63**, 827.

143. I. J. Beyerlein, R. J. McCabe and C. N. Tome, *International Journal for Multiscale Computational Engineering*, 2011, **9**, 459.

144. I. Beyerlein, X. Zhang and A. Misra, *Annual Review of Materials Research*, 2014, **44**, 329.

145. W. C. Oliver and G. M. Pharr, *Journal of Materials Research*, 1992, **7**, 1564.

146. C. A. Schuh, *Materials Today*, 2006, **9**, 32.

147. W. C. Oliver and G. M. Pharr, *MRS Bulletin*, 2010, **35**, 897.

148. H. Nili, K. Kalantar-zadeh, M. Bhaskaran and S. Sriram, *Progress in Materials Science*, 2013, **58**, 1.

149. H. Huang and H. W. Zhao, *Science of Advanced Materials*, 2014, **6**, 875.

150. Z. Z. Lu, M. J. Noordhoek, A. Chernatynskiy, S. B. Sinnott and S. R. Phillpot, *Journal of Nuclear Materials*, 2015, **462**, 147.

151. C. L. Kelchner, S. J. Plimpton and J. C. Hamilton, *Physical Review B*, 1998, **58**, 11085.

152. A. K. Nair, E. Parker, P. Gaudreau, D. Farkas and R. D. Kriz, *International Journal of Plasticity*, 2008, **24**, 2016.

153. A. Stukowski and A. Arsenlis, *Modelling and Simulation in Materials Science and Engineering*, 2012, **20**, 035012.

154. X. L. Ma and W. Yang, *Nanotechnology*, 2003, **14**, 1208.

155. T. P. Remington, C. J. Ruestes, E. M. Bringa, B. A. Remington, C. H. Lu, B. Kad and M. A. Meyers, *Acta Materialia*, 2014, **78**, 378.

156. C. J. Ruestes, A. Stukowski, Y. Tang, D. R. Tramontina, P. Erhart, B. A. Remington, H. M. Urbassek, M. A. Meyers and E. M. Bringa, *Materials Science and Engineering a-Structural Materials Properties Microstructure and Processing*, 2014, **613**, 390.

157. A. V. Verkhovtsev, M. Hanauske, A. V. Yakubovich and A. V. Solov'yov, *Computational Materials Science*, 2013, **76**, 80.

158. S. Plimpton, *Journal of Computational Physics*, 1995, **117**, 1.

159. L. Calabri, N. Pugno, A. Rota, D. Marchetto and S. Valeri, *Journal of Physics: Condensed Matter*, 2007, **19**, 395002.

160. J. Swadener, E. George and G. Pharr, *Journal of the Mechanics and Physics of Solids*, 2002, **50**, 681.

161. K. L. Johnson, *Contact Mechanics*, Cambridge University Press, Cambridge, UK, 1985.

162. E. T. Lilleodden, J. A. Zimmerman, S. M. Foiles and W. D. Nix, *Journal of the Mechanics and Physics of Solids*, 2003, **51**, 901.

163. D. Tromans, *IJRRAS*, 2011, **6**, 462.

164. A. Ballato, *Ieee Transactions on Ultrasonics Ferroelectrics and Frequency Control*, 1996, **43**, 56.

165. A. Ballato, *Poisson's Ratio for Hexagonal Crystals*, Report ARL-TD-424, Army Research Laboratory, 1995.

166. J. F. Nye, *Physical Properties of Crystal-Their Representation by Tensors and Materials*, Oxford Univeristy Press, UK, 1985.

167. D. J. Green, *An Introduction to the Mechanical Properties of Ceramics*, Cambridge University Press, Camgridge, 1998.

168. D. Tabor, *Hardness of Metals*, Clarendon Press, Oxford, 1951.

169. C. Yan, R. Wang, Y. Wang, X. Wang, Z. Lin, G. Bai and Y. Zhang, *Materials Science and Engineering: A*, 2015, **628**, 50.

170. A. Serra and D. J. Bacon, *Philosophical Magazine*, 2010, **90**, 845.

171. E. Schmid and W. Boas, *Plasticity of Crystals with Special Reference to Metals*, F.A. Hughes & Co. Ltd., 1935.

172. Z. Z. Lu, M. J. Noordhoek, A. Chernatynskiy, S. B. Sinnott and S. R. Phillpot, *Journal of Nuclear Materials*, 2015, **467**, 742.

173. C. Piconi and G. Maccauro, *Biomaterials*, 1999, **20**, 1.

174. Y. Ichikawa, Y. Akagawa, H. Nikai and H. Tsuru, *The Journal of Prosthetic Dentistry*, 1992, **68**, 322.

175. I. Denry and J. R. Kelly, *Dental Materials*, 2008, **24**, 299.

176. M. Schehl, J. M. Calderon-Moreno, R. Torrecillas and Ttp, in *Euro Ceramics Vii, Pt 1-3*, Trans Tech Publications Ltd, Zurich-Uetikon, 2002, vol. 206-2, pp. 1001.

177. E.-O. Oh, C.-M. Whang, Y.-R. Lee, J.-H. Lee, K. J. Yoon, B.-K. Kim, J.-W. Son, J.-H. Lee and H.-W. Lee, *Journal of the European Ceramic Society*, 2012, **32**, 1733.

178. S. Badwal, F. Ciacchi and D. Milosevic, *Solid State Ionics*, 2000, **136**, 91.

179. L. Chen, *Surface Review and Letters*, 2006, **13**, 535.

180. T. Liang, T. R. Shan, Y. T. Cheng, B. D. Devine, M. Noordhoek, Y. Z. Li, Z. Z. Lu, S. R. Phillpot and S. B. Sinnott, *Materials Science & Engineering R-Reports*, 2013, **74**, 255.

181. P. K. Schelling, S. R. Phillpot and D. Wolf, *Journal of the American Ceramic Society*, 2001, **84**, 1609.

182. X. Zhou, H. Wadley, J.-S. Filhol and M. Neurock, *Physical Review B*, 2004, **69**, 035402.

183. A. C. van Duin, B. V. Merinov, S. S. Jang and W. A. Goddard, *The Journal of Physical Chemistry A*, 2008, **112**, 3133.

184. M. Kilo, R. A. Jackson and G. Borchardt, *Philosophical Magazine*, 2003, **83**, 3309.

185. G. Lewis and C. Catlow, *Journal of Physics C: Solid State Physics*, 1985, **18**, 1149.

186. V. Butler, C. Catlow and B. Fender, *Solid State Ionics*, 1981, **5**, 539.

187. A. Dwivedi and A. N. Cormack, *Philosophical Magazine A*, 1990, **61**, 1.

188. C. Yin, F. Ye, C. Y. Yin, D. R. Ou and T. Mori, *Applied Mechanics and Materials*, 2014, **492**, 239.

189. G. Fadda, L. Colombo and G. Zanzotto, *Physical Review B*, 2009, **79**, 214102.

190. M. Fujikane, D. Setoyama, S. Nagao, R. Nowak and S. Yamanaka, *Journal of Alloys and Compounds*, 2007, **431**, 250.

191. D. Wolf, *Physical Review Letters*, 1992, **68**, 3315.

192. P. Tasker, *Journal of Physics C: Solid State Physics*, 1979, **12**, 4977.

193. N. Zhang and Y. Chen, *Journal of Materials Science*, 2013, **48**, 785.

194. S. Gadag, G. Subbarayan and W. Barker, *Journal of Materials Science*, 2006, **41**, 1221.

195. M. A. Lodes, A. Hartmaier, M. Goken and K. Durst, *Acta Materialia*, 2011, **59**, 4264.

196. H. M. Kandil, J. D. Greiner and J. F. Smith, *Journal of the American Ceramic Society*, 1984, **67**, 341.

197. T. W. Chiang, A. Chernatynskiy, M. J. Noordhoek, S. B. Sinnott and S. R. Phillpot, *Computational Materials Science*, 2015, **98**, 112.

198. C.-S. Zhang, B. Flinn, I. Mitchell and P. Norton, *Surface Science*, 1991, **245**, 373.

199. C.-S. Zhang, B. Flinn and P. Norton, *Surface Science*, 1992, **264**, 1.

200. M. Yamamoto, C. Chan, K. Ho and S. Naito, *Physical Review B*, 1996, **54**, 14111.

201. G. Bakradze, L. P. Jeurgens and E. J. Mittemeijer, *Surface and Interface Analysis*, 2010, **42**, 588.

202. G. Bakradze, L. P. Jeurgens and E. J. Mittemeijer, *Journal of Applied Physics*, 2011, **110**, 4904.

203. S. K. Sankaranarayanan, E. Kaxiras and S. Ramanathan, *Energy & Environmental Science*, 2009, **2**, 1196.

204. S. Kul'kova, A. Bakulin, S. Hocker and S. Schmauder, *Technical Physics*, 2013, **58**, 325.

205. M. Falk and J. Langer, *Physical Review E*, 1998, **57**, 7192.

206. F. Shimizu, S. Ogata and J. Li, *Materials Transactions*, 2007, **48**, 2923.

BIOGRAPHICAL SKETCH

Zizhe Lu was born and raised in Shijiazhuang, Hebei, China. He received his bachelor’s degree in materials physics from Hebei University of Technology in 2010. That August, Lu decided to go to United States for higher education. He joined the graduate program in University of Florida in Materials Science and Engineering. In 2011, he joined the Computational Materials Science Focus Group under the guidance of Dr. Simon Phillpot.